



National Library  
of Canada

Acquisitions and  
Bibliographic Services Branch

395 Wellington Street  
Ottawa, Ontario  
K1A 0N4

Bibliothèque nationale  
du Canada

Direction des acquisitions et  
des services bibliographiques

395, rue Wellington  
Ottawa (Ontario)  
K1A 0N4

Your file / Votre référence

Our file / Notre référence

## NOTICE

The quality of this microform is heavily dependent upon the quality of the original thesis submitted for microfilming. Every effort has been made to ensure the highest quality of reproduction possible.

If pages are missing, contact the university which granted the degree.

Some pages may have indistinct print especially if the original pages were typed with a poor typewriter ribbon or if the university sent us an inferior photocopy.

Reproduction in full or in part of this microform is governed by the Canadian Copyright Act, R.S.C. 1970, c. C-30, and subsequent amendments.

## AVIS

La qualité de cette microforme dépend grandement de la qualité de la thèse soumise au microfilmage. Nous avons tout fait pour assurer une qualité supérieure de reproduction.

S'il manque des pages, veuillez communiquer avec l'université qui a conféré le grade.

La qualité d'impression de certaines pages peut laisser à désirer, surtout si les pages originales ont été dactylographiées à l'aide d'un ruban usé ou si l'université nous a fait parvenir une photocopie de qualité inférieure.

La reproduction, même partielle, de cette microforme est soumise à la Loi canadienne sur le droit d'auteur, SRC 1970, c. C-30, et ses amendements subséquents.

**MTF, NPS and DQE Analysis of Portal  
Metal-Plate/Film Detectors**

by

Tony Falco  
Medical Physics Unit  
McGill University, Montreal  
March, 1996

A thesis submitted to the Faculty of Graduate Studies and Research in  
partial fulfillment of the requirements for the degree of  
Master of Science

© T. Falco, 1996



National Library  
of Canada

Acquisitions and  
Bibliographic Services Branch

395 Wellington Street  
Ottawa, Ontario  
K1A 0N4

Bibliothèque nationale  
du Canada

Direction des acquisitions et  
des services bibliographiques

395, rue Wellington  
Ottawa (Ontario)  
K1A 0N4

*Your file* *Votre référence*

*Our file* *Notre référence*

The author has granted an irrevocable non-exclusive licence allowing the National Library of Canada to reproduce, loan, distribute or sell copies of his/her thesis by any means and in any form or format, making this thesis available to interested persons.

L'auteur a accordé une licence irrévocable et non exclusive permettant à la Bibliothèque nationale du Canada de reproduire, prêter, distribuer ou vendre des copies de sa thèse de quelque manière et sous quelque forme que ce soit pour mettre des exemplaires de cette thèse à la disposition des personnes intéressées.

The author retains ownership of the copyright in his/her thesis. Neither the thesis nor substantial extracts from it may be printed or otherwise reproduced without his/her permission.

L'auteur conserve la propriété du droit d'auteur qui protège sa thèse. Ni la thèse ni des extraits substantiels de celle-ci ne doivent être imprimés ou autrement reproduits sans son autorisation.

ISBN 0-612-12191-7

**Canada**

## Abstract

Previous studies of modulation transfer function (MTF), noise power spectrum (NPS), and detective quantum efficiency (DQE) of metal-plate/film portal detectors have been performed on limited combinations of front and back metal-plates. We report on these parameters for an extensive set of forty-nine front-back metal-plate combinations. The portal detector consists of a double emulsion RP (Kodak localization therapy) film placed between metal-plates: Al, Cu, brass and Pb of thicknesses varying from 0.30 to 4.80 mm. Radiation sources included a Theratron Co-60 unit, and a Varian Clinac-18 linear accelerator delivering a polyenergetic 10 MV X-ray spectrum. In terms of the absolute efficiency of the detectors, the best DQE is obtained with the detector consisting of a 1.75 mm Cu front plate and a 1.62 mm Al back plate for the Clinac-18, and with the detector consisting of a 0.95 mm Cu front plate and a 0.80 mm Cu or a 1.62 mm Al back plate for the Co-60 gamma ray source.

## Résumé

Peu d'études ont été effectuées pour évaluer la fonction de transfert de modulation (MTF), le spectre de puissance du bruit (NPS), et l'efficacité de détection quantique (DQE) pour des détecteurs composés d'un film radiographique situé entre des plaques de métal. Notre détecteur, conçu pour l'imagerie médicale à de hautes énergies, consiste en un film RP (Kodak, localisation de thérapie) à double émulsion placé entre des plaques de métal de composition variée: Al, Cu, laiton, et Pb variant entre 0.30 mm et 4.80 mm d'épaisseurs. Deux sources de photons ont été utilisées pour irradier le détecteur: le cobalt-60 et un spectre de rayons x (10 MV) provenant d'un accélérateur linéaire Varian Clinac-18. Nous avons étudié le MTF, le NPS, et le DQE pour quarante-neuf combinaisons de plaque-avant/plaque-arrière. Nous avons conclu que les détecteurs qui offrent la DQE la plus élevée sont: le détecteur avec plaque avant de Cu d'épaisseur 1.75 mm et de plaque arrière d'Al d'épaisseur 1.62 mm pour le Clinac-18, et le détecteur avec plaque avant de Cu d'épaisseur 0.95 mm et plaque arrière de Cu ou d'Al d'épaisseurs 0.80 mm et 1.62 mm, respectivement, pour le cobalt-60.

## Original Contribution

An extensive set of metal-plate/film detectors have been studied, allowing the measurement of certain detector characteristics at megavoltage energies which have not been reported in the literature. The four original contributions to this thesis have been outlined in the four paragraphs below.

The detector spatial resolution is increased by using a low density, low atomic number back plate such as Al. This back plate is required to shield the detector film from room scatter while contributing minimally to backscatter.

The spatial resolution of metal-plate/film detectors appears to dependent on the density and thickness of both the front and back plates used. The front and back plates act as coupled entities in terms of their effect on the spatial resolution of the system. The results suggest that, as the thickness of the Cu or Pb front plate increases, the spatial resolution increases with a decrease in thickness of the Al back plate. A limit in the front plate thickness is reached when a detector without back plate gives the best spatial resolution. The maximum thickness of the front plate at which this situation occurs is 2.5 to 3.5 times the average maximum range of the electrons within the front plate. Thus, given a Cu or Pb front plate whose thickness is below this maximum thickness, there will be a characteristic low density, back plate thickness that optimizes the spatial resolution.

We show that when the thickness of a given front plate type is greater than the maximum range of the electrons within the front plate, the spatial resolution of the detector can only worsen due to the increased photon scatter from the thickness of the front plate that is greater than this range.

We also show that below spatial frequencies of 1 cycle/mm, the noise power, when plotted as a function of optical density (D), has a maximum of  $3.8 \times 10^{-5} \text{ mm}^2$  at  $\sim 1.3 D$ . This suggests that there is a limit to the increase in the noise power with increased high energy, photon exposures.

## Acknowledgments

I sincerely thank my supervisor and teacher Dr. B. Gino Fallone for the constant concern, patience, direction and encouragement he offered throughout the duration of the research.

I am also grateful to Mr. Corey Zankowski for the time he spent in teaching me the basics of the EGS4 monte carlo simulation package. Likewise, I am deeply indebted to Mr. Steve D. Donoghue who patiently showed me how to use their impressive, robust microdensitometer and was always around for any queries. As well, I am grateful to Captain Philip Edwards who was instrumental in giving me access to the microdensitometer at the National Defense Canadian Forces Photographic Unit.

I would also like to extend my gratitude to my colleague Mr. Dimitri Hristov with whom I had numerous, invaluable discussions. I would also like to thank the entire McGill Medical Physics staff, in particular Dr. E. B. Podgorsak, Dr. L. J. Schriener, Dr. C. Pla and Dr. B. G. Fallone for their teaching devotions toward fashioning the best Medical Physicists.

The unrelenting support of my family, friends and girlfriend is deeply appreciated. Therefore, last but not least, I would like to thank my parents Nunzio and Maria, my siblings Anna Franca and Mikey, my grandparents 'nonna' Anna and 'nonni' Falco, and my love Katia. This thesis is dedicated to my late uncle Antonio ('zio' Tonino) who died from cancer. He was a strong and loving man whose love of life was unmatched.

## List of Figures

<b>Figure 2.1</b>	<i>Discontinuous spatial frequency chart showing resolutions ranging from 0.6 to 5 line pairs per mm (lp/mm).</i>	10
<b>Figure 2.2</b>	<i>The linear system acting on some input object.</i>	11
<b>Figure 2.3</b>	<i>Schematic representation of the degradation of a delta source object due to a detector system.</i>	12
<b>Figure 2.4</b>	<i>Invariant and non-invariant systems.</i>	14
<b>Figure 2.5</b>	<i>Three microdensitometer traces scanned from a nominally, uniformly exposed film using three different aperture slit sizes.</i>	20
<b>Figure 2.6</b>	<i>Spectral estimate for 4950 samples of white noise along with the average of 33 spectra derived from the 4950 points.</i>	26
<b>Figure 2.7</b>	<i>Microdensitometer calibration curve.</i>	30
<b>Figure 2.8</b>	<i>Ideal array of detectors of area <math>a</math>, scanned with an aperture of size <math>A</math>.</i>	32
<b>Figure 2.9</b>	<i>The <math>(S/N)</math> transfer system.</i>	37
<b>Figure 2.10</b>	<i>LSF being sampled at intervals of <math>\Delta x</math>.</i>	39
<b>Figure 2.11</b>	<i>Effect on the spacing between repeated MTFs if the sample spacing of the sampled image is increased.</i>	40
<b>Figure 2.12</b>	<i>Sinc functions corresponding to several rectangular aperture widths: 1 mm; 100 <math>\mu\text{m}</math>; 10 <math>\mu\text{m}</math>; and 1 <math>\mu\text{m}</math>.</i>	41
<b>Figure 3.1</b>	<i>Block diagram for the experimental and processing techniques used to determine the MTF of the metal-plate/film detectors.</i>	48
<b>Figure 3.2</b>	<i>Spectra emitted by the Clinac-18 therapy machine in the 10 MV photon mode.</i>	52
<b>Figure 3.3</b>	<i>RP film characteristic curves obtained on four separate days with the two therapy machines.</i>	53
<b>Figure 3.4</b>	<i>Microdensitometer calibration curve.</i>	54

<b>Figure 3.5</b>	<i>Typical raw data LSF image showing background noise caused mainly by the film granularity.</i>	55
<b>Figure 3.6</b>	<i>Distorted LSF due to the fact that the scanning motion is not perfectly perpendicular to the slit image.</i>	56
<b>Figure 3.7</b>	<i>Distortions in the shape of the averaged LSF due to shifts in the relative positions of the peaks of each successive LSF.</i>	57
<b>Figure 3.8</b>	<i>Typical averaged LSF.</i>	58
<b>Figure 3.9</b>	<i>NPS values versus scanning slit length.</i>	64
<b>Figure 4.1</b>	<i>MTFs for detectors with Cu(0.95 mm) front plates and with varying thicknesses of Al back plates or without a back plate.</i>	78
<b>Figure 4.2</b>	<i>MTFs for detectors with Cu(1.75 mm) front plates and with varying thicknesses of Al, Cu, or Pb back plates or without a back plate.</i>	78
<b>Figure 4.3</b>	<i>MTFs for detectors with Cu(2.40 mm) front plates and with varying thicknesses of Al back plates or without a back plate.</i>	80
<b>Figure 4.4</b>	<i>MTFs for detectors with Pb(0.39 mm) front plates and with an Al(1.62 mm) back plates or without a back plate.</i>	80
<b>Figure 4.5</b>	<i>Modulation Transfer Functions for detectors with Pb(1.10 mm) front plates and with varying thicknesses of Al back plates or without a back plate.</i>	81
<b>Figure 4.6</b>	<i>MTFs for detectors with Pb(1.31 mm) front plates and with varying thicknesses of Al, Cu, or Pb back plates or without a back plate.</i>	82
<b>Figure 4.7</b>	<i>Modulation Transfer Functions for detectors with Pb(2.05 mm) front plates and with an Al(1.62 mm) back plate or without a back plate.</i>	82
<b>Figure 4.8</b>	<i>MTFs for detectors with brass(3.07 mm) front plates and with varying thicknesses of Al, Cu, or Pb back plates or without a back plate.</i>	83
<b>Figure 4.9</b>	<i>Modulation Transfer Functions for detectors with Al(3.22 mm) front plates and with varying thicknesses of Cu, or Pb back plates.</i>	84
<b>Figure 4.10</b>	<i>MTFs for detectors without front plates and with varying thicknesses of Al, Cu, Pb, or brass back plates or without a back plate.</i>	84
<b>Figure 4.11</b>	<i>MTFs for the best detectors from each of Figs. 4.1 to 4.10.</i>	86
<b>Figure 4.12</b>	<i>MTFs for detectors with Cu(0.95 mm) front plates and with varying thicknesses of Al back plates or without a back plate.</i>	89

<b>Figure 4.13</b>	<i>MTFs for detectors with Cu(1.75 mm) front plates and with varying thicknesses of Al , Cu , or Pb back plates or without a back plate.</i>	89
<b>Figure 4.14</b>	<i>Modulation Transfer Functions for detectors with Cu(2.40 mm) front plates and with varying thicknesses of Al back plates or without a back plate.</i>	90
<b>Figure 4.15</b>	<i>Modulation Transfer Functions for detectors with Pb(0.39 mm) front plates and with varying thicknesses of Al back plates without back plate.</i>	91
<b>Figure 4.16</b>	<i>Modulation Transfer Functions for detectors with Pb(1.10 mm) front plates and with varying thicknesses of Al back plates or without a back plate.</i>	91
<b>Figure 4.17</b>	<i>Modulation Transfer Functions for detectors with Pb(1.31 mm) front plates and with varying Al , Cu , or Pb back plates or without a back plate.</i>	92
<b>Figure 4.18</b>	<i>Modulation Transfer Functions for detectors with Pb(2.05 mm) front plates and with Al back plates or without a back plate.</i>	93
<b>Figure 4.19</b>	<i>MTFs for detectors with brass(3.07 mm) front plates and with varying thicknesses of Al , Cu , or Pb back plates or without back plates.</i>	93
<b>Figure 4.20</b>	<i>Modulation Transfer Functions for detectors with Al(3.22 mm) front plates and with varying thicknesses of Cu , or Pb back plates.</i>	94
<b>Figure 4.21</b>	<i>MTFs for detectors without front plates and with varying thicknesses of Al , Cu , Pb , or brass back plates or without a back plate.</i>	94
<b>Figure 4.22</b>	<i>Modulation Transfer Functions for the best detectors from each of the last ten figures (i.e., 4.12 to 4.21).</i>	96
<b>Figure 4.23</b>	<i>Noise Power Spectra for detectors with Al(1.62 mm) back plates and varying thicknesses of Cu , Pb , or brass front plates or without a front plate.</i>	98
<b>Figure 4.24</b>	<i>Noise Power Spectra for detectors with Cu(1.75 mm) front plates and varying thicknesses of Al , Cu , or Pb back plates or without a back plate.</i>	98
<b>Figure 4.25</b>	<i>Noise Power Spectra for detectors with Pb(1.10 mm) back plates and varying thicknesses of Al , Cu , Pb , or brass front plates or without a front plate. Also shown is the NPS for the film without metal-plates.</i>	99
<b>Figure 4.26</b>	<i>Noise Power Spectra for the (none; Pb, 1.10) detector where the nominally, uniform film densities used were 1.00, 0.69, and 0.52 optical density.</i>	101
<b>Figure 4.27</b>	<i>Optical density versus NPS at four spatial frequencies values: 0.39, 1.57, 3.92, and 8.23 cycles/mm.</i>	101

<b>Figure 4.28</b>	<i>Noise Power Spectra for detectors with Al(1.62 mm) back plates and varying thicknesses of Cu, Pb, or brass front plates or without a front plate.</i>	102
<b>Figure 4.29</b>	<i>Noise Power Spectra for detectors with Cu(1.75 mm) front plates and varying thicknesses of Al, Cu, or Pb back plates or without a back plate.</i>	103
<b>Figure 4.30</b>	<i>Noise Power Spectra for detectors with Pb(1.10 mm) back plates and varying thicknesses of Al, Cu, Pb, or brass front plates or without a front plate. Also shown is the NPS film without metal-plates.</i>	103
<b>Figure 4.31</b>	<i>Noise Power Spectra for the (none; Pb, 1.10) detector where the nominally, uniform film densities used were 1.00, 1.27, and 1.81 optical density.</i>	104
<b>Figure 4.32</b>	<i>Noise Power Spectrum versus film optical density for four spatial frequencies: 0.39, 1.57, 3.92, and 8.23 cycle/mm</i>	105
<b>Figure 4.33</b>	<i>DQE for detectors with Al(1.62 mm) back plates and varying thicknesses of Cu, Pb, or brass front plates or without a front plate.</i>	106
<b>Figure 4.34</b>	<i>DQE for detectors with Cu(1.75 mm) front plates and varying thicknesses of Al, Cu, or Pb back plates or without a back plate.</i>	107
<b>Figure 4.35</b>	<i>DQE for detectors with Pb(1.10 mm) back plates and varying thicknesses of Al, Cu, Pb, or brass front plates or without a front plate. Also shown is the film without metal-plates.</i>	107
<b>Figure 4.36</b>	<i>DQE for detectors with Al(1.62 mm) back plates and varying thicknesses of Cu, Pb, or brass front plates or without a front plate.</i>	109
<b>Figure 4.37</b>	<i>DQE for detectors with Cu(1.75 mm) front plates and varying thicknesses of Al, Cu, or Pb back plates or without back plates.</i>	110
<b>Figure 4.38</b>	<i>DQE for detectors with Pb(1.10 mm) back plates and varying thicknesses of Al, Cu, Pb, or brass front plates or without a front plate. Also shown is the DQE for film alone.</i>	110
<b>Figure A.1</b>	<i>Microdensitometer scan modes.</i>	122

## List of Tables

<b>Table 2.1</b>	<i>Digitization specifications.</i>	42
<b>Table 3.1</b>	<i>Front and back metal-plate combinations used with the RP portal localization film.</i>	51
<b>Table 3.2</b>	<i>Detectors used in the NPS determination, also listed are the MUs and/or irradiation time and SDD parameters used to generate a uniform optical density of 1.00 on the portal film.</i>	62
<b>Table 3.3</b>	<i>Example of Roger's tables.</i>	69
<b>Table 3.4</b>	<i>The absolute dose at a 5 cm depth within tissue and the absolute photon fluence at the surface, for the detectors and parameters listed in Table 3.2.</i>	71
<b>Table B.1</b>	<i>Actual scanning aperture sizes offered by the Micro-10 PDS microdensitometer.</i>	126

# TABLE OF CONTENTS

Abstract .....	ii
Résumé .....	iii
Original Contribution .....	iv
Acknowledgments .....	v
List of Figures .....	vi
List of Tables.....	x
Table of Contents.....	xi
<b>1 Introduction</b> .....	<b>1</b>
1.1 General Introduction .....	1
1.2 Thesis Organization .....	4
References .....	6
<b>2 Theory</b> .....	<b>9</b>
2.1 Measures of System Performance .....	9
2.1.1 Brief overview: Contrast and noise.....	9
2.1.2 Brief overview: Resolution .....	10
2.1.3 Transfer Theory .....	11
2.1.3.1 Point Spread Function (PSF).....	11

2.1.3.2	Line Spread Function (LSF)	14
2.1.3.3	Modulation Transfer Function (MTF)	16
2.1.4	Noise Power Spectrum (NPS)	18
2.1.4.1	Introduction	18
2.1.4.2	First-order statistics	20
2.1.4.3	Second-order statistics: The autocorrelation function	21
2.1.4.4	Error reduction in estimation of Wiener Spectra	25
2.1.4.5	Obtaining a $1 - d$ scan from $2 - d$ data	27
2.1.4.6	Callier coefficient	29
2.1.5	Detective Quantum Efficiency (DQE)	31
2.1.5.1	Introduction	31
2.1.5.2	Microscopic view	31
2.1.5.3	Macroscopic view	32
2.1.6	Signal-to-Noise Ratio	36
2.1.7	Noise-Equivalent Number of Quanta (NEQ)	37
2.2	Effects of Digitization	38
2.2.1	Introduction	38
2.2.2	Truncation artifacts	38

2.2.3 Aliasing artifacts .....	39
References .....	43
<b>3 Materials and Methods</b>	<b>46</b>
3.1 Measuring the Modulation Transfer Function .....	46
3.1.1 Introduction .....	46
3.1.2 Experimental techniques .....	49
3.1.2.1 Obtaining LSF images .....	49
3.1.2.2 Film H & D curves .....	52
3.1.3 Processing techniques .....	53
3.1.3.1 LSF digitization .....	53
3.1.3.2 Linearization and Callier effect corrections .....	54
3.1.3.3 Processing the digitized, linearized LSF .....	55
3.1.3.4 Corrections applied in the Fourier domain .....	58
3.2 Measuring the Noise Power Spectrum .....	61
3.2.1 Experimental techniques .....	61
3.2.2 Processing techniques .....	61
3.2.2.1 Digitizing the film-uniformly exposed to 1.00 D .....	61
3.2.2.2 Synthesizing an 8 mm by 30 $\mu\text{m}$ scanning slit .....	63

3.2.2.3 'Section' scan Noise Power Spectra .....	65
3.3 Determining fluence parameter $\bar{q}$ .....	68
3.4 Microdensitometer: Brief overview .....	71
References .....	73
<b>4 Results and Discussion</b>	<b>76</b>
4.1 Modulation Transfer Function .....	76
4.1.1 Clinac-18: Modulation Transfer Functions .....	76
4.1.1.1 Comparing front plates .....	85
4.1.2 Cobalt-60: Modulation Transfer Functions .....	88
4.1.2.1 Comparing front plates .....	95
4.2 Noise Power Spectrum results .....	96
4.2.1 Clinac-18: Noise Power Spectra .....	97
4.2.2 Cobalt-60: Noise Power Spectra .....	102
4.3 Detective Quantum Efficiency results .....	105
4.3.1 Clinac-18: Detective Quantum Efficiency .....	105
4.3.2 Cobalt-60: Detective Quantum Efficiency .....	108
References .....	112
<b>5 Conclusion</b>	<b>114</b>

**APPENDIX A** **118**

A.1 Microdensitometer function and operation specifications .....118

    A.1.1 Functionality .....118

    A.1.2 Components and operational specifications .....119

        A.1.2.1 Optics .....119

        A.1.2.2 Source section .....119

        A.1.2.3 Sensor section .....120

        A.1.2.4 Film stage .....121

        A.1.2.5 Scanning .....122

        A.1.2.6 Microprocessor .....123

        A.1.2.7 Scanning set up procedures .....124

**APPENDIX B** **126**

B.1 Microdensitometer scanning aperture sizes .....126

**BIBLIOGRAPHY** **127**

# INTRODUCTION

## 1.1 General Introduction

When external beam radiation therapy is used to control or to abate a tumorous mass, extreme care must be taken to irradiate the anatomical region prescribed for treatment while limiting the amount of radiation that is received by the surrounding healthy tissue. During therapy imaging (also known as therapy localization, therapy verification, or portal imaging) the patient is imaged with the high energy, X-ray therapy beam just prior to treatment. This is used to ensure that displacements of the actual treatment field with respect to the intended treatment tumor volume (i.e., localization errors) can be identified and corrected.

The steps involved with patient treatment with the therapy machine can be summarized as follows: First, the patient is imaged with a *simulator*, which is a system which has all of the degrees of freedom of a true therapy machine except that it uses a diagnostic X-ray tube as its source of photons. These photons are of much lower energies (30 - 110 keV) than the maximum therapy photon energies used (1 - 25 MeV) which results in high-contrast images not possible with therapy photons. The quality of the simulator images must be optimal since it is from these images that the radiation oncologist delineates

the tumorous regions that must be treated, and those that must be shielded (i.e., vital organs). Second, the radiation oncologist prescribes a dose to the tumor and the simulator data is sent to *treatment planning*. The appropriate treatment setup parameters (such as, X-ray source to surface distance (SSD), beam energy, field size, bolus, attenuating blocks, multiple beam treatments, etc...) are then established. Finally, the patient is brought to the treatment room to receive the prescribed dose in a controlled manner. It is important that the exact geometric setup that was considered optimum at the simulator procedure be reproduced at the actual therapy treatment unit.

The geometric set up at the treatment machine is guided in most cases by marking the prescribed treatment region on the patient's skin with a dye during the simulator process. These markings are used for the whole treatment which may consist of as many as forty fractionations or treatments to the therapy machine, with perhaps one fractionation per day. This verification technique is not sufficient because the treatment can last over several months and during this time the patient can lose considerable weight, causing the anatomy to shift in terms of the skin markings. Due to the high frequency of patient treatments in a day, accuracy in the geometric set up can be compromised if: (1) shielding blocks are placed improperly; (2) subtle patient positioning errors occur; (3) the radiation treatment machine is misaligned; (4) wedges are placed incorrectly into the tray holder; and (5) patient motion occurs during treatment which can cause underdose in the region of interest. Errors associated with the use of external markings for verification have been studied at length<sup>1-9</sup>.

Clinical studies concerned with the accuracy of placing the actual radiation field edges onto the prescribed field edges resulted in deviations of the order of 1-2 cm<sup>9-11</sup>. Studies have also shown that localization errors can lead to local recurrences at the edges of the treatment fields and suggest that the deviations should not exceed 5 mm<sup>12-13</sup>. It has been reported that a 5 mm reduction in placement errors could result in 10-20 % improvement in tumor control<sup>12-13</sup>. Furthermore, the literature suggests that local recurrence rates of cancer are caused by geometric localization errors at the time of treatment<sup>3,6,10-11,13-14</sup>. It has also been estimated that nearly 33 % recurrence rates in patients are due to localization errors at time of treatment<sup>3,15-17</sup>. These findings require that proper quality assurance procedures be performed in radiation therapy. Thus, an additional step is used just before and during treatment. A portal image is obtained by exposing the image receptor to the radiation beam emanating from the portal of a therapy

unit. Several authors have shown that an increase in the use of portal imaging has decreased the frequency of localization errors<sup>5,7,12-14</sup> which implies better tumor control.

Two types of portal films are generally used with slightly different purposes and method of application. A localization portal film is used to image the patient after set up but before treatment. This film is used to determine whether the patient's position on the couch should be altered to align the treatment and prescribed field. The radiation energy delivered to the patient during the portal image acquisition stage is insignificant as compared to the amount that the patient will receive during treatment. The other type of portal film is called a verification film, which is an extremely slow film as compared to the localization film and is kept below the couch during the time of each fractional treatment, and is used to check the overall exposure of the patient and to see if any significant patient motion has occurred throughout the treatment. In all cases, the portal films are placed between metal-plates and/or fluorescent screens to increase the number of electrons and photons generating the image on the film (intensification factor), to remove electron scatter generated by the patient, and to shield the film from photon scatter in the room which would otherwise degrade the film image quality.

Unfortunately, there are two main drawbacks to the use of portal films: (1) it is a very time consuming process for the radiation oncologist to locate recognizable details in the portal film low-contrast image which is then matched to the initially delineated prescription field of simulation standard; and (2) delays are encountered in the development of the portal films. Consequently, portal films are never taken for each treatment setup but only once or twice during the whole series of treatments. Many times several fractionation treatments have already been administered to the patient before portal films are actually taken. As a result, there has been considerable effort invested to develop digital, on-line therapy imaging systems as alternatives to film. These systems (1) eliminate delays associated with film; (2) allow positional checks after corrections for localization errors are made; and (3) would permit digital manipulation of the images through image enhancing tools to, for example, more accurately determine edges of structures in the images and thus enhance image contrast.

Boyer *et. al.*<sup>18</sup> give a very complete description of different types of on-line electronic portal imaging devices (EPIDs) that have been under development for some time. These devices extract as much information as possible from the low inherent subject contrast of therapy energies, as well as eliminate the time delay problems offered by portal

films. EPIDs are based on the following technologies: video-based systems<sup>19-25</sup>, scanning liquid ionization chambers<sup>26-29</sup>, and solid-state systems<sup>29-31</sup>. The on-line characteristics of these devices and the fact that the images can be obtained in real time makes them very appealing. Nevertheless, portal films (metal-plate/film combinations) are still a commonly used form of geometric setup control practiced in radiotherapy centers. Thus it is important to investigate this particular therapy imaging modality.

There are two goals to this thesis: First, the imaging quality of the metal-plate/film portal imaging detectors is quantified through the measurement of imaging parameters such as Modulation Transfer Function (MTF), Noise Power Spectrum (NPS), and Detective Quantum Efficiency (DQE). There have been several studies on the resolution and signal-to-noise characteristics of this most commonly used type of therapy imaging detector<sup>32-35</sup>, but none of these studies have been very extensive. This thesis will review the techniques used to determine these imaging parameters, and show results of an extensive study of the imaging characteristics of forty-nine front and back metal-plate detector combinations. The metal plates considered are aluminum (Al), copper (Cu), brass, and lead (Pb) ranging in thicknesses from 0.30 to 4.80 mm. This endeavor was carried out on two therapy machines (i.e., the Co - 60 unit and the Clinac-18 machine in its 10 MV X-ray mode). From these imaging parameters (MTF, NPS, and DQE), we can deduce some of the influences that the metal-plate thickness, density, atomic number, and different back and front plate combinations have on image quality. Second, we wish to determine the portal imaging metal-plate/film combination that will achieve the best quality portal images.

## **1.2 Thesis Organization**

The thesis is divided into the following chapters:

Chapter 2 is the theoretical section dealing with (1) the development of the methods that are generally used for describing imaging characteristics of radiation detectors. System resolution (MTF) and noise (NPS) will be discussed and formulae for the quantification of these imaging properties will be derived in the spatial frequency domain. The final goal of this section is to derive the Detective Quantum Efficiency (DQE) in the frequency domain. This absolute quantity combines all of the resolution and noise properties of a detector and is used to compare different radiation detectors. We will also review (2) the ramifications of using the digitized samples of our analog film data, in terms of the fidelity of the

sampled information as compared to the information contained in the analog form. Techniques that are used to correctly sample the analog film data are discussed.

Chapter 3 deals with (1) the experimental methods and materials used to acquire the analog data sets; (2) the computer processing procedures used to analyze the digital data to determine the imaging parameters discussed above; and, (3) the description of the microdensitometer system used to digitize the original analog data sets so that step (2) could be performed.

Chapter 4 discusses the results relating to the resolution, noise properties and overall imaging efficiencies of the forty-nine portal metal-plate/film detectors studied with the two different therapy energies. Limitations in imaging due to film graininess, detector metal-plate thicknesses, and composition are explored, along with recommendations for the best metal-plate/film detector combination that should be used.

Chapter 5 includes the summary and conclusions.

## References:

- <sup>1</sup> Task Group 28, "Radiotherapy Portal Imaging Quality: AAPM Report #24," *American Institute of Physics*, New York, (1987).
- <sup>2</sup> Svensson, G.K., "Quality Assurance in radiation therapy: Physics efforts," *Int. J. Radiation Oncol. Biol. Phys. sup. 1*, 10, 23-29, (1984).
- <sup>3</sup> Marks, J.E., Haus, A.G., Sutton, G.H., and Griem, M.L., "Localization error in the radiotherapy of Hodgkin's disease and malignant lymphoma with extended mantle fields," *Cancer*, 34, 83-90, (1974).
- <sup>4</sup> Marks, J.E., Davis, M.K., and Haus, A.G., "Anatomic and geometric precision in radiotherapy," *Radiologia Clinica et Biologica*, 43(1), 1-20, (1974).
- <sup>5</sup> Marks, J.E., Haus, A.G., Sutton, G.H., and Griem, M.L., "The value of frequent treatment verification films in reducing localization error in the irradiation of complex fields," *Cancer*, 37, 2755-2761, (1976).
- <sup>6</sup> Gelinas, M., and Fletcher, G.H., "Incidence and causes of local failure of irradiation in squamous cell carcinoma of the faucial arch, tonsillar fossa and base of the tongue," *Radiology*, 108(2), 383-7, (1973).
- <sup>7</sup> Haus, A.G., and Marks, J.E., "Detection and evaluation of localization errors in patient radiation therapy," *Invest. Radiol.*, 8(6), 384-391, (1973).
- <sup>8</sup> Dunscombe, P.B., and Fox, K., "Precision of determining compliance with prescribed fields from conventional portal films," *British J. Radiol.*, 62, 935-939, (1980).
- <sup>9</sup> Huizenga, H., Levendag, P.C., De Porre, P.M., and Visser, A.G., "Accuracy in radiation field alignment in head and neck cancer: A prospective study," *Radiotherapy and Oncology*, 11, 181-187, (1988).
- <sup>10</sup> Rabinowitz, I., Broomberg, J., Gointein, M., McCarthy, K., and Leong, J., "Accuracy in radiation field alignment in clinical practice," *Int. J. Radiat. Oncol. Biol. Phys.*, 11, 1957-1967, (1985).
- <sup>11</sup> Byhardt, R.W., Cox, J.D., Hornburg, A., and Liermann, G., "Weekly localization films and detection of field placement errors," *Int. J. Radiat. Oncol. Biol. Phys.*, 4, 881-887, (1978).
- <sup>12</sup> Gointein, M., and Busse, J., "Immobilization error: some theoretical considerations," *Radiology*, 117, 407-412, (1975).
- <sup>13</sup> Brahme, A., "Dosimetric precision requirement in radiation therapy," *Acta. Radiol. Oncol.*, 23, 379-391, (1984).
- <sup>14</sup> Verhey, L.V., Gointein, M., McNulty, P., Munzenrider, J.E., and Suit, H.D., "Precise positioning of patients for radiation therapy," *Int. J. Radiat. Oncol. Biol. Physics*, 8, 289-294, (1982).

- 15 Kinzie, J.J., Hanks, G.E., Maclean, C.J., and Kramer, S., "Patterns of care study: Hodgkin's disease relapse rates and adequacy of portals," *Cancer*, 52, 2223-2226, (1983).
- 16 Maruyama, Y., and Khan, F., "Blocking considerations in mantle therapy," *Radiology*, 101, 167-173, (1971).
- 17 Suit, H.D., in *Proceedings of the conference on time and dose relationships in radiation biology as applied to radiotherapy*, Brookhaven National Laboratories Publication #50203, (1970).
- 18 Boyer, A.L., Antonuk, L., Fenster, A., Van Herk, M., Meertens, H., Munro, P., Reinstein, L.E., Wong, J., "A review of electronic portal imaging devices (EPIDs)," *Medical Physics*, 19(1), 1-16, (1992).
- 19 Bailey, N.A., Horn, R.A., and Kamp, T.D., "Fluoroscopic visualization of megavoltage therapeutic x ray beams," *Int. J. Radiat. Oncol. Biol. Phys.*, 6, 935, (1980).
- 20 Munro, P., Rawlinson, J. A., and Fenster, A., "Therapy Imaging: A signal-to-noise analysis of a fluoroscopy imaging system for radiation therapy localization," *Medical Physics*, 17(5), 763-772, (1990).
- 21 Leong, J., "Use of digital fluoroscopy as an on-line verification device in radiation therapy," *Phys. Med. Biol.*, 31, 985-992, (1986).
- 22 Shalev, S., Lee, T., Leszczynski, K., Cosby, S., and Chu, T., "Video techniques for on-line portal imaging," *Comp. Med. Img. Graph.*, 13, 217-226, (1989).
- 23 Visser, A.G. , Huizenga, H., Althof, V.G.M., and Swanenburg, B.N., "Performance of a prototype fluoroscopic radiotherapy imaging system," *Int. J. Radiat. Oncol. Biol. Phys.*, 18, 43-50, (1990).
- 24 Munro, P., Rawlinson, J.A., and Fenster, A., "A digital fluoroscopic imaging device for radiotherapy localization," *Proc. SPIE* 1090, 321-329, (1989).
- 25 Wong, J.W., Binns, W.R., Cheng, A.Y., Gear, L.Y., Epstein, J.W., Klarmann, J., and Prudy, J.A., "On-line radiotherapy imaging with an array of fiber-optic image reducers," *Int. J. Rad. Oncol. Bio. Phys.*, 18, 1477-1484, (1990).
- 26 Van Herk, M., and Meertens, H., "A matrix ionization chamber imaging device for on-line patient setup verification during radiotherapy," *Radiother. Oncol.*, 11, 369-378, (1988).
- 27 Meertens, H., van Herk, M., Bijhold, J., and Bartelink, H., "First clinical experience with a newly developed electronic portal imaging device," *Int. J. Rad. Oncol. Biol. Phys.*, 18, 1173-1181, (1990).
- 28 Van Herk, M., "Physical aspects of a liquid filled ionization chamber with pulsed polarizing voltage," *Medical Physics*, 18, 692-702, (1991).

- 29 Taborsky, S.c., Lam, W.C., Sterner, R.E., and Skarda, G.M., "Digital imaging for radiation therapy verification," *Opt. Eng.*, 21, 888-893, (1982).
- 30 Morton, E.J., Swindell, W., Lewis, D.G., and Evans, P.M., "A linear scintillation-crystal photodiode detector for radiotherapy imaging," *Medical Physics*, 18, 681-691, (1991).
- 31 Antonuk, L.E., Yorkston, J., Boudry, J., Longo, M.L., Jimenez, J., and Street, A., "Development of hydrogenated amorphous silicon sensors for high-energy photon radiotherapy imaging," *IEEE Trans. Nucl. Sci.*, NS-37(2), 165-170, (1990).
- 32 Droege, R. T., Bjärngard, B. E., "Metal screen-film detector MTF at megavoltage x-ray energies," *Medical Physics*, 6(6), 515-518, (1979).
- 33 Munro, P., Rawlinson, J. A., and Fenster, A., "Therapy Imaging: A signal-to-noise analysis of metal plate/film detectors," *Medical Physics*, 14(6), 975-984, (1987).
- 34 Droege, R., T., "A megavoltage MTF measurement technique for metal screen - film detectors," *Medical Physics*, 6(4), 272-279, (1979).
- 35 Wowk. B., Radcliffe. T., Leszczynski, K.W., Shalev, S., and Rajapakshe, R., "Optimization of metal/phosphor screens for on-line portal imaging," *Medical Physics*, 21(2), 227-235, (1994).

# THEORY

## 2.1 Measures of System Performance

### 2.1.1 Brief overview: Contrast and noise

We are concerned with the quality of imaging systems whose input stage is electromagnetic radiation. The source of information for these types of imaging systems comes from the spatial distribution of the photons which have been modulated by a patient situated between the photon source and the imaging system. Subject contrast is related to the difference between the photon intensity transmitted through one part of the patient as compared to that transmitted through another part. Because information is collected through some photon detector system, subject contrast is transformed to image contrast or to radiographic contrast<sup>1</sup> if the detector system is film.

If the area of an image is divided into  $n$  squares or  $n$  picture elements (pixels), image contrast  $C$  can be defined as<sup>2</sup>

$$C = \frac{P_i - P_s}{P_s} \quad (2.1)$$

where  $P_i$  and  $P_s$  are the number of photons in the pixel of interest and the average number of photons in the surrounding pixels, respectively.

Several main factors contribute to the image contrast: subject contrast, scattered radiation, and system contrast. System contrast refers to the sensitivity of the detector to the range of photon energy densities it receives. At therapy energies scatter radiation is primarily due to the Compton scattering effect. Scattered radiation at the imaging plane increases with subject thickness, field size, and decrease in distance between the exit side of patient and imaging plane, among other factors<sup>1,3</sup>. Photons are subject to random variations in time and in space; their spatial and temporal distribution can be estimated by Poisson statistics. The stochastic nature of radiation beams implies a theoretical limit to the lowest subject contrast that can be detected. If the subject contrast is less than the fluctuations of the number of photons per unit area, the corresponding structure will be obscured. Fluctuations, whatever their origin (e.g. scatter radiation, stochastic nature of the radiation source or imperfections in the imaging system), that degrade the image contrast are referred to as noise.

### 2.1.2 Brief overview : Resolution

Historically, resolution has been defined as the measure of the minimum separation of two source points or sources that can be distinguished. Likewise it can be defined as the closest spacing of two lines that can just be distinguished (see Fig. 2.1).

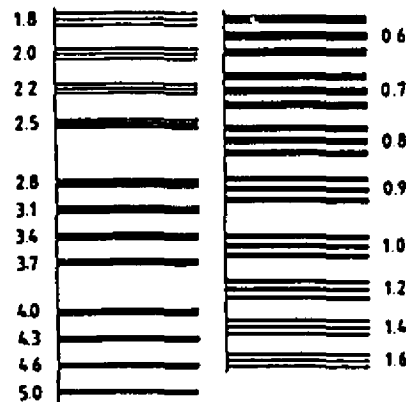


**Figure 2.1** Discontinuous spatial frequency chart showing resolutions ranging from 0.6 to 5 line pairs per mm (lp/mm).

In this case, resolution can be expressed in terms of spatial frequency: line pairs per spatial dimension. The spatial frequencies in the above figure range from 5 line pairs per mm (lp/mm) to 0.6 lp/mm. The Fourier transform conveniently transforms any spatial image to its spatial frequency components (spectrum).

A line pair is resolved, at a particular frequency, if the line pair image contrast exceeds some threshold quantity that is determined by the total noise of the system. Hence, the resolving power of an imaging system depends on contrast as well as noise level. What will follow is a description of physical system performance parameters which we have labeled 'resolution' and 'noise'.

### 2.1.3 Transfer Theory

The basic assumption in the theory of linear systems<sup>4-8</sup> is that a linear relationship exists between the input and the output of a system (see Fig. 2.2).

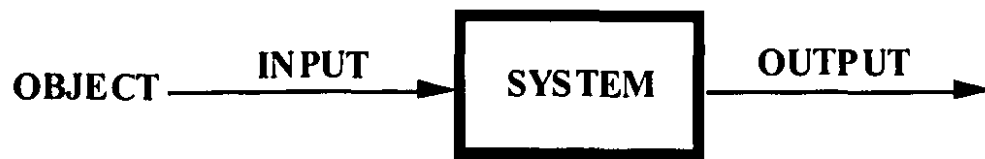


**Figure 2.2** *The linear system affects the output in some well defined manner, given some input object.*

The system, which can be a mechanical, electrical or optical device can be considered a frequency filter. The input signal is represented as a function of frequency and the system attenuates the intensities of certain frequencies.

#### 2.1.3.1 Point Spread Function (PSF)

The ideal imaging system should image the quanta from a point, or delta source in the object plane as an equivalent point in the imaging plane. In reality, some of the radiation from the point object spreads out over an area in the output or imaging plane (Fig. 2.3). The spread out image of the input point object is known as the point spread function (PSF). In the following, co-ordinates with subscript 1 denote the object plane whereas co-ordinates without subscripts correspond to the image plane.

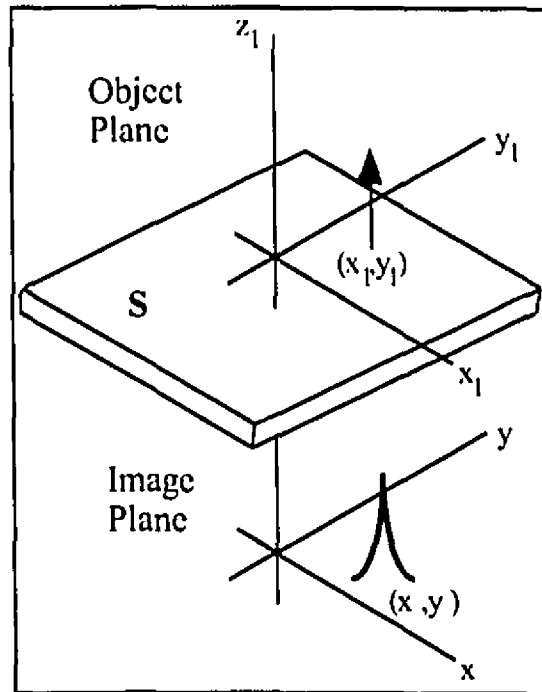


**Figure 2.3** Schematic representation of the degradation of a delta source object due to a system  $S$  (i.e., detector).

Given the system operator denoted by  $S$ , and an input  $f(x_1, y_1)$  then the output of the system is given by

$$g(x, y) = S[f(x_1, y_1)]. \quad (2.2)$$

If the input is a delta source then,

$$h(x, y; x_1, y_1) = g(x, y) = S[\delta(x_1, y_1)] \quad (2.3)$$

which defines the point spread function  $h$ .

Two assumptions which are physically realistic for many practical systems are made to simplify the analysis. The assumptions are that the system is linear and that it is invariant with respect to the position of the object in the object plane. Although the linearity assumption does not hold for photographic film, this problem can easily be corrected.

A linear system implies that if the object plane contains a number of delta function sources, then each of the sources will be imaged as PSFs in the image plane independent of the others. Thus the resulting distribution in the image plane will be the sum of these PSFs. This is the superposition principle of linear systems. If the inputs to a linear system are  $f_1(x_1, y_1)$  and  $f_2(x_1, y_1)$  and if  $a$  and  $b$  are constants then,

$$S\{af_1(x_1, y_1) + bf_2(x_1, y_1)\} = aS\{f_1(x_1, y_1)\} + bS\{f_2(x_1, y_1)\}. \quad (2.4)$$

Equations (2.2), (2.3), and (2.4) imply that the PSF weights the object distribution  $f(x_1, y_1)$  as a scalar multiple. The image distribution for a linear transfer system is thus given by the sum of all of the object points:

$$\begin{aligned} g(x, y) &= S\left\{\int_{-\infty}^{\infty} \int_{-\infty}^{\infty} f(x_1, y_1) \delta(x - x_1) \delta(y - y_1) dx_1 dy_1\right\} \\ g(x, y) &= \int_{-\infty}^{\infty} \int_{-\infty}^{\infty} f(x_1, y_1) S\{\delta(x - x_1) \delta(y - y_1)\} dx_1 dy_1 \end{aligned} \quad (2.5)$$

and using Eq. (2.3)

$$g(x, y) = \int_{-\infty}^{\infty} \int_{-\infty}^{\infty} f(x_1, y_1) h(x, y; x_1, y_1) dx_1 dy_1. \quad (2.6)$$

An invariant system in this case is defined as one where the image of the delta function retains its shape in the imaging plane irrespective of the position of the object in the object plane as is depicted schematically in Fig. 2.4. Mathematically, position invariance is represented by:

$$h(x, y; x_1, y_1) \rightarrow h(x - x_1, y - y_1). \quad (2.7)$$

So that under a position invariant system the intensity of each point of the PSF does not depend on each co-ordinate but on the difference of each co-ordinate. Thus the output of a linear, invariant system is the convolution of the input with the point spread function:

$$g(x, y) = \int_{-\infty}^{\infty} \int_{-\infty}^{\infty} f(x_1, y_1) h(x - x_1, y - y_1) dx_1 dy_1 \quad (2.8)$$

and can also be written as:

$$g(x, y) = f(x_1, y_1) \otimes h(x, y). \quad (2.9)$$

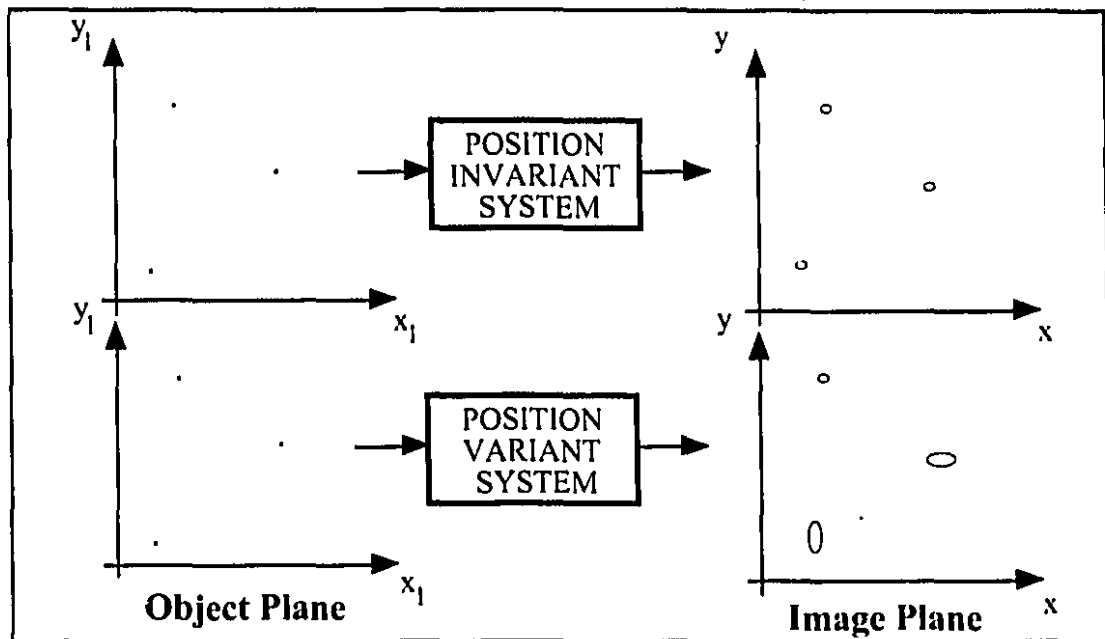


Figure 2.4 Comparing invariant and non-invariant systems.

### 2.1.3.2 Line Spread Function (LSF)

A summary of difficulties involved with measuring the PSF follows: (1) The pinhole that is used to represent the delta point source must be small compared to the source of radiation; (2) this aperture must be perfectly aligned with the center of the source; and (3) due to the low output from the pinhole, the detector system must be exposed for a very long period of time which may cause problems with tube overheating. At megavoltage energies, the pinhole must be of a very thick slab of lead or steel to sufficiently attenuate the beam outside the hole. However, this is very difficult to achieve at these high energies.

These difficulties are avoided by measuring the line spread function (LSF), which is the image of an infinitely long and infinitely narrow line of unit intensity in the object plane. The output of the slit, is much greater than that of a pinhole thus overcoming tube heating problems. It is also technically simpler to manufacture two thick blocks of steel or lead which are then clamped together, with a spacer to form a line in the object plane.

The input line, which lies in the  $y_1$ -direction, may be represented as a one dimensional delta function:

$$f(x_1, y_1) = \delta(x_1). \quad (2.10)$$

The output of the system, using Eq.(2.8) is

$$g(x, y) = I(x) = \int_{-\infty}^{\infty} \int_{-\infty}^{\infty} \delta(x_1) h(x - x_1, y - y_1) dx_1 dy_1 \quad (2.11)$$

and only depends on the  $x$  variable. Using the sifting property of the delta function we have the LSF

$$I(x) = \int_{-\infty}^{\infty} h(x, y_1) dy_1 \quad (2.12)$$

which can be obtained from the PSF by integrating over one variable. The measurement of the LSF is thus equivalent to scanning the PSF with a slit that, relative to the size of the PSF, is narrow in the direction perpendicular to the scan motion ( $x$ ) and long in the scan direction ( $y$ ).

For photographic processes, the PSF is usually rotationally symmetric (isotropic) and can be defined as

$$h(x, y) = h(r), \text{ where } r^2 = x^2 + y^2. \quad (2.13)$$

In this case, the PSF can be defined completely by a radial section or by a LSF.

For the  $1-d$  general case, where the distribution in the object plane is given by  $f(x_1)$ , the output in the image plane  $g(x)$  is given by

$$\begin{aligned} g(x, 0) = g(x) &= \int_{-\infty}^{\infty} \int_{-\infty}^{\infty} f(x_1) h(x - x_1, y_1) dx_1 dy_1 \\ &= \int_{-\infty}^{\infty} \int_{-\infty}^{\infty} f(x - x_1) h(x_1, y_1) dx_1 dy_1 \end{aligned} \quad (2.14)$$

and hence,

$$\begin{aligned} g(x, 0) = g(x) &= \int_{-\infty}^{\infty} f(x - x_1) I(x) dx_1 \\ &= f(x_1) \otimes I(x) \end{aligned} \quad (2.15)$$

Therefore, the LSF defines the system transfer characteristic for the  $1-d$  case, in the same way that the PSF defines the system transfer in the  $2-d$  case.

From elemental transfer characteristics, such as PSF and LSF the output of more complex input distributions can be calculated by evaluating the convolution integrals given by Eqs. (2.9) and (2.15). Since in general it can be difficult to evaluate convolution integrals, a simpler method can be used to describe the transmission of complex signals. This method is based on analyzing the system in the spatial frequency domain rather than the spatial domain.

### 2.1.3.3 Modulation Transfer Function (MTF)

Let us consider the transmission of a sinusoidally varying signal in the  $1-d$  object plane defined by  $f(x_1) = a + b \exp[i(2\pi u x_1 + \alpha)]$ , where  $u$  and  $\alpha$  are the spatial frequency and the phase, respectively. Also,  $a$  and  $b$  are constants which denote the offset and amplitude of the function. The modulation of the input signal  $M_{in}$  and the output signal  $M_{out}$  can be defined as:

$$M_{in} = \frac{\frac{1}{2}(|f_{max}| - |f_{min}|)}{\frac{1}{2}(|f_{max}| + |f_{min}|)} = \frac{b}{a}, \quad (2.16)$$

$$M_{out} = \frac{\frac{1}{2}(|g_{max}| - |g_{min}|)}{\frac{1}{2}(|g_{max}| + |g_{min}|)}$$

Given a sinusoidal input, using Eq. (2.14) and integrating with respect to  $y_1$  the output for a linear, invariant system is the convolution with the LSF

$$g(x) = \int_{-\infty}^{\infty} \int_{-\infty}^{\infty} \{a + b \exp[i(2\pi u(x - x_1) + \alpha)]\} h(x_1, y_1) dx_1 dy_1 \quad (2.17)$$

$$g(x) = \int_{-\infty}^{\infty} l(x_1) \{a + b \exp[i(2\pi u(x - x_1) + \alpha)]\} dx_1$$

which can be written as

$$g(x) = a + b \exp[i(2\pi u x + \alpha)] \int_{-\infty}^{\infty} l(x_1) \exp(-i2\pi u x_1) dx_1 \quad (2.18a)$$

where the area under the LSF is normalized to 1. The integral term is the Fourier transform of the LSF and is called the optical transfer function,  $H(u)$ . Thus Eq. (2.18a) becomes:

$$g(x) = a + b \exp[i(2\pi ux + \alpha)]H(u) \quad (2.18b)$$

where,

$$H(u) = \int_{-\infty}^{\infty} l(x_1) \exp(-i2\pi ux_1) dx_1 = \mathfrak{F}[l(x_1)] \quad (2.19)$$

The optical transfer function can be written in terms of a modulus  $M(u)$  and phase  $\varepsilon(u)$ :

$$H(u) = M(u) \exp[i\varepsilon(u)] \quad (2.20)$$

where,

$$M(u) = |\mathfrak{F}[l(x_1)]|. \quad (2.21)$$

Thus, Eq. (2.18b) becomes,

$$g(x) = a + bM(u) \exp[i(2\pi ux_1 + \alpha + \varepsilon(u))]. \quad (2.22)$$

The output of the system is sinusoidal and has the same frequency as the input. Thus a linear, invariant system affects the input object only in terms of the magnitude of the modulation and phase but not the spatial frequency component itself. From Eq. (2.22) and the output modulation as defined by Eq. (2.16) we obtain:

$$M_{out} = M(u) \frac{b}{a} = M(u)M_{in}. \quad (2.23)$$

$M(u)$ , the modulus of the optical transfer function, thus defines the transfer characteristics of the system in the spatial frequency domain, in the same way that the LSF defined the system transfer characteristics in the spatial domain.  $M(u)$  is called the Modulation Transfer Function (MTF). The MTF is the ratio of the output to the input modulations of any spatial frequencies  $u$  introduced in the imaging system. Note that for a real, symmetric LSF the optical transfer function will be equal to the modulation transfer function, since in Eq. 2.20,  $\exp[i\varepsilon(u)] = 1$ . Since the LSF was normalized to area 1, then

$$M(0) = \left| \int_{-\infty}^{\infty} I(x_1) dx_1 \right| = 1. \quad (2.24)$$

It is advantageous to use the spatial frequency rather than the spatial description of an imaging system because the system transfer is then defined by a simple multiplication (Eq. (2.23)) rather than a more complex convolution (Eq. (2.15)). Thus,

$$\begin{aligned} g(x,y) &= f(x,y) \otimes h(x,y) \\ G(u,v) &= F(u,v)H(u,v) \end{aligned} \quad (2.25)$$

are equivalent 2-*d* expressions where  $(u,v)$  denotes the co-ordinates of the spatial frequency domain,  $F(u,v)$  and  $G(u,v)$  denote the input and output of the system, respectively, and finally  $H(u,v)$  defines the fraction of the spatial frequencies present in the input that are transmitted by the system. Respectively, they are equal to the Fourier transforms of the functions  $f(x,y)$ ,  $g(x,y)$  and  $h(x,y)$ .

Considering the system in the spatial frequency domain, the multiplicative law will be used to facilitate the removal of artifacts caused by the finite size of the sampling aperture of the film scanning microdensitometer, which becomes convolved with the image while scanning (see Section 2.1.4.3). Previously in Section 2.1.2, the unit of spatial frequency was line pairs per mm (lp/mm) because we defined resolution in terms of the closest spacing of two *lines* that can be seen. In this section we defined the basic object as the *sinusoidal*, accordingly, the unit of the spatial frequency domain becomes cycles per mm (cycle/mm).

## 2.1.4 Noise Power Spectrum (NPS)

### 2.1.4.1 Introduction

A system's performance is measured by its abilities to (1) image a point source (i.e., transfer characteristics) and (2) suppress noise (i.e., fluctuations which are random or correlated). The Noise Power Spectrum (NPS) or Wiener spectrum is a quantitative analysis of the noise content of an imaging system as pertaining to the spatial frequency domain.

In the previous analysis of linear, invariant systems (i.e., transfer theory) it was assumed that both the input and the output of the system could be specified exactly. But due to the stochastic nature of the radiation information source and the random nature of photon-grain interactions, a statistical approach is necessary to describe the fluctuations in the input-output signals. Thus, if a section of film is irradiated, the photographic emulsion shows a granular, not a uniform, structure because the image is actually made up of a finite number of grains. Although the individual grains are not seen, the statistical fluctuations in the number of grains per unit area is apparent.

Methods have been devised to measure this randomly occurring non-uniformity in an otherwise nominally, uniformly exposed and processed film. Since system performance is determined by its ability to resolve detail and to lower the noise threshold level, fundamentally the only limitation to radiographic imaging is the noise component. These fluctuations or noise will be analyzed in the same way that other random processes are analyzed, that is, by the variance or the mean-square departure of the noise from its mean<sup>9-12</sup>.

Whereas a deterministic process is described by an ordered set of variables which change according to fixed laws with no uncertainty, a stochastic process is an ordered set of variables that have an uncertain or random nature, but which evolve according to well defined laws of probability. The collection of all of the possible outcomes or realizations of a statistical process is known as the ensemble. The distribution of photons exposing a given area of film is described by a random variable. Thus, the measurements of an optical density profile from a nominally, uniformly exposed film is a good example of a stochastic process. This one scan is a member of the ensemble of all such scans under the identical circumstances (i.e., same film, exposure and development techniques).

In this section we will look at the statistical analysis of the noise from the spatial frequency perspective to gain some insight into the origins of the noise. We also discuss the analytical techniques generally used to obtain noise power spectrum estimates. As was the case for the development of transfer theory in the previous section, we are assuming that the density distribution of a sample of uniformly exposed and uniformly processed film is statistically stationary. That is, the statistics of any region of the sample are the same and are not affected by a shift in the origin. We also assume that a subset of the ensemble density distributions of a uniformly exposed film are statistically representative of the ensemble. A random process which possesses the characteristics above is called ergodic.

### 2.1.4.2 First-order statistics

Figure 2.5 shows three microdensitometer scans of our nominally, uniformly irradiated film using three different aperture settings .

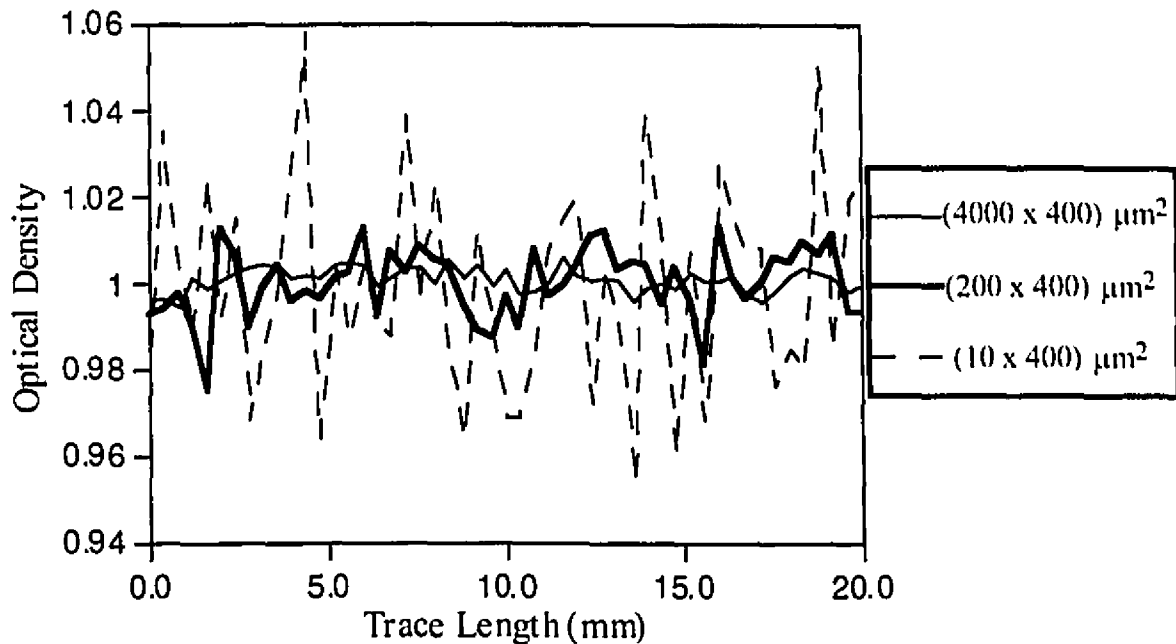


**Figure 2.5** Three microdensitometer traces scanned from a nominally, uniformly exposed film using three different aperture sizes.

The values for each trace can be modeled quite well with a Gaussian distribution. The mean and standard deviation for each aperture setting ( $4000 \times 400 \mu\text{m}^2$ ,  $200 \times 400 \mu\text{m}^2$ , and  $10 \times 400 \mu\text{m}^2$ ) are:  $(1.001 \pm 0.003)$ ,  $(1.000 \pm 0.008)$ , and  $(0.999 \pm 0.023)$  optical density ( $D$ ), respectively. Selwyn<sup>13</sup> used a model of photographic image fluctuations to show that the density fluctuations that are measured with an aperture of some given area should follow a Gaussian distribution. He made two assumption for his derivation: Firstly, he assumed that the aperture area is large with respect to the size of the grains in the emulsion, and secondly, that within the aperture area there are many grains. Previously, in 1913 Nutting<sup>14</sup> demonstrated that the film optical density is proportional to the total number of image grains per unit area. Thus, Selwyn showed that the total number of grains that lie under the aperture will follow a Gaussian distribution and so will the resulting image density according to the Nutting formula<sup>6</sup>. Thus, the mean of the optical density distributions  $\bar{D}$  and the variance  $\sigma^2$  can be used to distinguish, in a quantitative

manner, the three random processes that are shown in Fig. 2.5. For ergodic, stationary processes, the moments of the probability distributions may be expressed as

$$\bar{D} = \frac{1}{N} \sum_{i=1}^N D_i \quad (2.26)$$

$$\sigma_A^2 = \frac{1}{N} \sum_{i=1}^N (D_i - \bar{D})^2. \quad (2.27)$$

The mean density  $\bar{D}$  and the standard deviation  $\sigma_A$  of the density fluctuations are sufficient to specify the properties of noise at one point in the image i.e., first-order statistics of the image noise. We can see from Fig. 2.5 that the standard deviation of the probability distribution is related to the area  $A$  of the aperture used. This is the reason why  $\sigma$  has a subscript  $A$ .

#### 2.1.4.3 Second-order statistics: The autocorrelation function

Generally, the noise in an image has a spatial structure; that is, any two points within the image will be statistically correlated. Second-order statistics of a stationary, ergodic process is used to describe the joint probability that at point  $(x,y)$  the image has density value  $D(x,y)$  and at a point  $(x + \Delta x, y + \Delta y)$  it has a density value of  $D(x + \Delta x, y + \Delta y)$ . The autocorrelation function describes second-order statistics. In general, the autocorrelation function is difficult to define, but for Gaussian processes it is defined completely by the first-joint moment of the second-order probability function, in the same way that first-order statistics are completely described by the  $\bar{D}$  and  $\sigma_A$ . For stationary, ergodic, Gaussian processes, the autocorrelation function is a function of the interval between the sampled points  $(\Delta x, \Delta y)$  and can be defined as follows<sup>15</sup>:

$$c(\Delta x, \Delta y) = \lim_{x,y \rightarrow \infty} \frac{1}{2X} \frac{1}{2Y} \int_{-X}^{+X} \int_{-Y}^{+Y} D(x,y) D(x + \Delta x, y + \Delta y) dx dy. \quad (2.28)$$

It is often more practical to use the autocorrelation of the fluctuations about the mean:

$$c(\Delta x, \Delta y) = \lim_{x,y \rightarrow \infty} \frac{1}{2X} \frac{1}{2Y} \int_{-X}^{+X} \int_{-Y}^{+Y} \Delta D(x,y) \Delta D(x + \Delta x, y + \Delta y) dx dy. \quad (2.29)$$

The autocorrelation function is normalized to the scanned area, where  $2X$  and  $2Y$  are the width and length of the uniformly scanned area, respectively.

The autocorrelation function is a measure of how well the shifted data resembles the unshifted data. Note that the autocorrelation function for the interval  $(0,0)$  reduces to the variance, as is shown in Eq. (2.30).

$$c_{\Delta D}(0,0) = \lim_{x,y \rightarrow \infty} \frac{1}{2X} \frac{1}{2Y} \int_{-X}^{+X} \int_{-Y}^{+Y} \Delta D(x,y)^2 dx dy = \sigma_{\Delta}^2 \quad (2.30)$$

Thus the autocorrelation function completely specifies the first-order and second-order noise statistics for Gaussian, ergodic, stationary processes.

It can be shown<sup>16</sup> that all of the higher-order probability density functions (as well as their moments) associated with Gaussian processes, can be specified in terms of the autocorrelation function. Thus this function defines the ensemble random process. One of the drawbacks of the correlation function is that its shape depends heavily on the aperture that is used to measure the densities at the points  $(x,y)$ , and  $(\Delta x, \Delta y)$ .

If the density fluctuation at the point  $(x,y)$  is  $\Delta D(x,y)$  and a perfect optical system is used to measure this value then the value measured will be  $\Delta D(x,y)$ . Yet, if the aperture and the optical system of the microdensitometer used to make the measurement has a combined point spread function  $h(x,y)$  then the value measured will be  $\Delta D'(x,y)$ . Since the density fluctuations are small about some average value, the microdensitometer system acts as a linear, stationary transfer system. Thus, if at point  $(x,y)$  the input to this system is the actual density fluctuation  $\Delta D(x,y)$  and the output is the measured fluctuation  $\Delta D'(x,y)$ , then, they are related by the convolution relation

$$\Delta D'(x,y) = \int_{-x}^{+x} \int_{-y}^{+y} h(x',y') \Delta D(x-x', y-y') dx' dy' \quad (2.31)$$

and at point  $(x + \Delta x, y + \Delta y)$  by

$$\Delta D'(x + \Delta x, y + \Delta y) = \int_{-x}^{+x} \int_{-y}^{+y} h(x',y') \Delta D(x + \Delta x - x', y + \Delta y - y') dx' dy'. \quad (2.32)$$

Thus the measured autocorrelation function can be derived by inserting Eqs. (2.31) and (2.32) into Eq. (2.29) to obtain:

$$c'(\Delta x, \Delta y) = c(\Delta x, \Delta y) \otimes h(-x, -y) \otimes h(x, y). \quad (2.33)$$

Although the measurement of the autocorrelation function is simple, removing the effects of the measuring aperture from the convolution equation is difficult. In transfer theory, the convolution operation was avoided by treating the system in the spatial frequency domain; this is also the approach we will follow for the autocorrelation function.

If  $D(x, y)$  describes a two dimensional point-by-point density distribution scanned with a microdensitometer, and  $\Delta D(x, y)$  describes the fluctuation component, then from Eq. (2.27) the scanned densities can be defined in terms of the average density:

$$D(x, y) = \bar{D} + \Delta D(x, y). \quad (2.34)$$

This density fluctuation, as seen on a uniformly exposed metal-plate/radiographic film, is known as radiographic mottle. Radiographic mottle has these principle sources: (1) fluctuations in the number of high energy photons absorbed per unit area of the metal-plate; (2) fluctuations in the energy absorbed per interacting photon; (3) fluctuations in the number of electrons emitted per unit energy absorbed in the metal-plate; (4) spatial fluctuations in the detector absorption associated with inhomogeneities caused by physical or thickness imperfections in the metal-plate and in the film; and (5) fluctuations in the number of silver halide grains per unit area of the emulsion. The first source of radiographic mottle is known as quantum mottle, the second and third sources only make small modifications to the quantum mottle. The fourth source is known as structure mottle, and the fifth source of radiographical mottle is known as film granularity<sup>1,3</sup>. The basic components that contribute most to the total noise are the quantum mottle and the film granularity. The NPS or the Wiener Spectrum can be defined as a representation of the noise variance into spatial frequency components of an otherwise nominally uniform, stationary, ergodic signal<sup>17-18</sup>.

$$W(u, v) = \lim_{x \rightarrow \infty, y \rightarrow \infty} \left[ \left( \frac{1}{4XY} \right) \langle |F(u, v)|^2 \rangle \right] \quad (2.35)$$

where the  $\langle \rangle$  brackets indicate ensemble average and

$$F(u, v) = \int_{-X}^X \int_{-Y}^Y \Delta D(x, y) \exp\{-2\pi i(ux + vy)\} dx dy \quad (2.36)$$

is the Fourier transform of the fluctuations in optical density,  $2X$  is the width of the uniformly scanned area and,  $2Y$  is the length of the scanned area on the portal film. The Wiener spectrum has the dimensions of area and is normalized to the area scanned.

The Wiener-Khintchin theorem<sup>19</sup> describes the sample autocorrelation function and the sample Wiener function (NPS) as Fourier transform pairs (the same holds for the population autocorrelation function and the population NPS):

$$W(u, v) = \int_{-\Delta x}^{+\Delta x} \int_{-\Delta y}^{+\Delta y} c(\Delta x, \Delta y) \exp[-2\pi i(u\Delta x + v\Delta y)] d\Delta x d\Delta y \quad (2.37)$$

$$c(\Delta x, \Delta y) = \int_{-\Delta x}^{+\Delta x} \int_{-\Delta y}^{+\Delta y} W(u, v) \exp[-2\pi i(u\Delta x + v\Delta y)] dudv$$

By setting  $\Delta x = 0, \Delta y = 0$ , the measured variance of the density fluctuations (i.e., scale value) is equal to the volume under the Wiener spectrum

$$c(0, 0) = \int_{-\Delta x}^{+\Delta x} \int_{-\Delta y}^{+\Delta y} W(u, v) dudv = \sigma_A^2 \quad (2.38)$$

In the same manner that the LSF and the MTF are equivalent ways of describing the image spatial resolution, the autocorrelation function and the Wiener spectrum (NPS) are equivalent measures of the image noise for Gaussian processes.

In the spatial frequency domain, Eq. (2.33) becomes:

$$W'(u, v) = W(u, v) \cdot |H(u, v)|^2 \quad (2.39)$$

where  $H(u, v)$  is the optical transfer function of the microdensitometer (or any other scanning device) in question. Although both the Wiener Spectrum and the autocorrelation function give a complete statistical description of the random process, the 'true' Wiener function is simpler to obtain than the 'true' autocorrelation function. The 'true' Wiener

spectrum  $W(u, v)$  is obtained by dividing the measured Wiener spectrum  $W'(u, v)$  by the MTF of the system squared.

#### **2.1.4.4 Error reduction in estimation of Wiener spectra**

In the same way that increasing the number of scanned points will result in a better estimate of the population variance in the spatial domain, one would expect that, given a fixed sampling aperture in the direction of the scan, an increase in the number of sampled points will improve the estimate of the frequency components of the Wiener spectrum (NPS).

Watts and Jenkins<sup>20</sup> estimated the NPS (Wiener spectrum) for the normal, white (i.e., random, gaussian distributed) noise they generated using 100, and 200 scanned points and compared their results to the 'true' horizontal-line spectrum. They arrived at the following conclusions: (1) Increasing the number of points does not improve the estimate of the true spectrum; (2) the standard deviation ( $\sigma$ ) of the spectral estimates is large, in the order of the mean value ( $\mu$ ); and (3) the estimate of the mean is close to the actual value of the mean.

These conclusions can be explained in the following manner. If the sampling interval in the spatial domain remains fixed, then increasing the number of sampled points increases the record length and hence increases the number of spectral components in the spatial frequency domain since the spacing in the Fourier domain  $\Delta u$  decreases with record length. But, each Fourier component retains its variability as an individual point in the same way that each data point sampled in the image has its own variability. Increasing the number of sampled points in the spatial domain does not increase the number of samples of each individual spectral value at a given frequency, but it increases the number of spectral values. Thus, to decrease the variability in the spectral values, many samples of the spectral values at each frequency must be obtained.

One technique that is used to reduce errors in the spectral estimates is to section into  $K$  equal segments the entire length of the film scanned, and to subsequently determine the NPS of each segment separately. Thus each segment's NPS will have an estimate of the same spatial frequency components and the  $K$  estimates for each frequency components will be averaged to obtain the final averaged NPS.

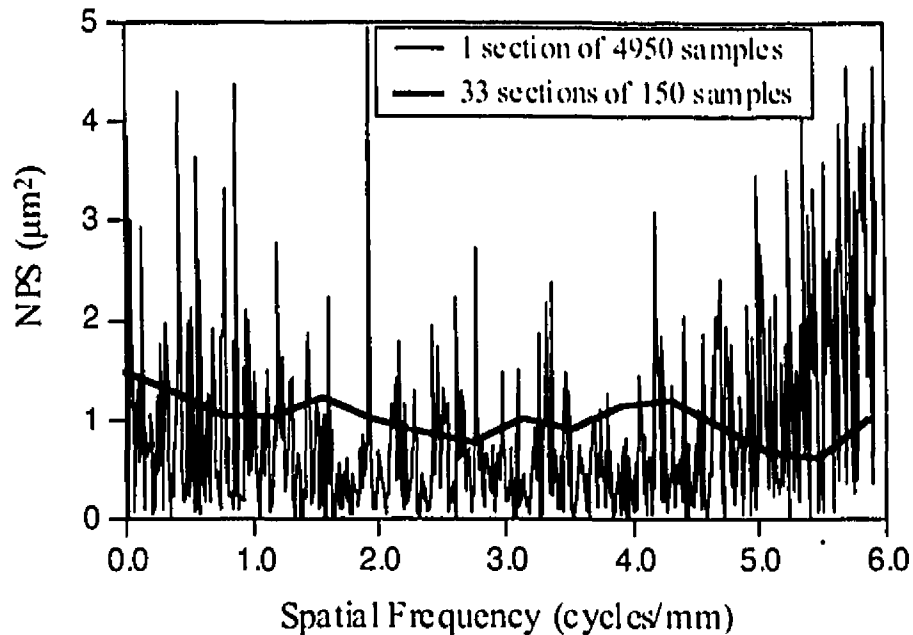


**Figure 2.6** *NPS estimates for 4950 samples of white noise and the average of 33 spectra derived from the 4950 points.*

In Fig. 2.6 we compare the NPS for 4950 scanned points to the spectrum obtained by segmenting the 4950-point trace into 33 segments of 150 points each and averaging the 33 resulting spectra. The scanning interval used is 0.017 mm. The variation of the 4950-point NPS, in units of the mean, is 1.156, yet when we average 33 sections, the variability of the spectral components, in units of the mean, is now reduced to 0.215 which corresponds to approximately  $1 / \sqrt{33-1}$  of the previous value. The mean for the 1 section 4950-point NPS is 0.997, and for the averaged NPS it is 0.999. Although the estimate of the spectral components is improved when the sectioning approach is taken, the spatial frequency resolution  $\Delta u$  has decreased since  $\Delta u$  is inversely related to the record length (0.012 mm<sup>-1</sup> and 0.392 mm<sup>-1</sup> are  $\Delta u$  for the 4950-point NPS and the 150-point NPS, respectively). Thus, when smoothing techniques are applied to spectral data one principle feature emerges: frequency resolution is traded for reduced variation in the spectral values. In the determination of the MTF, the record length chosen is dictated by the length of the tails of the LSF, and only one segment per film length is taken since only one LSF exists per length. In the determination of the NPS, however, there is a need to investigate the effects of the length of the segmented record on the results of the final spectrum values.<sup>17,20-22</sup>

If a length  $R$  of film is sampled, then, from the above discussion<sup>23-25</sup>:

$$\Delta u \cdot \sigma^2 = \frac{1}{R}. \quad (2.40)$$

A fixed amount of information is thus found in a given length  $R$  of sampled film. Precision is exchanged for resolution. Hence, the standard error or uncertainty on the NPS spectral values is given by:

$$S.E. = \left( \frac{1}{R\Delta u} \right)^{\frac{1}{2}}. \quad (2.41)$$

#### 2.1.4.5 Obtaining a 1-d scan from 2-d data

Since our system is isotropic and invariant, a 1-d section of the actual 2-d Wiener spectrum can be totally representative of the information found in the 2-d Wiener spectrum. Thus a measuring method is introduced to provide one section of the 2-d Wiener spectrum without having to evaluate the whole 2-d Wiener spectrum. This permits the determination of the NPS without the need for large memory storage capacities.

Let us assume that the autocorrelation function is measured from a scan in the  $x$ -direction; the autocorrelation function would be solely dependent on the  $\Delta x$  variable since  $\Delta y=0$ . The noise pattern resulting from the therapy machine is isotropic and positionally invariant, thus, the autocorrelation function that is obtained through a 1-d scan will be independent of the actual scan direction (i.e., independent of the value of  $y$ ). Using Eqs. (2.37), and (2.39) and ( $\Delta y = 0$ ), the measured autocorrelation function obtained from the 1-d scan can be written as:

$$c'(\Delta x) = \int_{-\infty}^{+\infty} \left[ \int_{-\infty}^{+\infty} W(u,v) |H(u,v)|^2 dv \right] \exp[-2\pi i(u\Delta x)] du. \quad (2.42)$$

For the 1-d case, the Wiener - Khintchin theorem states that the autocorrelation function and the Wiener function are related as follows:

$$c'(\Delta x) = \int_{-\infty}^{+\infty} [W'(u)] \exp[-2\pi i(u\Delta x)] du. \quad (2.43)$$

Hence, from equations Eqs. (2.42) and (2.43)<sup>26</sup>:

$$W'(u) = \int_{-\infty}^{+\infty} W(u, v) |H(u, v)|^2 dv \quad (2.44)$$

This equation relates the measured  $1-d$  Wiener spectrum of the  $1-d$  scan in the  $x$  - direction with the actual  $2-d$  Wiener spectrum. This is a completely general expression. For an infinitely thin and infinitely long aperture the optical transfer function of the slit is:

$$\begin{aligned} h(x, y) &= \delta(x), \\ H(u, v) &= \delta(v). \end{aligned} \quad (2.45)$$

Using Eqs. (2.44) and (2.45) the measured  $1-d$  spectrum is related to the actual  $2-d$  spectrum in the following manner:

$$W'(u) = W(u, 0). \quad (2.46)$$

Thus, if the noise pattern is scanned by an infinitely thin and infinitely long slit, the  $1-d$  Wiener spectrum is equal to a section of the actual  $2-d$  Wiener spectrum.

Consider the slit transfer function for a more realistic situation of a long, narrow slit with length  $l$  and width  $w$ , in a direction perpendicular to the slit length. The transfer function of the measuring optics is neglected since it is negligible as compared to the scanning slit transfer function.:

$$H(u, v) = \left[ \frac{\sin(\pi w u) \cdot \sin(\pi l v)}{\pi w u \cdot \pi l v} \right] \quad (2.47)$$

and Eq. (2.44) becomes:

$$W'(u) = \text{sinc}^2(uw) \int_{-\infty}^{+\infty} W(u, v) \text{sinc}^2(vl) dv. \quad (2.48)$$

If the slit is sufficiently long that  $W(u, v)$  is constant over the spatial frequency range where the function  $\text{sinc}^2(vl)$  is appreciably non-zero (i.e., tending towards Eq. (2.45)), then

$$W'(u) = \text{sinc}^2(uw) W(u, 0) \int_{-\infty}^{+\infty} \text{sinc}^2(vl) \chi dv. \quad (2.49)$$

The value of the integral is  $1/l$  and the measured  $1-d$  Wiener spectrum is hence equal to:

$$W'(u) = \frac{\text{sinc}^2(uw)}{l} W(u, 0). \quad (2.50)$$

To summarize, if a noise pattern is scanned with a long, narrow aperture then, a representative section of the actual  $2-d$  Wiener spectrum can be readily determined from the  $1-d$  measured Wiener spectrum according to Eq. (2.50). The length  $l$  of the scanning slit used is crucial, and a trial and error method is used to determine the best slit length so as to not obtain erroneous underestimation of the lower frequency components of the Wiener spectrum (discussed in Section 3.2.2.2).

If we chose instead to scan the noise pattern in the  $x$ -direction with a circular aperture of radius  $r$ , then equation (2.44) becomes

$$W'(u) = \int_{-\infty}^{+\infty} W(u, v) \left( \frac{2J_1(2\pi r \sqrt{u^2 + v^2})}{2\pi r \sqrt{u^2 + v^2}} \right)^2 dv, \quad (2.51)$$

where the term in brackets refers to the transfer function of the circular aperture, and  $J_1$  is the first order Bessel function. Since the noise pattern is statistically isotropic the equation above can, in principle, be solved to obtain a  $1-d$  section of the actual  $2-d$  Wiener spectrum from the measured  $W'(u)$ . But this solution is more difficult to obtain. The rectangular slit is more often used since it directly gives a  $1-d$  section of the  $2-d$  Wiener spectrum.<sup>27-30</sup>

#### 2.1.4.6 Callier coefficient

An additional correction factor<sup>18</sup> that must be included in the NPS. This factor involves the actual density or transmission quantity of fluctuations.

Densitometers that illuminate the film with a narrow beam of light and collect transmitted light through  $2\pi$  steradians measure diffuse densities, and densitometers that

collect light from only very narrow beams measure specular density. Specular type densitometers give film optical density readings that are larger than values measured by diffuse density type densitometers since a smaller portion of the output is measured. The Callier coefficient  $Q$ , which is defined as the ratio of the specular to diffuse density, is always greater than 1.00.

The illumination and collection angles in microdensitometers are finite and vary between instruments. Thus, the specular density  $D_I$  of a film sample will be specific to the particular instrument used to measure it. If the density fluctuations,  $\Delta D$ , are measured in terms of the  $D_I$ , then the calculated Wiener spectrum will have a magnitude that is specific to the particular microdensitometer. In comparing Wiener spectra of systems, the spectra should be made independent of the type of microdensitometer used. For this reason, the measure  $\Delta D_I$  are converted to diffuse densities  $\Delta D_D$  by the Callier Coefficient.

The conversion between specular and diffuse density is performed by scanning a multitude of film samples, whose range in densities covers the range of densities desired, using both the microdensitometer in question and a densitometer that measures diffuse density. A typical calibration curve for the microdensitometer used, is shown in Fig. 2.7. In this example, the microdensitometer was calibrated with 14 film samples ranging in optical densities from 0.21 to 3.21 D. A polynomial is then fit to the curve of instrument density versus the corresponding diffuse densities, and the resultant calibration curve is used to convert the measured Wiener spectrum specular densities into diffuse densities.

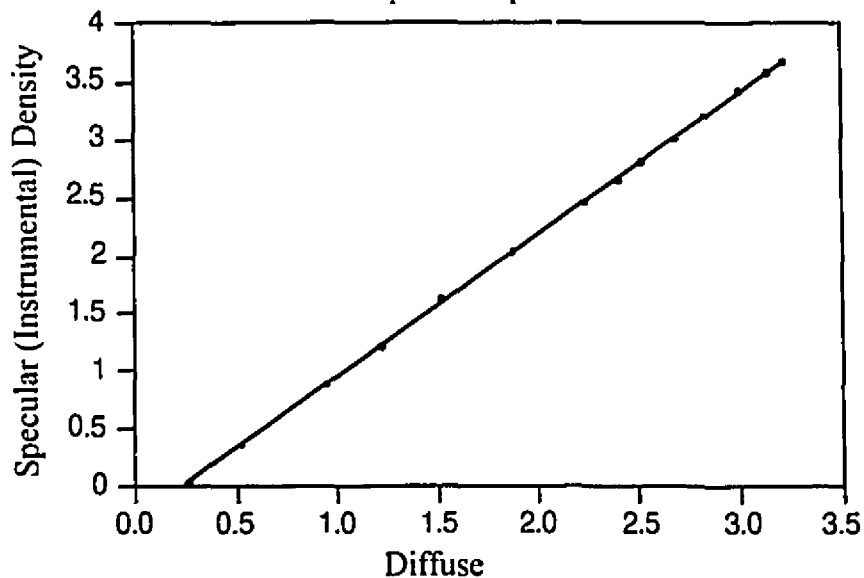


**Figure 2.7** *Microdensitometer calibration curve: Instrumental specular density versus diffuse density.*

The slope of the line in Fig. 2.7 is 1.23, and the calibration curve corresponds to the microdensitometer used for the results in this thesis. The fact that the microdensitometer is set to read net densities is apparent by the offset from zero.

## **2.1.5 Detective Quantum Efficiency (DQE)**

### **2.1.5.1 Introduction**

In 1946, Rose<sup>31</sup> proposed the concept of the Comparative Noise Level (CNL) as a measure of the 'useful' quantum efficiency. It is usually referred to as the detective quantum efficiency (DQE). The ultimate basis of the DQE is the quantum nature of radiation. The lowest noise limit given by the quantum fluctuations in the input information radiation source defines the upper limit of 100% DQE. For the following derivation we are considering the signal and noise transfer characteristics of the system under the assumption that the only source of noise is the fluctuation in the input quantum fluence. The DQE of the metal-plate/film detector can be expressed as a function of the fundamental imaging parameters (film H & D curve, MTF, and NPS) if the system is treated as a detector with a defining operating characteristic which converts fluctuations in exposure to fluctuations in density<sup>32-34</sup>.

### **2.1.5.2 Microscopic view**

The ideal imaging device can be modeled as an array of photon counters, each of which has an area  $a$  and identical response properties (Fig. 2.8). In this case there is a one-to-one relationship between the incident exposure quanta and some measurable output state of the image. Another assumption is that each receptor records the incident quanta independent of its neighbors.

The first stage of the imaging system can be considered as the information source. Since we are using radiation to form the image, the information source in this case is the spatial distribution of the photon intensity entering the detector. The generation of photons at very high energies, due to electron collision with a target, is stochastic in nature resulting in photon counts that can be estimated by Poisson statistics. If the mean number of photons arriving at any ideal detector receptor is  $\bar{n}$ , the standard deviation is  $\sqrt{\bar{n}}$ . The ideal image is one that has noise contribution from only the quantum fluctuations at the information source. For imaging modalities that use very low counting to generate their image such as

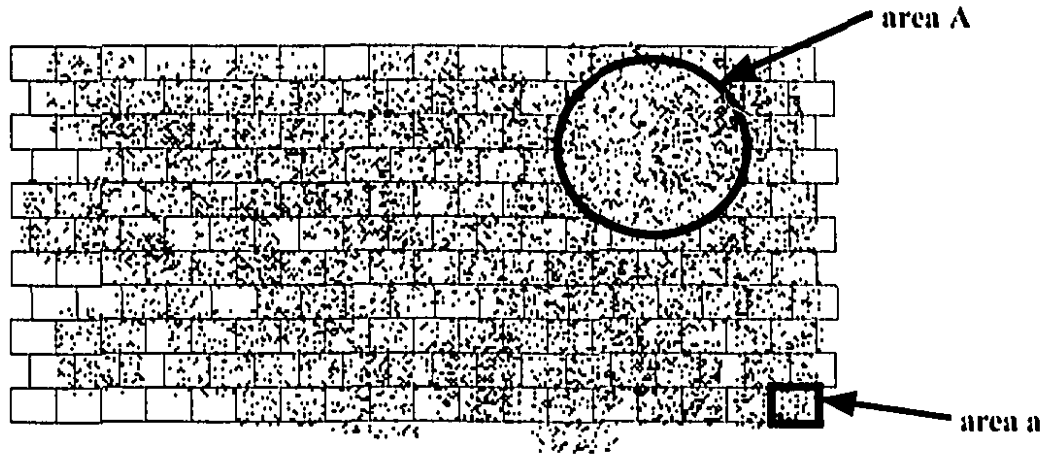


**Figure 2.8** Ideal array of detectors each of area  $a$  and the number of photon counts impinging onto it.  $A$  is the scanning aperture size.

the gamma camera, lesions in the image can be obscured by the quantum noise. To ensure that the detectability of the real signal is not mistaken by the random fluctuations of the background photon density, the magnitude of the real signal must differ considerably from the mean value of the background. Real imaging systems contribute noise other than quantum mottle to the signal detected (see Section 2.1.4.3).<sup>35</sup>

For practical imaging systems, a macroscopic approach is taken in describing the input and output relation because a very large number of photons and radiographically exposed grains are involved.

### 2.1.5.3 Macroscopic view

A measure of the level of photon counts received can be gauged by the degree of 'blackness' or opacity  $O$  of the individual receptors. The opacity of the receptor is defined as the ratio of incident  $I_o$  to transmitted  $I_T$  intensity. A more practical measure of film darkness is optical density  $D$ , which is the logarithm of opacity.

$$D = \log_{10} O, \text{ where } O = I_o/I_T \quad (2.52)$$

We can also measure the density of a large number of receptors rather than just each individual receptor area  $a$  by using a measuring aperture of area  $A$  (Fig. 2.8):

$$A = Na \quad (2.53)$$

where  $N$  is the number of receptors covered by the aperture. Assuming that the amount of light that is subtracted from the incident beam during illumination is proportional to the average quantum exposure count level  $q$ , then we can write<sup>14</sup>

$$D \propto \log_{10} q. \quad (2.54)$$

The constant of proportionality which is also the slope of the sensitivity curve  $\gamma$  that relates the fluctuation in exposure to fluctuation in measured density is given by

$$\gamma = \frac{dD}{d(\log_{10} q)} \quad (2.55)$$

and since  $d(\log_{10} q) = \log_{10} e(dq/q)$ , then Eq. (2.55) becomes

$$\gamma = \left( \frac{q}{\log_{10} e} \right) \left( \frac{dD}{dq} \right). \quad (2.56)$$

The real detector will be compared to the ideal case, using the Comparative Noise Level (CNL) analysis developed by Rose<sup>31</sup>. The CNL is given as the ratio of the input signal fluctuations to the output signal fluctuations. Thus an ideal detector would have a CNL of one whereas any real detector has a value of CNL less than one. The CNL is determined in the following manner. The mean square fluctuation in film density is denoted by  $\sigma_A^2$  measured with a scanning aperture of area  $A$ . This is the output density fluctuations, and using Eq. (2.56) we can define the equivalent *output exposure fluctuations* as:

$$\text{output exposure fluctuations} = \sigma_A^2 \left( \frac{dq}{dD} \right)^2 = \sigma_A^2 \left( \frac{q_A}{\gamma \log_{10} e} \right)^2 \quad (2.57)$$

where  $q_A$  denotes the average number of exposure quanta per image area  $A$ . The *input exposure fluctuations* is given by  $\overline{\Delta q_A^2} = q_A$ . Thus, this will lead to a comparative noise level or detective quantum efficiency (DQE) of:

$$\begin{aligned}
 CNL = DQE &= \frac{\text{exposure fluctuations in input}}{\text{exposure fluctuations in output}} \\
 &= \frac{q_A}{\sigma_A^2 \left( \frac{q_A}{\gamma \log_{10} e} \right)^2} = \frac{\gamma^2 (\log_{10} e)^2}{\sigma_A^2 q_A}. \quad (2.58)
 \end{aligned}$$

At this point it may be beneficial to look more closely at the characteristics of the mean-square noise fluctuations over the sampling aperture  $A$ . It is shown in Fig. 2.5 that the aperture size affects the density fluctuations that are measured. It can be shown that although the density fluctuations during image scanning are dependent on the size of the scanning aperture  $A$ , the product  $A\sigma_A^2$  is independent of the size of the measuring aperture, and is defined as the noise parameter  $G$ .<sup>36-37</sup>

$$G = A\sigma_A^2 \quad (2.59)$$

Next we define the average fluence, denoted by  $\bar{q}$ , using Eq. (2.53)

$$q_A = Nq = \frac{A}{a}q = A\bar{q} \quad (2.60)$$

where  $q$  is the average number of exposure quanta impinging on the receptors of area  $a$ . Using Eqs. (2.58), (2.59) and (2.60) we redefine DQE in terms of  $G$ :

$$DQE = \frac{\gamma^2 (\log_{10} e)^2}{\sigma_A^2 A\bar{q}} = \frac{\gamma^2 (\log_{10} e)^2}{\bar{q}G}. \quad (2.61)$$

Equation (2.61) gives an expression for the DQE which is independent of the aperture that is used to measure the optical density fluctuations from the radiographic film.

The DQE should also be expressed in terms of the spatial frequency domain. To accomplish this the noise parameter  $G$  is to be expressed in terms of the Wiener spectrum. The noise parameter is related to the Wiener spectrum through the relation<sup>26,38</sup>

$$G = W(0) \quad (2.62)$$

for an isotropic noise pattern, and for the case where the product of the Wiener spectrum and the transfer function of the microdensitometer optical system is constant over the spatial frequency range defined by the dimensions of the scanning aperture. But in general, since the Wiener spectra for most film noise patterns and the transfer function of microdensitometer optical systems decrease with increased spatial frequencies, the following must be quoted<sup>26</sup>

$$G \leq W(0). \quad (2.63)$$

From Eqs. (2.57), (2.59),(2.60), and (2.62) the output noise ( $\sigma_{out}$ ), which is obtained from the mean-square fluctuations in density over an area of the image  $A$ , can be written in terms of  $W(0,0)$  in the following manner

$$\sigma_{out}^2 = \sigma_A^2 \left( \frac{dq}{dD} \right)^2 = GA \left( \frac{\bar{q}}{\gamma \log_{10} e} \right)^2 \rightarrow \sigma_{out}^2(0,0) = W(0,0)A \left( \frac{\bar{q}}{\gamma \log_{10} e} \right)^2. \quad (2.64)$$

The inequality in Eq. (2.63) will be accounted for in Eq. (2.64) by considering the dependence of the output fluctuations  $\sigma_{out}$  on spatial frequency through the dependence of the macro characteristic curve on spatial frequencies. It can be shown<sup>17,39</sup> that the slope of the characteristic curve is a function of the MTF of the detector:

$$\gamma(u,v) = \gamma(0,0)MTF(u,v). \quad (2.65)$$

This product is known as the Contrast Transfer Function (CTF). With Eq. (2.65), the expression for the output fluctuations of Eq. (2.64) becomes:

$$\sigma_{out}^2(u,v) = W(u,v)A \left( \frac{\bar{q}}{\gamma MTF(u,v) \log_{10} e} \right)^2 \quad (2.66)$$

where for simplification  $\gamma = \gamma(0,0)$ .

Since the input quantum fluence follows Poisson statistics (a random distribution), from Eq. (2.58) the input fluctuations can be given by  $\sigma_{in}^2(u,v) = q_A = \bar{q}A$ . Therefore, the DQE is given by

$$DQE(u, v) = \frac{\sigma_{in}^2}{\sigma_{out}^2} = \left( \frac{[\gamma(\log_{10} e) MTF(u, v)]^2}{\bar{q} W(u, v)} \right) \quad (2.67)$$

and for the case of an isotropic imaging process:

$$DQE(u) = \left( \frac{[\gamma(\log_{10} e) MTF(u)]^2}{\bar{q} W(u)} \right). \quad (2.68)$$

The  $\gamma$  must correspond to the value of the slope for the film mean optical density at which the Wiener spectrum is determined, and there is no dependence on the aperture size that is used to measure the Wiener spectrum.

### 2.1.6 Signal-to-Noise Ratio

In quantifying the efficiency of a radiation detector, one of the most important criterion used is the signal-to-noise ratio ( $S/N$ ). Thus we will now calculate the DQE in terms of this ratio.

When the input noise is only due to the quantum fluctuations (modeled by Poisson statistics) of the input exposure quanta, then the input ( $S/N$ ) ratio for  $q_A$  average input exposure quanta is given by

$$\left( \frac{S}{N} \right)_{in} = \frac{q_A}{\sqrt{q_A}} = \sqrt{q_A} \rightarrow \left( \frac{S}{N} \right)_{in}^2 = q_A. \quad (2.69)$$

The output ( $S/N$ ) ratio is defined by the average number of input exposure quanta divided by the output noise measured from the optical density on the film and referred back in terms of the exposure. Using equation (2.57) we obtain

$$\left( \frac{S}{N} \right)_{out} = \frac{q_A}{\sigma_A \left( \frac{dq}{dD} \right)} = \frac{\gamma(\log_{10} e)}{\sigma_A}. \quad (2.70)$$

The square of the ratio  $(S/N)_{out}$  to  $(S/N)_{in}$  is exactly equal to the DQE (see Eq. (2.61)):

$$\frac{(S/N)_{out}^2}{(S/N)_{in}^2} = \frac{1}{q_A} \left( \frac{\gamma(\log_{10} e)}{\sigma_A} \right)^2 = DQE. \quad (2.71)$$

This equation seems intuitively correct since  $(S/N)_{out}$  will always be less than or equal to  $(S/N)_{in}$  which implies that the ratio in the above equation is always less than 100 % except for the case of an ideal detector where the ratio is 100 %. A schematic representation of the  $(S/N)$  ratios and DQE for the photographic process is shown in Fig. 2.9, where the DQE acts as the transfer function of the system.

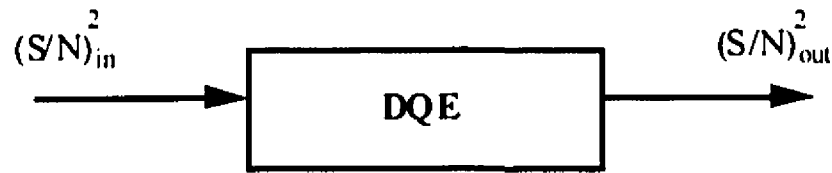


Figure 2.9 The  $(S/N)$  transfer system.

### 2.1.7 Noise-Equivalent Number of Quanta

The efficiency of a detector can also be interpreted in terms of the *equivalent* number of quanta absorbed by the detector. In this way, an ideal detector is one that collects all of the photons impinging on it while a practical detector can be considered to be a detector that detects a lesser number of counts than those that are available to it (i.e., an inefficient photon counter).

Using Eqs. (2.61) and (2.71) we can define the lesser number of counts  $\bar{q}'$  detected by a real detector as

$$\frac{(S/N)_{out}^2}{(S/N)_{in}^2} = \left( \frac{\frac{(\gamma \log_{10} e)^2}{G}}{\bar{q}} \right) = \left( \frac{\bar{q}'}{\bar{q}} \right) = \frac{NEQ}{\bar{q}} \quad (2.72)$$

where the upper limit of the number of quanta detected is equal to the average fluence from the information source  $\bar{q}$ .  $\bar{q}'$  is usually interpreted as the noise-equivalent number of quanta (NEQ). Since  $G$  is independent of the aperture used to measure it, the NEQ per unit image area is also independent of the aperture used to measure it.

## 2.2 Effects of Digitization

### 2.2.1 Introduction

The LSF image and the uniformly irradiated film are scanned using a microdensitometer and this sampled data is then processed through a Fast Fourier Transform (FFT) algorithm to determine the MTF and the Wiener spectrum, respectively. The sampling rate and the number of samples obtained (i.e., length of the sampled data set) are important in determining to what extent the digital data is faithful to the information found in the analog medium. Two types of artifacts must be avoided when digitizing data: *truncation artifacts*, when the length of the sampled LSF data set is too short, and *aliasing artifacts* which occur whenever an incorrect sampling rate is used for the extent of the spatial frequencies that we desire to study.

### 2.2.2 Truncation Artifacts

Although the tail portions of LSFs consist of small intensities in the spatial domain, they may nevertheless contain significant spatial frequency information. The truncation effect is similar to a windowing effect whereby a finite-length, digitized LSF is equivalent to the 'true' LSF multiplied with a 1-d rectangular function. In the spatial frequency domain this results in the 'true' MTF, that would correspond to the 'true' LSF, being convolved with a *sinc* function characterized by the length of the sampled data set. This fact is evident from the mathematical point of view, where  $\mathfrak{F}$  denotes the Fourier operator.

$$\begin{aligned} LSF_{trunc}(x) &= LSF(x) \cdot rect(x), \\ \mathfrak{F}[LSF_{trunc}(x)] &= \mathfrak{F}[LSF(x)] \otimes \mathfrak{F}[rect(x)] \\ MTF_{trunc}(u) &= MTF(u) \otimes sinc(u) \end{aligned} \tag{2.73}$$

Truncation artifacts<sup>4,18</sup> can be avoided by sampling the correct length of the LSF images. This implies that any background noise from scattered photons must be estimated to determine what is actually part of the tail information on the film. Techniques used to estimate the background will be discussed in chapter 3.

### 2.2.3 Aliasing artifacts: Finite Sampling Interval and Finite Sampling aperture effects

Sampling a function at some rate in the spatial domain can be described by multiplying the function with the  $comb(x/\Delta x)$  function. The  $comb(x/\Delta x)$  consists of a series of equi-distant *delta* functions with sampling separation  $\Delta x$ . Figure 2.10 shows this schematically.

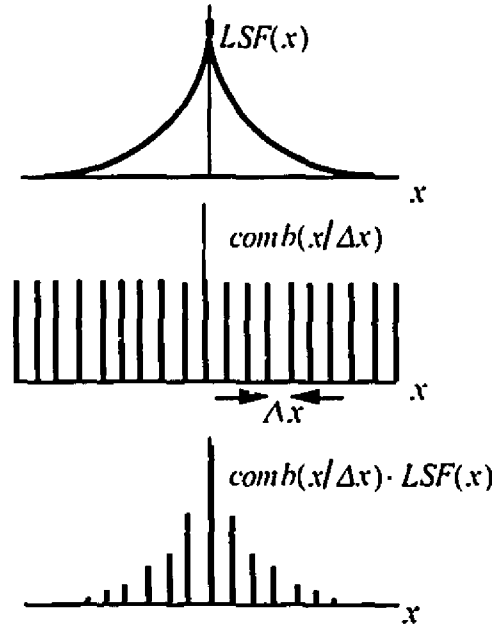


Figure 2.10 LSF being sampled at intervals of  $\Delta x$ .

The Fourier transform of the sampled LSF can be described mathematically:

$$\begin{aligned}
 LSF_{sampled}(x) &= LSF(x) \cdot comb(x/\Delta x), \\
 \mathfrak{F}[LSF_{sampled}(x)] &= \mathfrak{F}[LSF(x)] \otimes \mathfrak{F}[comb(x/\Delta x)] \\
 MTF_{result}(u) &= MTF(u) \otimes comb(\Delta x \cdot u)
 \end{aligned}
 \tag{2.74}$$

The Fourier transform of the *comb* function is another *comb* function but with the spacing given by  $1/\Delta x$ . Since the *comb* function is made up of periodic *delta* functions the convolution represented in the last line of Eq. (2.74) results in exact copies of the MTFs in the spatial frequency domain at spacings of  $1/\Delta x$ . Assuming that the MTF of the LSF image is a bound function with its spatial frequency domain falling within a specified range where the maximum spatial frequency component of the function is  $f_n$ , then, Fig. 2.11

shows the effects for different sampling rates in the spatial domain. Aliasing occurs when the function in the spatial domain is sampled at intervals less than  $1/(2f_n)$  because, as is shown in Fig. 2.11, the Fourier transform of the function overlaps with itself in the spatial frequency domain<sup>4</sup>. In this case, frequencies greater than  $f_n$  are masked or are being treated as lower frequency contributions. The Nyquist criterion states that the largest spatial frequency of any function, sampled at rate  $\Delta x$ , whose spectral value is equal to that of the analog counterpart is  $u = 1/(2\Delta x)$ . This limiting frequency  $u$  is known as the folding or Nyquist frequency.

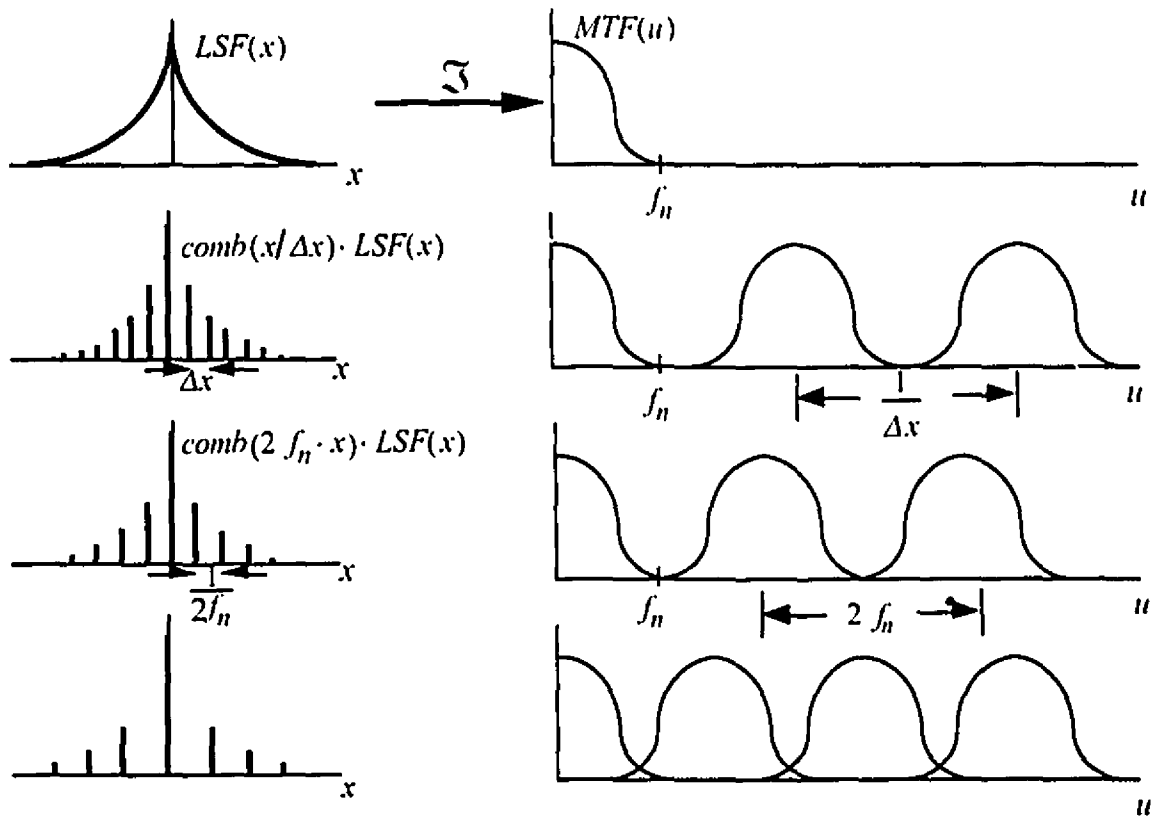


**Figure 2.11** Effect on the spacings between repeated MTFs if the sample spacing of the sampled image is increased<sup>4</sup>.

Since the analog data is being scanned with a finite-sized aperture, we are dealing with bound functions. The sampling *comb* function in Fig. 2.11 should actually be convolved with the size of the sampling aperture (a *rect* function). This gives rise to a repetition of bounded functions as is alluded to in Fig. 2.11, multiplied by the aperture *sinc* function, at each repetition. Mathematically we have:

$$\begin{aligned}
 LSF_{\text{sampled}}(x) &= LSF(x) \otimes \text{rect}(x) \cdot \text{comb}(x), \\
 \mathfrak{N}[LSF_{\text{sampled}}(x)] &= \mathfrak{N}[LSF(x)] \cdot \mathfrak{N}[\text{rect}(x)] \otimes \mathfrak{N}[\text{comb}(x)], \\
 MTF_{\text{result}}(u) &= MTF(u) \cdot \text{sinc}(u) \otimes \text{comb}(u).
 \end{aligned}
 \tag{2.75}$$

Thus, each MTF is multiplied at intervals of  $1/\Delta x$  with the microdensitometer scanning aperture *sinc* function. The MTF data will be destroyed if the bounding effects of the aperture are not taken into consideration. In Fig 2.12, we show the extent of the first lobe for *sinc* functions corresponding to several aperture widths ranging from 1  $\mu\text{m}$  to 1 mm.

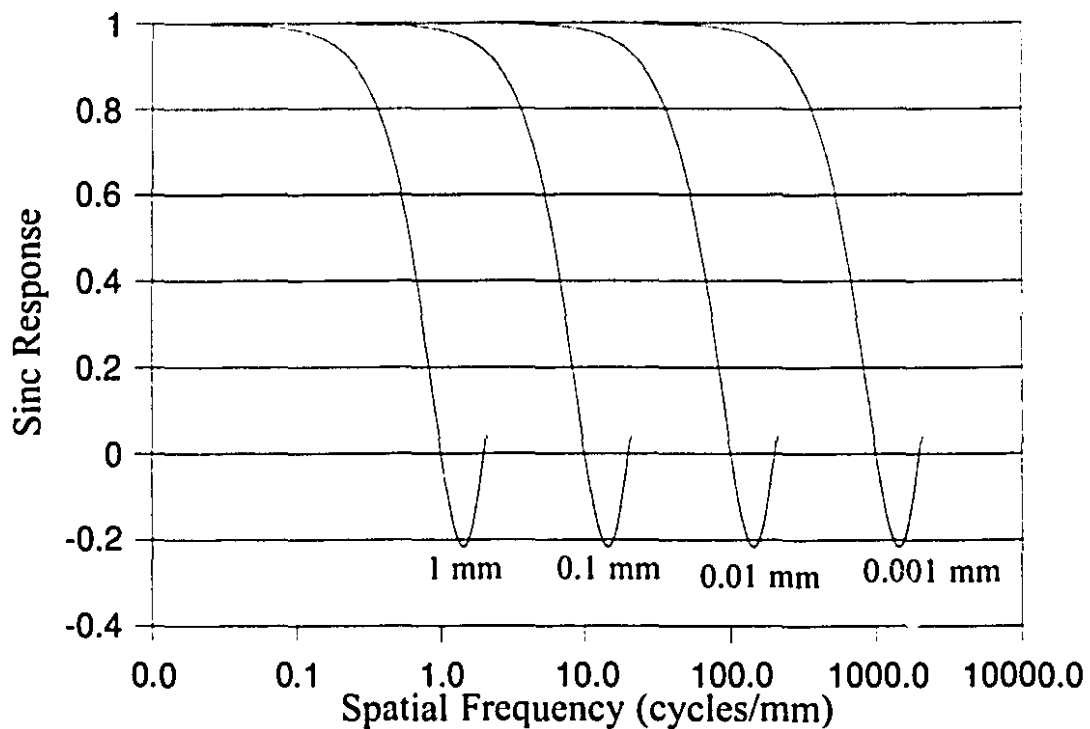


**Figure 2.12** *Sinc functions corresponding to several rectangular aperture scanning widths: (from left to right) 1 mm; 100  $\mu\text{m}$ ; 10  $\mu\text{m}$ ; and 1  $\mu\text{m}$ .*

Several steps have to be considered to determine the correct sampling rate so as to prevent aliasing. (1) The maximum spatial frequency up to which we want to determine accurately the MTF and Wiener spectra, must be chosen. For our purpose 10 cycles/mm is adequate. (2) If we allow no more than a 2 % systematic error on the value of the MTF then we have to choose the *sinc* function that corresponds to an aperture of size no more than 10  $\mu\text{m}$ , as is indicated in the figure above<sup>40</sup>. If a 1 mm scanning aperture is chosen, then the corresponding lobe of the *sinc* function would destroy most of the information

beyond 0.5 cycles/mm. Likewise, a 100  $\mu\text{m}$  aperture would introduce an approximately 10 % systematic error in the measurement of the MTF for frequencies at 5 cycles/mm. The bound function corresponds to the function that is found in the region of the first lobe of the *sinc* function for that aperture size. The sampling interval  $\Delta x$  has to be such that there is no overlap of the first lobe of the *sinc* function due to replication. The first zero of the *sinc* function for the 10  $\mu\text{m}$  aperture is at 100 cycles/mm. (3) Using the Nyquist rule to avoid overlap of the functions up to 100 cycles/mm, we require sampling at 5  $\mu\text{m}$  intervals. However, since we are concerned only with the first 10 cycles/mm and not the whole 100 cycles/mm range, the 5  $\mu\text{m}$  scanning interval required can be relaxed. The extent of the first *sinc* lobe is 200 cycles/mm. Thus, if the MTFs are repeated at every 110 cycles/mm, as opposed to 200 cycles/mm, then, the adjacent *sinc* lobes would fall to zero at 10 cycles/mm, not affecting the MTF between 0 and 10 cycles/mm. With a 10  $\mu\text{m}$  aperture, a repetition of the MTFs at every 110 cycles/mm can be generated by sampling at intervals of 9  $\mu\text{m}$ . Using a 9  $\mu\text{m}$  instead of a 5  $\mu\text{m}$  sampling interval would decrease to almost half the storage memory required and the time of acquisition. The resulting MTF is then divided by the *sinc* function of the finite sampling aperture to reduce the systematic error it caused.

The secondary lobes associated with the aperture *sinc* function affect to a lesser degree the results found in the primary lobe of the adjacent function. The amplitude of the first sidelobe of the *sinc* is  $(1/3\pi)$  with respect to the zero frequency term. The digitization specifications in this thesis are summarized in Table 2.1:

**Table 2.1** Digitization specifications.

Maximum spatial frequency considered	10 cycles / mm
Maximum scanning aperture width required for a maximum 2 % systematic error on the spectral values	10 $\mu\text{m}$
Extent of the first lobe of the <i>sinc</i> function corresponding to this aperture width	$\frac{1}{10 \mu\text{m}} = 100 \text{ cycles / mm}$
The sampling interval $\Delta x$ required according to the Nyquist criterion	$\frac{1}{2 \cdot 100 \text{ cycles / mm}} = 5 \mu\text{m}$

## References:

- <sup>1</sup> Curry, T.S., Dowdey, J.E., and Murrey, R.C., Jr., *Christensen's Physics of Diagnostic Radiology, fourth edition*, Lea & Febiger, 196-218, (1990).
- <sup>2</sup> Rose, A., *Vision-Human and electronic*, Plenum, New York, (1974).
- <sup>3</sup> Webb, S., editor, *The Physics of Medical Imaging*, Medical Science Series, Adam Hilger, Bristol and Philadelphia, PA, USA, Chapter 3, (1988).
- <sup>4</sup> Bracewell R.N., *The Fourier Transform and Its Applications, second edition*, McGraw-Hill Book Company, chapters 1 to 6, (1978).
- <sup>5</sup> Cooley, J. W., Lewis, P. A. W., and Welch, P. D., *The Fast Fourier transform algorithm and its applications*, IBM, Yorktown Heights, New York, Res. Paper RC-1743, (1967).
- <sup>6</sup> Dainty, J. C., and Shaw, R., *Image Science*, Academic Press, London, New York, chapters 6 and 7, (1974).
- <sup>7</sup> Champeney, D.C., *Fourier Transforms and their Physical Applications*, Academic Press, chapters 1-5, (1973).
- <sup>8</sup> Papoulis, A., *Systems and Transforms with Applications in Optics*, McGraw-Hill Series in Systems Science, chapters 2 and 3, (1968).
- <sup>9</sup> Wiener, N., "Generalized harmonic analysis," *Acta Math*, 55, 117, (1930).
- <sup>10</sup> Fellgett, P.B., "Concerning photographic grain, signal-to-noise ratio, and information," *J. Opt. Soc. Amer.*, 43, 271, (1953).
- <sup>11</sup> Jones, R.C., "New method of describing and measuring the granularity of photographic materials," *J. Opt. Soc. Amer.*, 45, 799, (1955).
- <sup>12</sup> Zwiieg, H. J., "Autocorrelation and granularity. Part I. Theory," *J. Opt. Soc. Am.*, 46, 805 - 811, (1956).
- <sup>13</sup> Selwyn, E.W.H., "A theory of graininess," *Photographic J.*, 75, 571, (1935).
- <sup>14</sup> Nutting, P.G., "On the absorption of light in heterogeneous media," *Phil. Mag.*, 26, 423, (1913).
- <sup>15</sup> Schwarz, R. J., and Friedland, B., *Linear Systems*, McGraw-Hill Book Company, New York, New York, chapter 9, (1965)
- <sup>16</sup> I bid reference 6., chapter 8.
- <sup>17</sup> I bid reference 6., chapters 6, 7 and 8.

- 18 Doi, K., Holje, G., Loo, N., Chan, H., Sandrik, J.M., Jennings, R.J., and Wagner, R.F., "MTF's and Wiener Spectra of radiographic screen-film systems," HHS Publication, No. 82-8187 (FDA), (1982).
- 19 O'Neill, E.L., *Introduction to Statistical Optics*, Addison-Wesley, Reading, MA, page 18, (1963).
- 20 Jenkins, G. M., and Watts, D. G., *Spectral Analysis and its applications*, Holden-Day, San Francisco, (1968).
- 21 Blackman, R. B., and Tukey, J. W., *The measurement of Power Spectra*, Dover, New York, (1958).
- 22 Brigham, E. O., *The Fast Fourier Transform*, Englewood Cliffs, N.J., Prentice-Hall, Chapter 13, (1974).
- 23 Wagner, R. F., and Sandrik, J. M., "An introduction to digital noise analysis," In: *The physics of Medical Imaging: Recording System Measurements and Techniques*, A.G. Haus, Ed., American Institute of Physics, New York, 524-545, (1979).
- 24 Doi, K., "Wiener spectrum analysis of quantum statistical fluctuations and other noise sources in radiography," In: *Television in Diagnostic Radiology*, Moseley, R. D., and Rust, J. H., Eds., Aesculapius Publishing Co., 313-333, (1969).
- 25 I bid reference 6., Figure 8.13.
- 26 Jones, R.C., "New methods of describing and measuring the granularity of photographic materials," *J. Opt. Soc. Amer.*, 43, 271, (1955).
- 27 Trabka, E. A., "Wiener spectrum scans obtained from an isotropic two - dimensional random field," *J. Opt. Soc. Amer.*, 55, 203, (1965).
- 28 Wagner, R. F., and Weaver, K. E., "Noise measurements on rare-earth intensifying screen systems," In: *Medical X-ray Photo-Optical Systems Evaluation*, Proc. SPIE, 56, Palos Verdes Estates, CA, pp. 198 - 207, (1975).
- 29 Sandrik, J. M., and Wagner, R. F., "Radiographic screen-film noise power spectrum: Variation with microdensitometer slit length," *Applied Optics*, 20(16), 2795-2798, (1981).
- 30 De Belder, M., De Kerf, J., "The determination of the Wiener spectrum of photographic emulsion layers with digital methods," *Photo. Sci. Eng.*, 11, 371-378, (1970).
- 31 Rose, A., "A unified approach to the performance of photographic film, television pick-up tubes, and the human eye," *J. Soc. Motion Picture Engrs.*, 47, 273, (1946).
- 32 Rossman, K., "Spatial fluctuations of x-ray quanta and the recording of radiographic mottle," *Am. J. Roentgenol*, 90, 863 - 869, (1963).

- 33 Cleare, H. M., Splettstosser, H. R., Seeman, H. F., "An experimental study of the mottle produced by x-ray intensifying screens," *Am. J. Roentgenol*, 88, 168-174, (1962).
- 34 I bid reference 6., chapter 5.
- 35 Papoulis, A., *Probability, Random Variables and Stochastic Processes*, McGraw-Hill, New York, (1965).
- 36 Selwyn, E.W.H., "A theory of graininess," *Photogr. J.*, 75, 571, (1935).
- 37 Shaw, R., "Image evaluation as an aid to photographic emulsion design," *Photogr. Sci. Eng.*, 16, 395, (1972).
- 38 Shaw, R., "The equivalent quantum efficiency of the photographic process," *The Journal of Photographic Science*, 11, 199-204, (1963).
- 39 Shaw, R., "Evaluating the efficiency of imaging processes," *Report on the Progress of Physics*, 41, 1103-1155, (1978).
- 40 Villafana, T., "Modulation transfer function of a finite scanning microdensitometer slit," *Medical Physics*, 2(5), 251-254, (1975).

# MATERIALS AND METHODS

## 3.1 Measuring the Modulation Transfer Function

### 3.1.1 Introduction

The detectors' absolute performance is given by the DQE which is defined by Eq. (2.68) as:

$$DQE(u) = \left( \frac{[\gamma(\log_{10} e) MTF(u)]^2}{\bar{q} \cdot NPS(u)} \right)$$

where  $NPS(u)$  is the total Noise Power Spectrum (replacing symbol  $W(u)$  in Eq. (2.68)) of the detector whose film was irradiated to a nominal optical density of 1.00,  $\gamma$  is the point gradient of the film characteristic curve at that same optical density,  $MTF(u)$  is the Modulation Transfer Function of the detector, and  $\bar{q}$  is the average fluence per unit area that impinges onto the detector when irradiating the film to optical density one.

Experimental techniques are used to obtain the LSF which is subsequently processed to obtain the  $MTF^{1-11}$ . Certain experimental and processing techniques will be

discussed in detail here. There are basically three experimental techniques that can be used to determine the LSF: the wire, edge or slit techniques<sup>6</sup>.

The wire method uses a radiopaque wire between the radiation source and the detector. In this case, the beam is barely attenuated and the signal that is obtained at the detector is greatly affected by the scatter that is present in the room. Thus, the wire method *SNR* can never be greater than that of the edge or slit methods. For practical reasons the wire method is never used because the contrast of the LSF at high energies would be non-existent.

The edge method<sup>12-13</sup> consists of placing a radiopaque block in the X-ray beam so that the center of the X-ray beam coincides with the edge of the block (i.e., only half of the X-ray beam is covered by the block). In this case, an Edge Spread Function (ESF) is obtained which must be differentiated to obtain the LSF and which is subsequently Fourier transformed to obtain the MTF. Scatter is again a problem since half of the detector area detects scattered photons not attenuated by the blocks.

The slit method can be seen as the complement of the wire method in that it involves imaging an X-ray beam passing through a narrow slit formed by two adjacent radiopaque blocks. The portion of the X-ray beam that is collimated through the slit is used to approximate a line in the object plane. The X-ray beam field size is made equal to or smaller than the field of the radiopaque blocks to reduce the amount of scattered photons generated in the therapy room. These scattered photons would otherwise be detected as a background noise contribution to the image of the LSF, and would decrease the image contrast. Munro *et al.*<sup>4</sup> compare LSFs obtained with the slit method under conditions of maximum scatter behind the blocks (large field size, blocks close to wall), or minimum scatter behind the blocks (field size smaller than the area of the blocks). Even though the correct set up is used there will still be some minimal background noise due to scatter that is added to the slit image, but, the overwhelming contribution to the background noise level will come from the film granularity. Several processing techniques will be discussed in the next section to deal with the removal of this background noise. Background noise accounts for the largest portion of the systematic error in estimating the MTF. For this reason, the thickest possible blocks that can be manufactured are used to maximize attenuation of the beam outside the slit and obtain the largest LSF contrast.

The slit method, in addition to generating lower background noise due to decreased scatter, is also simpler to implement when aligning the slit with the center of the X-ray beam<sup>1</sup>. The criterion for perfect alignment of the slit with the center of the radiation beam<sup>2-5</sup> is achieved when the ratio of the film intensity of the center of the slit image to that at the LSF tail (background) is greatest. Cunningham *et al.*<sup>6</sup> simulated results for all three methods and found that the edge technique is superior for measuring low-frequency response but that the slit technique is best for measuring high-frequency response. Because of high scatter and alignment difficulties in therapy imaging, the slit method is used almost exclusively.

Figure 3.1 shows a schematic of the steps that were taken to obtain the estimate of the MTF for each detector. A detector consists of a double-emulsion portal film (RP Kodak localization) sandwiched between some combination of front and back metal-plates. Boxes with single outline correspond to the experimental techniques section (3.1.2), whereas, boxes with double outlined are discussed in the processing techniques section (3.1.3). The section numbers in each box correspond to the section in which the contents of the box is discussed.

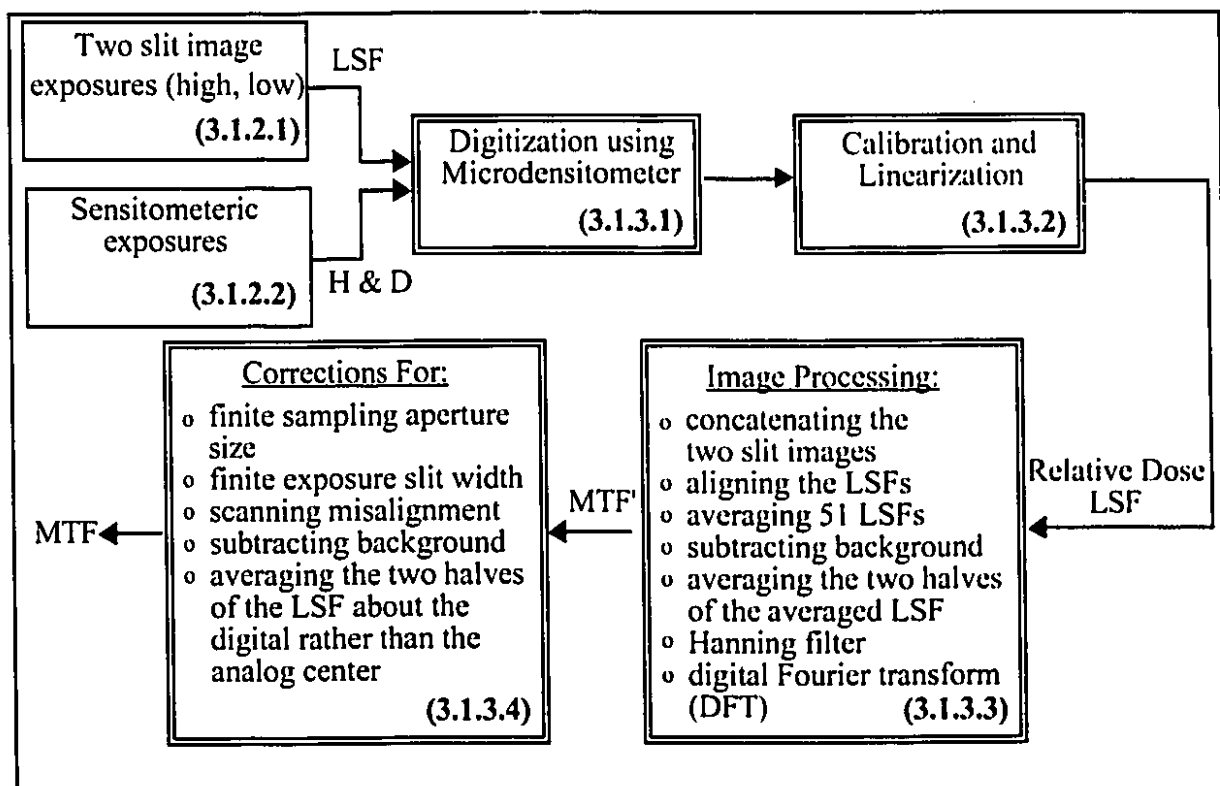


**Figure 3.1** Block diagram for the experimental and processing techniques used to determine the MTF of the metal-plate/film detectors.

### 3.1.2 Experimental techniques

The experimental procedures<sup>2-5</sup> used to determine the LSF image are discussed in the following section.

#### 3.1.2.1 Obtaining LSF images

The slit is formed from two stainless steel blocks each with dimensions 76.2 x 76.2 x 160.0 mm<sup>3</sup> and density 7.54 g/cm<sup>3</sup>. The thickness of the blocks is 160.0 mm (attenuating a 1 MeV photon beam to approximately 0.05 % of its incident flux) and the maximum length of the slit was 76.2 mm. The blocks were cut, ground, and milled to a tolerance of 4 - 7 μm, in terms of parallelness of the opposing sides.

The nominal slit width formed is 25 μm. This slit width is obtained by placing two steel shims of 25 μm thicknesses between the adjacent steel blocks that are subsequently clamped together. The steel shims are placed on the top and bottom portion of the blocks. The steel shims have approximate dimensions of 25 μm x 70.0 mm x 10.0 mm. When digitizing the LSF from the film, the top 15.0 mm and the bottom 15.0 mm of the LSF image is not scanned since this portion of the LSF is corrupted by the images of the shim spacers.

In the diagnostic case, the LSF is obtained with slit widths of the order of 5 - 10 μm<sup>13</sup>. These small slits can be used at these energies since a high contrast exists between the center of the LSF and the tails, due to the inherent high subject contrast at these energies and low scatter contribution. But, at higher energies the need for the smallest slit width is exceeded by the need for high contrast. A slit of size 5 μm at high energies would result in the destruction of the LSF peak due to the high scatter<sup>2</sup>. The field of view from the source to the detector is also increased with a large slit so that it is less likely to lose contrast in the LSF due to misalignment. Furthermore, because of the penetrating nature of the high energy photons compared to that of the diagnostic photons, the effective slit width is less sensitive to misalignment<sup>2-3</sup>.

The clamped blocks are then fastened to an X-Y platform (Aerotech, Inc., Pittsburgh, PA) which is a servo-motor operated unit, whose motion is controlled by two-axis microprocessor-based motion controller (Model Unidex 11, U11s). The platform motion can be specifiable to 2 μm. Initially, the slit formed by the blocks is approximately aligned with the center of the X-ray beam through the use of the wall lasers. The gantry is

moved in a horizontal position to irradiate the blocks and detectors. The XY-stage is moved so that the motion of the blocks is perpendicular to the wall lasers. The double-emulsion RP (Kodak, therapy localization) film is placed between the metal-plates while still being in its light tight envelope, since this is how it is generally employed. The detector is held firmly together by a plastic frame which is tightly clamped, and is placed against the exit side of the blocks. After irradiation with a beam field size of 40.0 x 80.0 mm<sup>2</sup> at the entrance side of the blocks, the film is developed and the ratio between the optical density values of the peak and tail portions of the LSF image is determined using a densitometer (Macbeth TD-502, diffuse type densitometer with upper range of 4.00 optical density). The slit assembly is then translated one-half millimeter perpendicular to the beam direction using the controller, and then another film is placed between the plates and irradiated again. This process is repeated until the ratio between the peak of the LSF and the tail of the LSF is the greatest, at which point the slit is centered with the X-ray source.

Once the slit is aligned with the center of the radiation source, each metal-plate/film combination is then placed, in turn, abutting the exit side of the blocks and is irradiated to a high and low exposure on separate films. The source to block distance (SBD) is fixed at 115 cm. In all, forty-nine different detector metal-plate combinations are studied and they are listed in Table 3.1. The metal-plates are of aluminum (Al), copper (Cu), brass, and lead (Pb) compositions and varied in thicknesses from 0.30 to 4.80 mm. The approximate densities for the different types of metals are: Al (2.7 g/cm<sup>3</sup>), Cu (8.7 g/cm<sup>3</sup>), brass (8.5 g/cm<sup>3</sup>), and Pb (11.3 g/cm<sup>3</sup>). The Kodak RP film is used with all of the metal-plate combinations. Two different therapy machines are used for the study: a Theratron Co-60 unit and a Varian Clinac-18 unit which emits a 10 MV polyenergetic spectrum of X-rays shown in Fig. 3.2.

Two RP films are exposed per detector: The first film is exposed to a low value and is used to get information about the peak of the LSF and, the second film is exposed between 10 - 100 times the first to obtain well defined LSF tails that have values that are  $\sim 1 \times 10^{-2}$  times the peak value. The tails are always less exposed than the peak because photons or electrons are scattered more centrally. This gives rise to a lower counting statistics in the tails resulting in larger uncertainty. Therefore, a second film is exposed to increase the number of events in the tail regions. The data from the two films are then concatenated digitally.

Table 3.1 Front /back metal-plate combinations used with the RP portal localization film.

	Detectors					
	Front Plate	Thickness		Back Plate	Thickness	
		g/cm <sup>2</sup>	mm		g/cm <sup>2</sup>	mm
1	Cu	0.837	0.95	Al	0.186	0.60
2	Cu	0.837	0.95	Al	0.434	1.62
3	Cu	0.837	0.95	Al	0.872	3.22
4	Cu	0.837	0.95	Al	1.299	4.81
5	Cu	0.837	0.95	-		
6	Cu	1.558	1.75	Al	0.186	0.60
7	Cu	1.558	1.75	Al	0.434	1.62
8	Cu	1.558	1.75	Al	0.872	3.22
9	Cu	1.558	1.75	-		
10	Cu	2.158	2.40	Al	0.186	0.60
11	Cu	2.158	2.40	Al	0.434	1.62
12	Cu	2.158	2.40	Al	0.872	3.22
13	Cu	2.158	2.40	-		
14	Pb	0.404	0.39	Al	0.434	1.62
15	Pb	0.404	0.39	-		
16	Pb	1.241	1.10	Al	0.186	0.60
17	Pb	1.241	1.10	Al	0.434	1.62
18	Pb	1.241	1.10	Al	0.872	3.22
19	Pb	1.241	1.10	-		
20	Pb	1.458	1.31	Al	0.434	1.62
21	Pb	1.458	1.31	-		
22	Pb	2.335	2.05	Al	0.434	1.62
23	Pb	2.335	2.05	-		
24	brass	2.595	3.07	Al	0.186	0.60
25	brass	2.595	3.07	Al	0.434	1.62
26	brass	2.595	3.07	Al	0.872	3.22
27	brass	2.595	3.07	-		
28	Cu	1.558	1.75	Cu	0.228	0.30
29	Cu	1.558	1.75	Cu	0.720	0.80
30	Cu	1.558	1.75	Pb	0.404	0.39
31	Cu	1.558	1.75	Pb	1.241	1.10
32	Pb	1.458	1.31	Cu	0.228	0.30
33	Pb	1.458	1.31	Cu	0.720	0.80
34	Pb	1.458	1.31	Pb	0.404	0.39
35	Pb	1.458	1.31	Pb	1.241	1.10
36	brass	2.595	3.07	Cu	0.228	0.30
37	brass	2.595	3.07	Cu	0.720	0.80
38	brass	2.595	3.07	Pb	0.404	0.39
39	brass	2.595	3.07	Pb	1.241	1.10
40	Al	0.872	3.22	Cu	0.228	0.30
41	Al	0.872	3.22	Cu	0.720	0.80
42	Al	0.872	3.22	Pb	0.404	0.39
43	Al	0.872	3.22	Pb	1.241	1.10
44	-			Cu	0.720	0.80
45	-			Pb	1.241	1.10
46	-			brass	2.595	3.07
47	-			Al	0.434	1.62
48	-			Al	0.872	3.22
49	-			-		

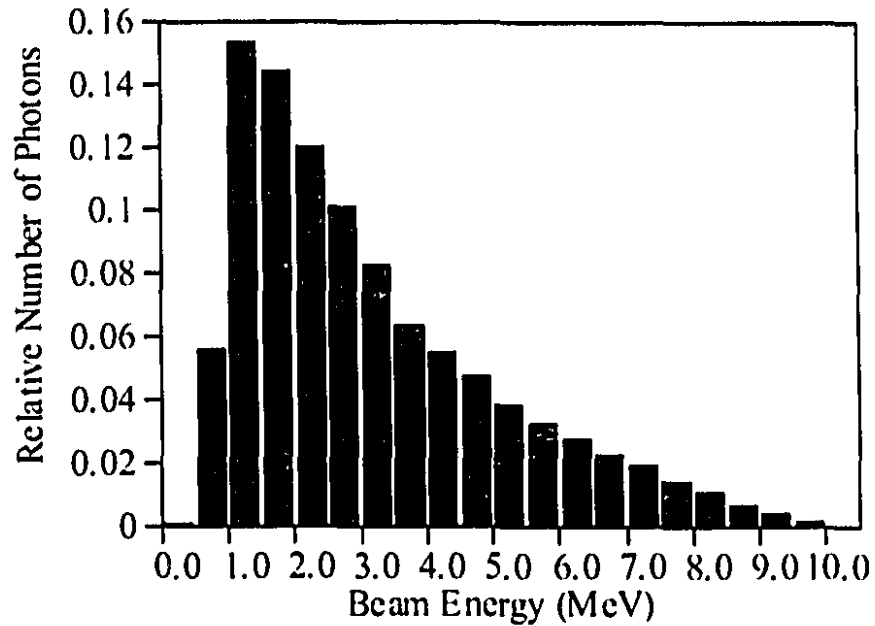


**Figure 3.2** *Spectra emitted by the Clinac-18 therapy machine in the 10 MV photon mode. Calculated using the EGS4 simulation package for a source-to-detector scoring distance of 190 cm (see section 3.3 for details).*

### 3.1.2.2 Film H & D curves

The fact that we use linear systems theory to study a non-linear system such as film must be addressed. The film characteristic curve is determined for each film batch used in the following manner: The film and a calibrated ion chamber are interchanged at the same depth within polystyrene for different ranges of exposure settings on the Co-60 and Clinac-18 therapy machines. The optical density readings from the films are then obtained with the Macbeth TD-502 diffuse type densitometer. These characteristic curves (optical density versus relative dose) are then used to convert optical density readings from the film to exposure readings, thus linearizing the LSF data sets. The LSF data was collected on four separate days and Fig. 3.3 shows the characteristic curves for each of the film batches used on these days. There is a small yet detectable difference between the batches, but no difference between the therapy machines.

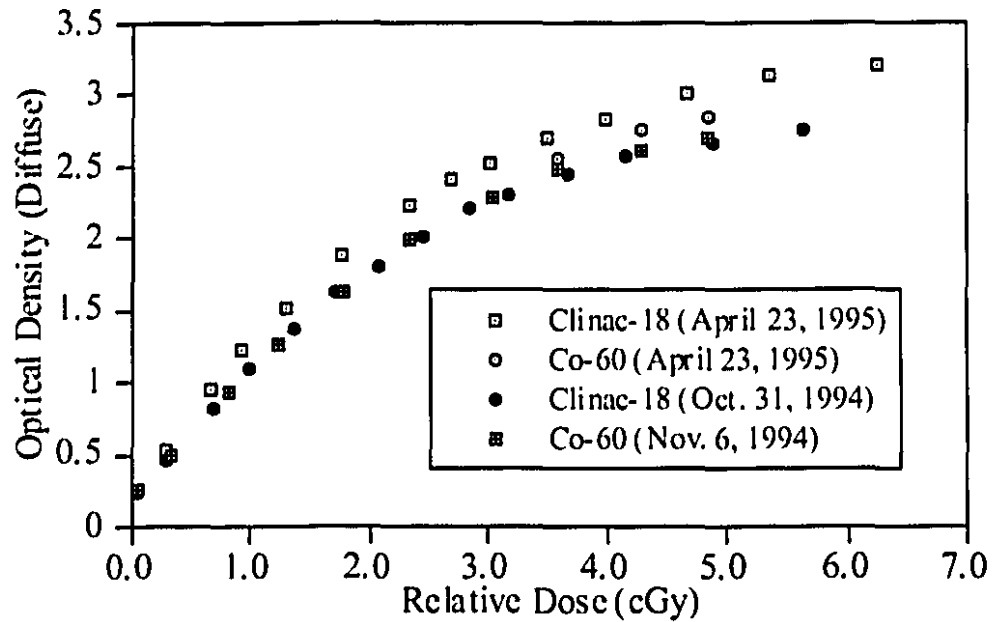


**Figure 3.3** *RP film characteristic curves obtained on four separate days for the two therapy machines.*

Relative dose is used instead of absolute dose because the mass absorption coefficients of film and polystyrene, for which the chamber is calibrated, are different. The film is placed at the position of the center of the ion chamber. The point gradients  $\gamma$  for each film batch and machine energy are obtained using the data in Fig. 3.3 and Eq. (2.55). The points gradients for April 23 (Clinac), April 23 (Co-60), Oct. 31 (Clinac), and Nov. 6 (Co-60) are 1.79, 1.70, 1.71, and 1.70, respectively.

### 3.1.3 Processing techniques

#### 3.1.3.1 LSF digitization

A microdensitometer is used to digitize the LSF images from each detector. The microdensitometer scanning slit has dimensions 10 by 400  $\mu\text{m}$ . The 10  $\mu\text{m}$  aperture width is used to obtain a relatively low, maximum systematic error of 2 % at 10 cycles/mm (see Section 2.2.3), before applying corrections for finite aperture size. The scanning interval is 5  $\mu\text{m}$  in accordance with the Nyquist criterion. Each detector LSF is obtained by scanning the microdensitometer aperture perpendicular to the slit image. Each line is scanned at intervals equal to the length of the aperture, 400  $\mu\text{m}$ . Fifty-one lines are scanned from each

LSF image and these are then averaged to obtain a better estimate of each LSF. Each line consists of 6000 scanned points (i.e., 3000 points on each side of the LSF peak) resulting in a LSF segment of 3.0 cm long, and a scanned area of 3.0 x 2.0 cm<sup>2</sup>. A flip-mode type scan is used and is described in section (3.3).

### 3.1.3.2 Linearization and Callier effect corrections

The microdensitometer is calibrated by scanning the same films from which the characteristic curves of Fig. 3.3. are generated. Because the microdensitometer reads specular density and the Macbeth TD-502 densitometer reads diffuse density, the calibration of the microdensitometer also converts specular to diffuse density. Thus to address the Callier phenomena, the four characteristic curves, for each machine and film batch shown in Fig. 3.3, are scanned using the microdensitometer to obtain the microdensitometer calibration curve in Fig. 3.4, which has a slope of 1.23. The diffuse density data from Fig. 3.4 are then linearized by using the curves in Fig. 3.3 to obtain relative dose data.

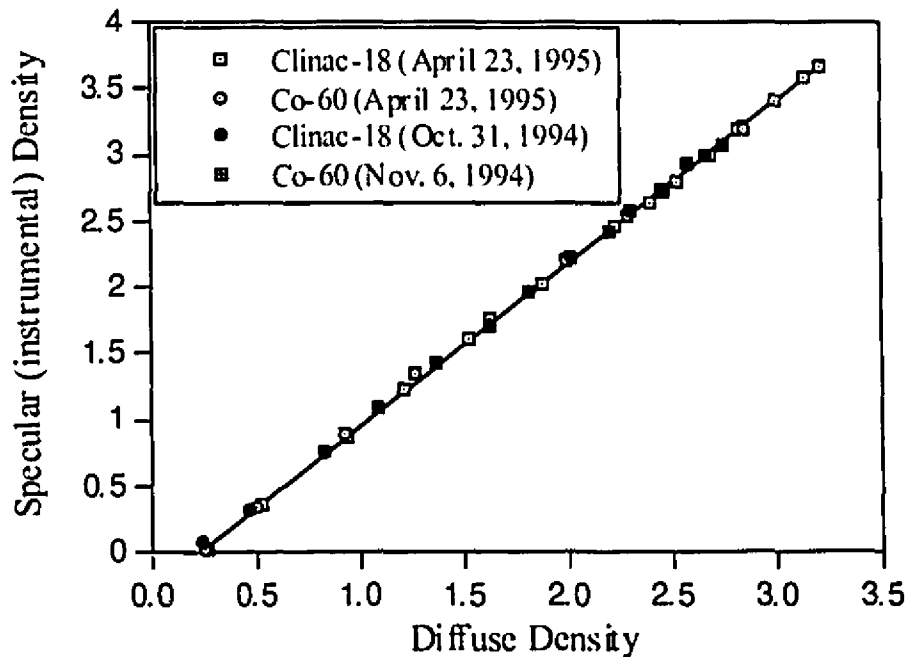


**Figure 3.4** *Microdensitometer calibration curves converting specular density to diffuse density.*

### 3.1.3.3 Processing the digitized, linearized LSF

The background noise for a typical raw data LSF image is shown in Fig. 3.5, and has a standard deviation of 3 % the peak value. This background noise gives rise to two sources of error in megavoltage MTF estimates<sup>2</sup>: (1) The background of the LSF can not be accurately estimated, rendering estimates of the area under the LSF inaccurate and causing systematic errors in the MTF values. Because the MTF is normalized at zero frequency where  $MTF(0)$  is equal to the area below the LSF curve, the MTF values at all spatial frequencies will be greater than or less than the true values depending on whether the area under the LSF is under or over estimated, respectively. (2) Since noise has more higher frequency components,<sup>14-17</sup> MTF spectral estimates will be incorrectly biased towards higher values. Processing steps are taken to reduce the noise level in the scanned LSF and thus reduce systematic errors in estimates of the MTF.

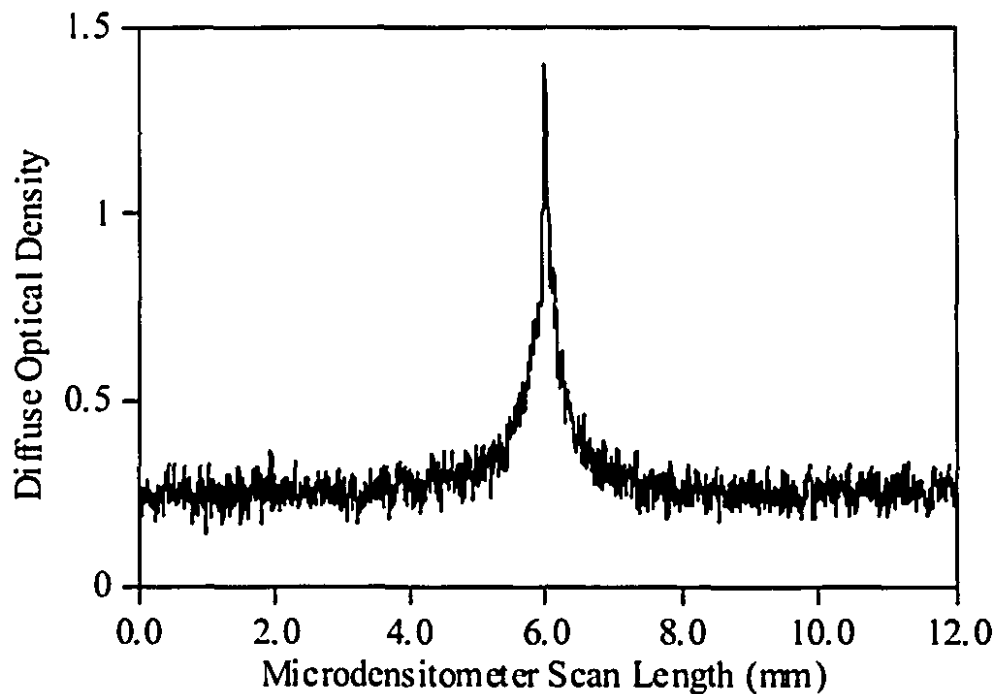


**Figure 3.5** Typical raw data LSF image showing background noise caused mainly by the film granularity.

First, to reduce noise in the LSF, a large contrast LSF is desired. As discussed earlier, the LSF obtained at megavoltage energies is of much lower contrast than those obtained at diagnostic energies. To obtain high contrast LSFs a relatively large exposure slit width and concatenation of the high and low exposure images is used. Figure 3.5

shows a typical raw data, concatenated LSF. Corrections for the finite slit width are small compared to those resulting from large variations in background when dealing with megavoltage slit images. At megavoltage energies we are concerned with spatial frequencies generally below 10 cycles/mm, and a 25  $\mu\text{m}$  exposure slit causes little effect in this domain. The situation is different at kilovoltage energies where spatial frequencies of interest are of the order  $> 100$  cycles/mm. In this case, smaller slit widths are used and slight misalignment of the small slits can significantly alter the effective width of the slit exposures thus making finite width corrections more inaccurate.<sup>2</sup>

Furthermore, noise reduction in LSFs is obtained by averaging over a large number of independent LSF estimates. The slit image is scanned several times at intervals equal to the scanning aperture length of the microdensitometer (i.e., 400  $\mu\text{m}$ ). Random fluctuations in the LSF averaged scan are reduced by  $\sqrt{n}$  where  $n$  is the number of individual scans acquired, for our case 51 per detector type. An equivalent method is to scan the slit image once but with a microdensitometer whose slit length  $l$  is very long. In this case, the signal is averaged through the summation of a larger scanned area at each point. It is more difficult to scan with a larger slit since small misalignments of the scanning slit aperture relative to the LSF slit image are accentuated for long scanning slits. If the scanning direction is skewed instead of perpendicular to the slit image then the averaging process will widen (distort) the LSF: (Fig. 3.6). The LSF will no longer be convolved with a rectangular function but with a trapezoidal function whose shape is dependent on the scanning angle  $\theta$ . A generalization of misalignment correction for small scanning slits, as well as for large, will be discussed shortly<sup>18-19</sup> (see Section 3.1.3.4).

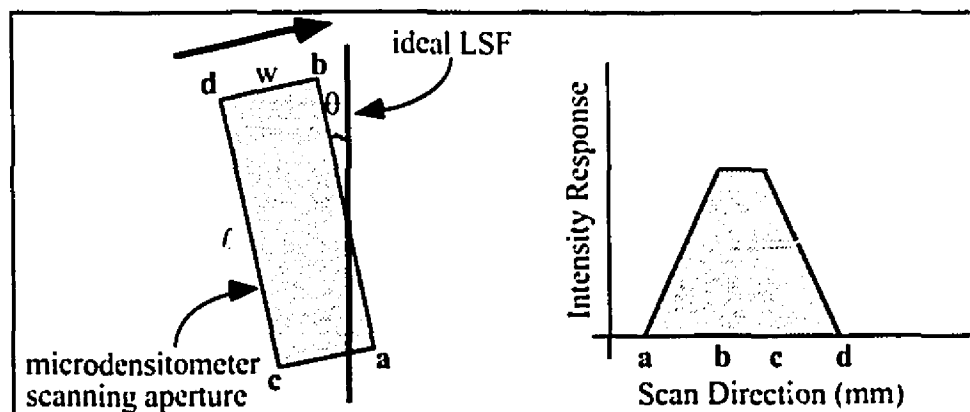


**Figure 3.6** Distorted LSF due to the fact that the scanning motion is not perfectly perpendicular to the slit image

The misalignment of the scanning slit relative to the image of the LSF slit not only causes distortions in the shape of each individual LSF, but also causes a shift between the relative position of the peaks of each successive LSF, as is depicted in Fig. 3.7. This peak shifting would cause further systematic distortions in the averaged LSF.

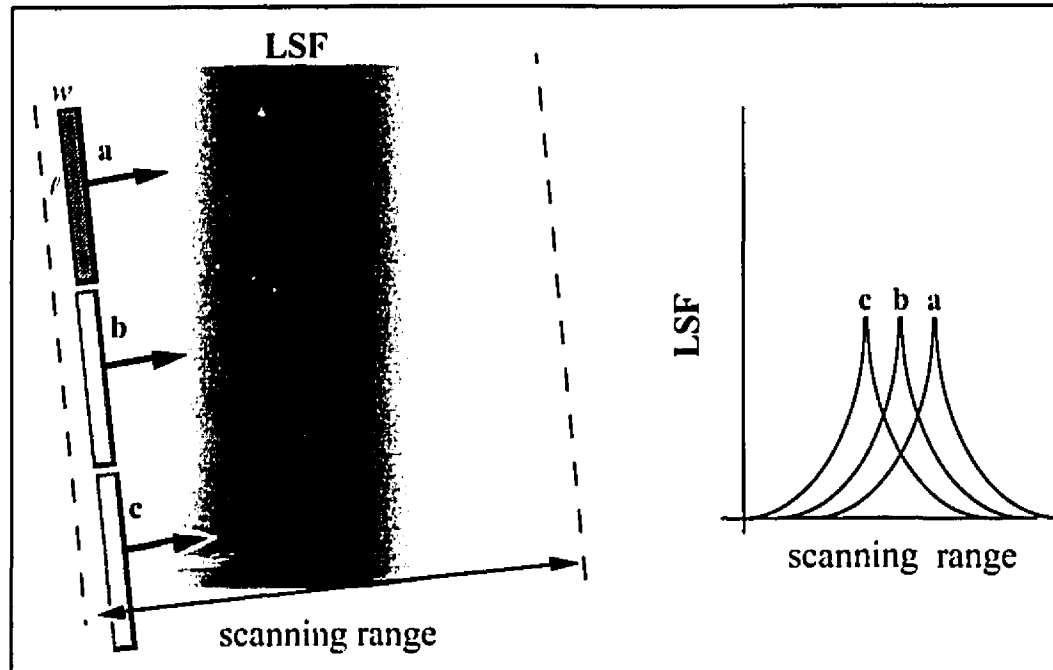


**Figure 3.7** Distortions in the shape of the averaged LSF due to misalignment between scanning aperture and LSF slit image.

An algorithm is written to deal with the systematic shifting between successive LSFs peaks: The algorithm searches for the locations of the peak values of all of the 51 LSFs scanned per film. Then, each of the successive LSFs has a corresponding number of readings removed from the beginning of each LSF data set so that each of the peaks coincide for all 51 LSFs. Three thousand points, centered on the peak of each LSF, are then extracted and the average of these resulting LSFs is obtained. Tails that are 7.5 mm (1500 x 5  $\mu\text{m}$ ) long are chosen. At 7.5 mm from the LSFs' peaks, the density readings correspond to the base and fog densities of the film, which insures that the LSF is not truncated prematurely.

Because the 51 LSFs are symmetric about their peaks, we further reduce noise by averaging the two halves of the averaged LSF about its center. In Fig. 3.8 we show a typical LSF that results from the averaging of 51 raw LSFs and averaging the resulting LSF about its peak. The steps to obtain the LSF in Fig. 3.8 can be summarized as follows:

the original microdensitometer scan is converted to diffuse density, and linearized, the peaks of the 51 LSFs are aligned and averaged, and its halves are averaged about the peak. Except for the Hanning filter which is also described below, the rest of the correction factors are applied in the spatial frequency domain after application of the FFT to the LSF.

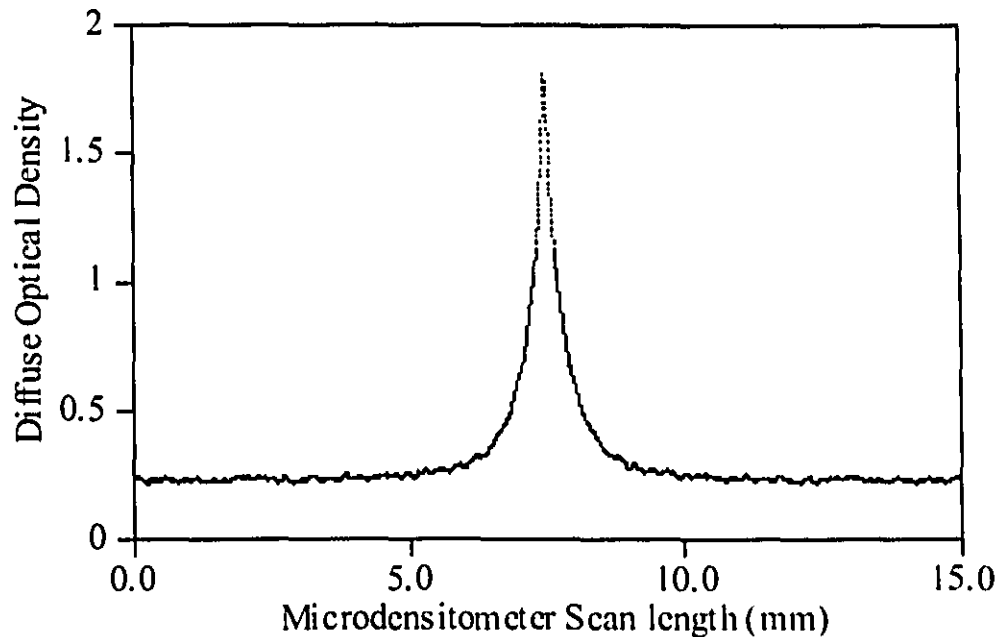


**Figure 3.8** Typical LSF which corresponds to the average of 51 LSFs and the average of its halves.

### 3.1.3.4 Corrections applied in the Fourier domain

Due to the discrete nature of the data, the peak value of the digital LSF does not correspond to the true center of the averaged LSF. The method used to determine this discrepancy is as follows<sup>2,6</sup>: A symmetric function, such as the Gaussian exponential, is fit to the averaged LSF and the discrepancy  $c$  between the peak of the symmetric function and the peak of the digitized LSF, is obtained. After folding about the digital peak, truly symmetric locations in the tails are shifted by an amount  $2c$  from the true center. This shift causes systematic errors in the resulting MTF and are corrected by multiplying the MTF by the following factor derived by Droege<sup>2</sup>:

$$\frac{2\sin(2\pi uc)}{\sin(4\pi uc)} \quad (3.1)$$

The incorrect estimation of the background level would contribute in the largest degree to the systematic error in the MTF values<sup>1-5</sup>. To determine the background noise more confidently, the noise in the LSF tails is reduced by applying a moving average of  $S$  points to the averaged LSF. This procedure is repeated for every LSF because the intensification factor and thus the background level for different plates differ. The background is subsequently subtracted from the LSF. The distortion in the final MTF due to the smoothing procedure is then removed by multiplying the MTF by<sup>2,3</sup>

$$\frac{S \cdot \sin(\pi u \Delta x)}{\sin(S \pi u \Delta x)} \quad (3.2)$$

As stated earlier, the phase component of the Fourier transform of a noise sample varies rapidly as a function of frequency. This implies MTF noise derived from a noisy LSF can be reduced by replacing the transform value at a given spatial frequency by the weighted average of data points in a bin centered at the frequency in question. This convolution in the spatial frequency domain is more easily accomplished by multiplying the LSF by an appropriate function in the spatial domain. The function that is best suited for this is the Hanning (Tukey) function given by<sup>16</sup>

$$H(x) = \frac{1}{2} \left( 1 - \cos\left(\frac{\pi x}{Z}\right) \right) \quad (3.3)$$

where  $2Z$  is the length of the sampled data. If  $2Z$  is chosen to equal the length over which the data is sampled then the averaging in frequency space will be approximately a three point average with the center point given twice the weighting of the adjacent points. If the value for  $Z$  chosen is decreased, then the tails of the LSF function will be 'chopped off' at the ends and the average in the spatial frequency domain will be over a larger number of points. This truncation of the LSF is potentially dangerous since it can lead to unwanted ringing in the MTF and can also lead to an over estimation of the values of the MTF due to the decrease in the measured normalizing value at (MTF(0)). In addition, by truncating the LSF with smaller  $Z$  in the Hanning function,  $\Delta u$  is increased since  $\Delta u$  is related to the reciprocal of the length of the LSF. Thus, a decrease in  $Z$  results in a smoother but less accurate MTF.

Other techniques<sup>3-4</sup> are also used to diminish the amount of noise in the tails of the LSFs. A common one is to fit an analytic curve to the tails of the LSF function. Typically an exponential function is fit to the tail portion of the LSF for values below 10 - 15 % of

the LSF's maximum value and the analytical function is used to replace the noisy values of the tails. Since the fit will contain less random noise, the MTF values will also be less noisy. Since only a portion of the tails are fit by the model, care must be taken not to create discontinuities where the LSF values end and where the analytical fit begins. Incorrect fitting model or discontinuities will result in systematic errors for the MTF values. Another method used to reduce the noise in the tails is by truncating the tails of the LSF. To avoid truncation artifacts, the area under the LSF must not change significantly. This assumes knowledge of the LSF tails which is difficult due to the additional problem of determining the background value. Thus, we choose not to truncate the tails to a value smaller than 7.5 mm which is extremely long by high energy metal-plate/film LSF standards<sup>3-4,20-23</sup> and to deal with the noise in the tails using the Hanning method. The Hanning method is chosen because no radical changes are made to the shape or length of the LSF.

The mixed Fourier transform routine which comes with the DADISP (Cambridge, MA, USA) software package residing on a Sun Sparc 10 workstation, is used to derive the MTF from the LSF. Corrections to the MTF are then made for averaging of the two halves of the LSF and for the smoothing that was performed to more easily estimate the background value. There are several other key corrections to the MTF that are performed in the spatial frequency domain and that are discussed below.

Corrections are done for the finite exposure slit width  $d=25 \mu\text{m}$ , finite scanning aperture width  $w$  of the microdensitometer, and for the scanning slit misalignment with the LSF image, described by  $\theta$ . The last two factors can be incorporated into one factor for correction of microdensitometer scanning characteristics. Corrections for a finite separation  $d$  of the blocks is given by

$$\frac{(\pi u d)}{\sin(\pi u d)} \quad (3.4)$$

Droege developed Villafana's<sup>18</sup> expression for finite slit misalignment to include any angle  $\theta$ :<sup>2-3</sup>

$$\frac{\pi u w \cdot \cos \theta}{\sin(\pi u w \cdot \cos \theta)} \frac{\pi u l \cdot \sin \theta}{\sin(\pi u l \cdot \sin \theta)} \quad (3.5)$$

where  $l$  is the scanning slit length. For perfect alignment  $\theta=0$  and the correction for the finite scanning slit width is obtained.

## **3.2 Measuring the Noise Power Spectrum**

As with Section (3.1), this section will also be divided into two parts: experimental and image processing techniques. The methods used to estimate NPS have been described<sup>24-30</sup>, and we will use the methods of Wagner and Weaver<sup>27-28</sup>.

### **3.2.1 Experimental techniques**

The experimental set up for the NPS determination is similar to the one used for the MTF determination, but, the radiopaque blocks are removed and a trial and error adjustments of the source-detector distances (SDD) and radiation source output are used to obtain a nominal optical density of 1.00 on the detectors' film. The optical density obtained for the various detectors is  $1.00 \pm 0.02$  D. A  $15 \times 15$  cm<sup>2</sup> field size at the detector plane and SDD that is larger than 1.5 m are used to generate  $1.00 \pm 0.02$  D on the RP films per detector. Because different metal-plate combinations have different intensification factors, the SDD distances and the MU and/or irradiation time are varied accordingly to obtain 1.00 D on the films. Table 3.2 lists the detectors types, SDDs and MUs and/or irradiation times used.

The SDD parameter will be subsequently used as one of the input parameters to the EGS4 simulation package (section 3.3) to determine the average fluence per unit area  $\bar{q}$  that is impinging on each of the detectors. NPS measurements are done for only seventeen of the forty-nine detectors used in the MTF section due to time constraints placed on the use of the microdensitometer.

### **3.2.2 Processing techniques**

#### **3.2.2.1 Digitizing the film-uniformly exposed to 1.00 D**

The MTF estimates for the detectors are calculated before the NPS digitization was performed on the films irradiated to a nominal optical density of 1.00. The MTF results showed spectral values with approximately zero intensity beyond 3 cycles/mm.

**Table 3.2** Detectors used for the NPS determination; listed are the MUs (time) and SDD parameters used to generate an optical density of 1.00 on the RP portal film. In the table a dash '-' refers to a detector without a front and/or back plate. The output of our machines at a depth in tissue of dose maximum ( $d_{max}$ ) for the Clinac-18 and the Cobalt-60 unit is 100 cGy/100 monitor units (MUs) at SSD 100 cm and 100 cGy/1.02 min. at SSD 80 cm, respectively.

	Detector				Parameters used to obtain 1.00 D			
	Front plate	thickness (mm)	Back plate	thickness (mm)	Clinac-18		Cobalt-60	
					SDD (cm)	MU	SDD (cm)	time (min.)
1	Cu	0.95	Al	1.62	195	3	225	0.11
2	Cu	1.75	Al	1.62	210	3	225	0.11
3	Cu	2.40	Al	1.62	210	3	225	0.11
4	Pb	1.10	Al	1.62	215	3	230	0.11
5	Pb	1.31	Al	1.62	215	3	230	0.11
6	Pb	2.05	Al	1.62	217	3	233	0.11
7	brass	3.07	Al	1.62	215	3	220	0.11
8	-	-	Al	1.62	200	16	225	0.19
9	Cu	1.75	Pb	1.10	225	2	210	0.07
10	Cu	1.75	Cu	0.80	235	3	240	0.11
11	Cu	1.75	Al	3.22	210	3	225	0.11
12	Cu	1.75	-	-	192	3	210	0.11
13	Pb	1.31	Pb	1.10	238	2	220	0.07
14	Al	3.22	Pb	1.10	210	2	220	0.07
15	brass	3.07	Pb	1.10	230	2	210	0.07
16	-	-	Pb	1.10	190	6	210	0.10
17	-	-	-	-	200	20	225	0.23

Accordingly, the scanning aperture width for the NPS measurements is chosen so as to be faithful within 2 % accuracy to the analog data up to 3.3 cycles/mm. The scanning aperture chosen for the NPS film digitization is 30  $\mu\text{m}$ . The first lobe of the *sinc* function corresponding to this scanning aperture width falls to zero at 33.3 cycles/mm. Thus, a maximum 2 % systematic error occurs at 3.3 cycles/mm (Fig. 2.12). Increasing the aperture from 10  $\mu\text{m}$  to 30  $\mu\text{m}$  allows a larger area of the nominally, uniformly exposed film to be scanned in less time. A larger scanned area gives more precise NPS spectral value estimates since the statistical random error on the spectral values is proportional to the inverse of the length of the record scanned (Eq. (2.41)). The samples are taken at 17  $\mu\text{m}$  intervals and equal to approximately half the aperture width to respect the Nyquist criterion.

The nominally, uniformly exposed central area of the RP portal film is scanned in a rectilinear raster pattern with a microdensitometer employing a scanning aperture at the film plane 30  $\mu\text{m}$  wide by 400  $\mu\text{m}$  long. The 400  $\mu\text{m}$  side of the aperture is perpendicular to the scan direction. The digitized area consists of 6000 points per line in the scan direction and 340 lines each spaced at intervals of 400  $\mu\text{m}$ . Thus, the total area scanned is (17  $\mu\text{m}$  x 6000) 10.2 cm wide by (340 x 400  $\mu\text{m}$ ) 13.6 cm long.

### 3.2.2.2 Synthesizing an 8 mm by 30 $\mu\text{m}$ scanning slit

The length of the scanning slit used is important<sup>24,31-32</sup> (see Section 2.1.4.5, Eq. (2.50)), and in Fig. 3.9 we show the NPS estimates for spatial frequencies ranging from 0.39 to 3.14 cycles/mm for synthesized slit lengths ranging from 0.40 to 8.0 mm, as is obtained from our data. For small spatial frequencies the spectral components are observed to increase with slit length until a saturation value is reached. For a spatial frequency of 0.392 cycles/mm the 0.40 mm slit length gives spectral values that are 50 % less than the saturation spectral values corresponding to a slit length of 8.00 mm. This error reduces to about 25 % at  $\sim 1$  cycle/mm. The different scan slit lengths offer no differences in spectral values at  $\sim 3$  cycles/mm. Thus, because values are underestimated when the slit length is less than 8.00 mm long, this slit must be synthesized by averaging the transmission values derived from the density measurements of 20 adjacent scans. The amount of light transmitted through the scanning aperture is converted to density readings by a logarithmic amplifier in the microdensitometer. Thus before averaging 20 adjacent points, the density readings must be re-converted into transmittance values. To complete the discussion of Section (2.1.4.5) concerning the long, thin scanning aperture to correctly obtain *2-d* information from a *1-d* scan, we required an 8.00 mm long, 30  $\mu\text{m}$  wide slit.

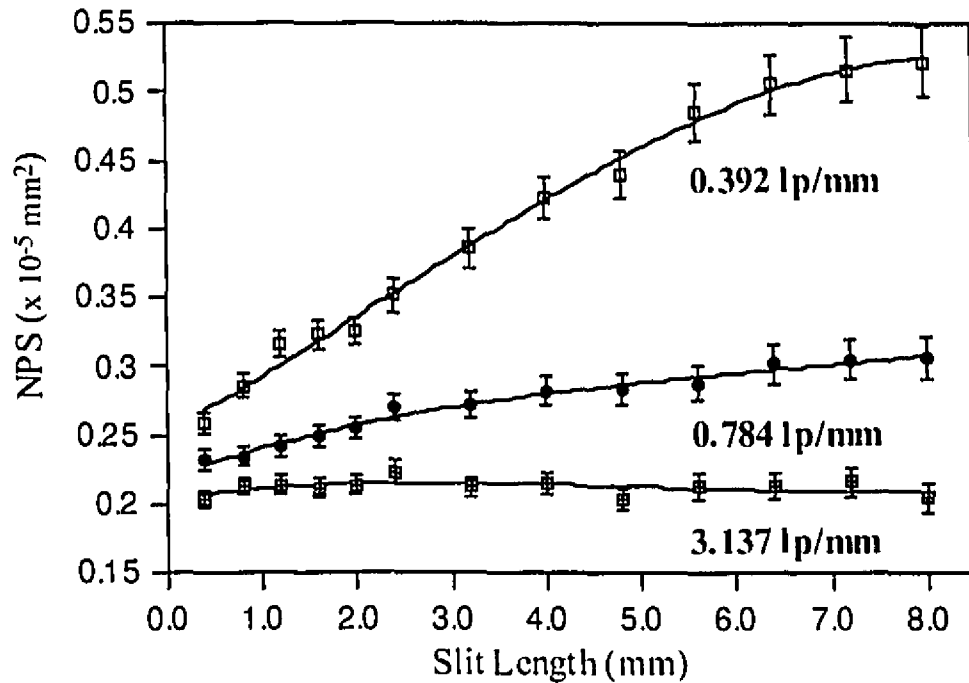


**Figure 3.9** NPS values versus slit length for spatial frequency values of 0.392 cycles/mm, 0.784 cycles/mm, and 3.137 cycles/mm.

To not underestimate NPS values at low spatial frequencies a scanning slit of dimensions 30  $\mu\text{m}$  wide by 8 mm long is required. Since our true scanning slit has dimensions 30  $\mu\text{m}$  wide by 400  $\mu\text{m}$  long the scanning slit required must be synthesized by averaging 20 adjacent scanned lines. We thus appear to be scanning with an 8 mm long aperture and have only 17 raster lines. In this case, each 8 mm long scanned line is called a 'section' scan. Thus, from the total film area scanned, seventeen 'section' scans are generated, each 'section' scan comprises 20 scanned lines (i.e., 20 x 17 = 340). Therefore, with an 8 mm long slit, the total NPS is determined from a total of 6000 x 17 = 102,000 points. A minimum of 100,000<sup>28</sup> points from the film are needed to get a statistically valid estimate for the NPS. The NPS for each of the 17 *l-d* 'section' scans is determined through the technique discussed in Section 3.2.2.3. The final NPS is given as the average of these 17 'sectional' NPSs.

The DQE requires knowledge of both the film characteristic curve point gradient  $\gamma$  and the NPS at one optical density. These parameters both have units that include the square of the optical density. This is achieved by measuring the film characteristic curve

with the same microdensitometer scanning slit that is used to measure the NPS (i.e., 30  $\mu\text{m}$  x 400  $\mu\text{m}$ ).

In the next section we discuss the processing that is applied to each of the 17 'section' scans per detector. The 17 NPS obtained from each of these 17 'section' scans are then averaged to obtain the total NPS for the particular detector.

### 3.2.2.3 'Section' Scan Noise Power Spectra

To provide protection against aliasing error, the data from each 'section' scan are lowpass-filtered by move-averaging of the data by two. The original data scan lines consisted of 6000 points, thus, each 8 mm long 'section' scan synthesized from 20 scan lines also consists of 6000 points. If the 6000 samples in a 'section' scan are designated by  $x_j''$  and the resulting data points, averaged in groups of 2, by  $x_i'$  then

$$x_i' = \left(\frac{1}{2}\right) \sum_{j=i}^{i+1} x_j'' \quad (3.6)$$

where

$$1 \leq i \leq 5999.$$

Low-frequency filtering is then used to remove very low frequency components that arise due to factors such as the physical defects in the emulsion layer and effects caused by the roller marks of the processor or any other local trends<sup>26</sup>. Thus the 5999 points that remain from the lowpass-filtering are averaged in groups of  $n_l$  to yield  $n$  data points  $x_i$  by means of the formula shown below:

$$x_i = x_{i+n_l} - \left(\frac{1}{n_l}\right) \sum_{j=i}^{i+n_l-1} x_j' \quad (3.7)$$

$$n = 5999 - n_l$$

where  $n_l=1000$  to obtain best reproducibility of low-frequency results<sup>27</sup>. Thus, the  $x_i$  are the deviations of  $x_j'$  from a local mean that has a range of 1000 points. The second term in

the above equation corresponds to a moving average over 1000 points. Thus the data points  $x_i$  now correspond to the change in optical density,  $\Delta D$  values.

After filtering, the data points are sectioned into  $K$  overlapping segments (see section 2.1.4.4 for rationale) of  $J$  data points with  $J/2$  overlapping points. Eventually the NPS for each of these segments are determined, and then averaged.

$$K = \frac{n}{(J/2)} \quad (3.8)$$

Since the uncertainty on the spectral values is inversely proportional to the frequency resolution  $\Delta u$ , the length of the segment  $J$  which results in the largest frequency resolution tolerable must be determined. If the largest frequency resolution tolerable is approximately 0.40 cycles/mm then the approximate number of data points  $J$  required in each segment is calculated from

$$\Delta u = \frac{1}{J * \Delta x} \rightarrow 0.40 = \frac{1}{J * 17\mu\text{m}} \rightarrow J \cong 150.$$

With 150 data points for each segment,  $\Delta u=0.392$  cycles/mm, and  $K=66$  segments. The prerequisite to determining  $J$  is to know the sampling interval ( $17 \mu\text{m}$ ) which is determined from the scanning aperture size ( $30 \mu\text{m}$ ). The latter is determined from the spatial frequency range we are interested in. In our case, the maximum spatial frequency we are interested in is 3 cycles/mm which is influenced by knowledge of the MTF results (see section 3.2.2). Choosing a maximum spatial frequency resolution of 0.392 cycles/mm, imposing an uncertainty of no more than 4 % on the spectral values, and using Eq. (2.41) we determine that the length  $R$  of the film that had to be scanned is  $\sim 1600$  mm. Based on this value of  $R$ , we chose to scan a total area of 136 by 102 mm (section 3.2.2) which consisted of 17 lines ('section' scans) 8 mm wide and 102 mm long which amounted to a length  $R= (17 \times 102 \text{ mm})=1734$  mm. By segmenting each 'section' scan into 66 samples will improve our NPS estimates while decreasing frequency resolution.

A window is then applied to the data within each segment which produced the weighting shown below:

$$x_{iw} = x_i \cdot w_i,$$

where

$$w_i = 1 - \left\{ \frac{\left( i - \frac{J-1}{2} \right)^2}{\left( \frac{J+1}{2} \right)^2} \right\}, \quad (3.9)$$

and

$$1 \leq i \leq J.$$

Use of this window in the spatial domain has the same effect as using the Hanning (Tukey) window in the frequency domain<sup>33</sup>, thus decreasing the systematic errors caused by data truncation. The Hanning filter assures that the values of the last and first data points are the same so that no high frequency noise, due to jumps in cyclical data, is introduced. Each segment of the windowed data (i.e.,  $x_{iw}$ ) is then Fast Fourier transformed.

The NPS estimate at a given frequency is the square of the modulus of the Fourier coefficients at that frequency and is given in terms of the Fourier coefficients,  $A_m$  by:

$$NPS''(u) = (J\Delta x/U) |A_m|^2 \quad (3.10)$$

where,

$$U = \frac{1}{J} \sum_{j=1}^J w_j^2 \quad (3.11)$$

and,

$$A_m = \sum_{j=1}^J x_{jw} \exp\{-2\pi im(j-1)/J\}. \quad (3.12)$$

The  $U$  factor normalizes the Fourier coefficients by equating to unity the sum of the spectral weights. Thus a data segment, consisting of deviations of optical densities about a local mean value, is windowed and Fourier transformed. Because of the use of the discrete FFT algorithm, a multiplication by  $(J\Delta x)^2$  is used to obtain correct units, and then multiplication by  $(J\Delta x)^{-1}$  to normalize for the record length. This is equivalent to the factor  $1/(4AY)$  in Eq. (2.35) and is the reason for the  $(J\Delta x)$  factor in Eq. (3.10).

To correct for the smoothing operation that is performed to prevent aliasing, the NPS estimates are rewritten as:

$$NPS'(u) = NPS''(u) \{2 \cdot \sin(\pi u \Delta x) / \sin(2 \pi u \Delta x)\}^2, \quad (3.13)$$

These spectral estimates are then further corrected for the finite extent of the microdensitometer slit width  $w$  and are also multiplied by the effective scanning slit length  $l$ , this provides an estimate of the  $l$ - $d$  slice through the 2-d noise power spectrum (section 2.1.4.5).

$$NPS(u) = NPS'(u) l \{(\pi u w) / \sin(\pi u w)\}^2, \quad (3.14)$$

The spectral estimates from the  $K$  segments are subsequently averaged to yield the spectrum for one of the seventeen 'section' scans. The 17 NPS from the 17 individual 'sections' scans are averaged to obtain the overall spectrum. The above procedures are repeated for each detector listed in Table 3.2.

### 3.3 Determining fluence parameter $\bar{q}$

The semi-empirical method to determine the required fluence to achieve a mean optical density of 1.00 on the Kodak RP film for each detector set up in Table 3.2, is discussed in this section.

Three items are required to determine the absolute fluence impinging onto the detectors: (1) The Fluence to Dose Equivalent Conversion Factor tables from Rogers<sup>34</sup>; (2) the energy spectrum of the Clinac-18 using the Monte Carlo electron-photon transport simulation package; and (3) calibrated absolute dose values at depth of 5 cm within a water phantom.

(1) Rogers used NRCC's EGS3 electron-photon transport simulation package developed at the Stanford Linear Accelerator Center (SLAC) by Ford and Nelson<sup>35-36</sup> to calculate equivalent depth dose to unit surface fluence conversion factors ( $Gy \cdot cm^2$ ). The unit fluence corresponds to that fluence that is impinging onto the surface of a 30 cm-thick slab of ICRU four element tissue equivalent phantom. The factors are calculated for monoenergetic broad parallel photon beams in the 100 keV to 20 GeV energy range, and are quoted in terms of absorbed dose at depth per unit fluence at surface of tissue equivalent phantom. A sample of Roger's tables for energy values ranging from 1 MeV to 3 MeV and for depths in the ICRU tissue equivalent phantom ranging from 0.2 to 30 cm is shown in

Table 3.3. At a depth of 5 cm within the tissue equivalent phantom, the relative dose-to-fluence conversion factor for Co-60 is  $5.96 \times 10^{-12} \text{ Sv} \cdot \text{cm}^2$ .

Table 3.3 Example of Roger's tables.

Depth (cm)	Incident Photons			
	1 MeV Sv x cm <sup>2</sup> (x 10 <sup>-12</sup> )	1.25 MeV Sv x cm <sup>2</sup> (x 10 <sup>-12</sup> )	2 MeV Sv x cm <sup>2</sup> (x 10 <sup>-12</sup> )	3 MeV Sv x cm <sup>2</sup> (x 10 <sup>-12</sup> )
0.20	3.80	3.53	2.70	2.10
0.40	5.38	6.25	6.29	5.13
0.60	5.44	6.42	8.35	7.81
0.80	5.46	6.35	8.63	9.81
1.00	5.49	6.36	8.64	11.0
1.50	5.47	6.37	8.73	11.3
2.00	5.36	6.35	8.66	11.2
2.50	5.39	6.22	8.51	11.0
3.00	5.34	6.23	8.46	10.9
3.50	5.30	6.11	8.41	10.9
4.00	5.14	6.12	8.29	10.9
4.50	5.18	6.09	8.35	10.8
5.00	5.12	5.96	8.30	10.7
6.00	5.02	5.82	8.09	10.6
7.00	4.91	5.79	7.93	10.3
8.00	4.82	5.59	7.89	10.2
9.00	4.64	5.41	7.52	10.1
10.00	4.51	5.32	7.43	10.0
15.00	4.03	4.80	6.91	9.21
20.00	3.35	4.10	5.99	8.34
25.00	2.60	3.37	5.18	7.33
30.00	2.03	2.66	4.20	6.17

(2) The Clinac-18 emits a 10 MV polyenergetic spectrum. Thus, the second step is to calculate the energy spectrum emanating from the Clinac-18 at the SDD of interest (i.e., the SDD for each detector in Table 3.2) using the EGS4 Monte Carlo simulation package<sup>37</sup>. The energy spectrum is used to weigh the depth dose-to-fluence conversion factors for our particular polyenergetic machine. The geometry of the different physical components of our Clinac-18 therapy machine was incorporated into the EGS4 code by Zankowski<sup>38</sup>. An extensive amount of literature has been devoted to the development and explanation of Monte Carlo techniques<sup>39</sup>.

The photon fluence spectrum of the Clinac-18 is calculated relative to the 5 million electrons incident on the Clinac-18 tungsten target used in the EGS4 code, and must give an area normalized to 1. The spectra for the different scoring distances (i.e., SDDs in Table 3.2) are obtained by averaging 5 runs of 5 million electrons each. Although it would be relatively simple to determine the relative fluence from EGS4, it is difficult to determine the incident number of electrons that are used to obtain the mean optical density of 1.00 on the film for each of the seventeen detectors. We thus used Roger's conversion factors. An example of a spectrum obtained from the EGS4 code is shown in Fig. 3.2. This is the Clinac-18 spectrum for SDD=190 cm which corresponds to the relative spectrum incident on detector 16 in Table 3.2. The Clinac-18 energy spectra are divided into twenty 0.5 MeV bins from 0 MeV to 10 MeV. The spectra did not vary much for the range of SDDs listed in Table 3.2.

The weighted conversion factor for each spectrum corresponding to each SDD in Table 3.2, is calculated for the 5 cm depth. A curve is fit to Roger's 5 cm depth dose-to-fluence conversion factors to obtain values for the conversion factors at energies that are required but not calculated by him. Also, instead of equivalent dose and the Sievert (*Sv*) we use dose in Gray (*Gy*) since the quality of photons in the energy range we consider is 1.0, and the dose equivalent is numerically equal to the absorbed dose to tissue.

(3) Once the Roger's conversion factors have been weighted according to the 10 MV spectra for each SDD in Table 3.2 and for a depth in tissue of 5 cm, a tissue equivalent absolute dose reading is obtained at that depth and then multiplied with the weighted dose-to-fluence factor. This results in the average absolute fluence that was impinging onto the film during the NPS measurements.

Table 3.4 lists the measured absolute dose at a depth of 5 cm within tissue, and the corresponding absolute fluence impinging on the different detectors and set up parameters listed in Table 3.2. From Fig. 3.4, it is clear that the use of a front plate and/or back plate increases the sensitivity of the detector because a less photons flux is required to generate 1.00 D on the portal films used with metal-plates.

**Table 3.4** *The absolute dose at a 5 cm depth within tissue and the absolute photon fluence at the surface, for the detectors and parameters listed in Table 3.2. Symbol F in the second column refers to the front plate, B refers to the back plate, and t to their thicknesses. The values are for a field size at SDD of 15 cm x 15 cm, and for a nominal optical density on the detectors' film of 1.00.*

	Detector (F, t; B, t)	Absolute dose and fluence			
		Clinac-18		Cobalt-60	
		Dose (cGy)	$\bar{q}$ (x 10 <sup>6</sup> /mm <sup>2</sup> )	Dose (cGy)	$\bar{q}$ (x 10 <sup>6</sup> /mm <sup>2</sup> )
1	(Cu, 0.95; Al, 1.62)	0.76	8.06	0.96	16.07
2	(Cu, 1.75; Al, 1.62)	0.66	6.96	0.96	16.07
3	(Cu, 2.40; Al, 1.62)	0.66	6.96	0.96	16.07
4	(Pb, 1.10; Al, 1.62)	0.63	6.69	0.90	15.13
5	(Pb, 1.31; Al, 1.62)	0.63	6.69	0.90	15.13
6	(Pb, 2.05; Al, 1.62)	0.62	6.56	0.90	15.13
7	(brass, 3.07; Al, 1.62)	0.63	6.69	1.01	17.70
8	(-, -; Al, 1.62)	3.91	41.32	1.78	29.93
9	(Cu, 1.75; Pb, 1.10)	0.39	4.07	0.62	10.45
10	(Cu, 1.75; Cu, 0.80)	0.53	5.63	0.85	14.23
11	(Cu, 1.75; Al, 3.22)	0.66	6.96	0.96	16.07
12	(Cu, 1.75; -, -)	0.79	8.33	1.09	18.34
13	(Pb, 1.31; Pb, 1.10)	0.34	3.64	0.57	9.60
14	(Al, 3.22; Pb, 1.10)	0.44	4.64	0.57	9.60
15	(brass, 3.07; Pb, 1.10)	0.37	3.91	0.62	10.45
16	(-, -; Pb, 1.10)	1.60	16.95	0.97	16.34
17	(-, -; -, -)	4.87	51.56	2.20	36.90

### 3.4 Microdensitometer: Brief overview

Appendix A has a detailed description of the Perkin-Elmer PDS microdensitometer functional performance and operational sequence<sup>40-41</sup> for the digitization of the optical density of films. Below we give a brief overview of the microdensitometer function and the basic digitization parameters used for this thesis.

The Perkin-Elmer PDS MICRO-10 microdensitometer is a microprocessor-controlled flatbed scanning photodigitizer. It converts the analog (continuous-tone) image into a formatted array of digital values. The two-dimensional array of data constitutes the numerical image of the scanned specimen. This array of data can be stored in computer memory to be processed afterwards. Examples of specimens that can be scanned by the microdensitometer fall in a wide range, but concern any photographic-like object which has a planar distribution of light-attenuating features, such as radiographs, photographic negatives, PC boards, IC masks, maps, tissue samples, etc. The Micro-10 system for digitizing film data can be divided into three subsystems: (1) one for measuring the transmission information; (2) another for moving the stage; and, (3) another for yielding the precise stage position information. Perkin-Elmer guarantees that the difference between the measured and known locations will not exceed +/- 5 microns. We calibrated it to within +/- 1 micron using a calibration test grid that is supplied with the microdensitometer.

The density measurements are acquired by passing a beam of incandescent light from the lower optical system, through the film, and then on to the upper optical system. Light passing through the apertures is collected and measured with a photomultiplier tube (PMT). Digitizing is achieved by sampling the output voltage signal from the PMT at user-defined increments of the stage travel. A sample-and-hold amplifier samples the photometer output signal and holds it at a level until the ADC has had time to complete its function. The ADC digitizes to 12-bit resolution and the least significant bit (LSB) of the ADC is 1.25 mV so that all of the bits are set for an input of 5.12 V ( $2^{12} \cdot 1.25$  mV). During scanning in automatic mode, an onboard micro-processor controls all of the functions of the Micro-10 by continually monitoring the X and Y stage positions, initiating the ADC conversions, formatting the signals, and storing the data. It takes approximately 9 ms for the entire conversion cycle. The manufacturer recommends that the collecting aperture should not be less than 2.8  $\mu\text{m}$  square (at the film plane). The smallest aperture we used at the film plane had dimensions 10 by 400  $\mu\text{m}$ .

Three types of scan modes are available with the microdensitometer (Fig. A.1). The film data in this thesis is scanned using the flip-type mode (Appendix A). The storage buffer used during the digitization process can store a maximum of 3200 pixels (6.4 kbytes) before the digitized data must be dumped to the storage medium. The microprocessor can handle a maximum of 50,000 samples per second. Scanning parameters such as pixel intervals (pixel size is defined by the optics settings, see Appendix B), scan lengths, scan speeds, and the scan-mode are defined through the SCANSALOT program supplied with the microdensitometer.

## References:

- <sup>1</sup> Doi, K., Holje, G., Loo L-N., Snadrik J.M., and Wagner, R.F., "MTF's and Wiener Spectrum of Radiographic Screen-Film Systems," *IIIS Publication FDA*, 82-8187, (1982).
- <sup>2</sup> Droege, R., T., "A megavoltage MTF measurement technique for metal screen - film detectors," *Medical Physics*, 6(4), 272-279, (1979).
- <sup>3</sup> Droege, R. T., Bjärngard, B. E., "Metal screen-film detector MTF at megavoltage X-ray energies," *Medical Physics*, 6(6), 515-518, (1979).
- <sup>4</sup> Munro, P., Rawlinson, J. A., and Fenster, A., "Therapy Imaging: A signal-to-noise analysis of metal plate/film detectors," *Medical Physics*, 14(6), 975-984, (1987).
- <sup>5</sup> Munro, P., Rawlinson, J. A., and Fenster, A., "Therapy Imaging: A signal-to-noise analysis of a fluoroscopy imaging system for radiation therapy localization," *Medical Physics*, 17(5), 763-772, (1990).
- <sup>6</sup> Cunningham, I. A., and Reid, B.K., "Signal and noise in modulation transfer determinations using the slit, wire, and edge techniques," *Medical Physics*, 19(4), 1037-1044, (1992).
- <sup>7</sup> Sanderson, G.K., "Erroneous perturbations of the modulation transfer function derived from the line spread function," *Phys. Med. Biol.* 13, 661-663, (1968).
- <sup>8</sup> Ehrhardt, J.C., "Reduction of aliasing in MTF measurements," *Medical Physics* 13(5), (1986).
- <sup>9</sup> Doi, K., Strubler, K., and Rossmann, K., "Truncation errors in calculating the MTF of radiographic screen-film systems from the line spread function," *Phys. Med. Biol.* 17, 241-250, (1972).
- <sup>10</sup> Rossmann, K., and Sanderson, G., "Validity of the modulation transfer function of radiographic screen-film systems measured by the slit method," *Phys. Med. Biol.*, 13, 259, (1968).
- <sup>11</sup> Morgan, R.H., Bates, L.M., Gopala Rao, U.V., and Marinaro, A., "The frequency response characteristics of X-ray films and screens," *Am. J. Roentgenol*, 92, 426, (1964).
- <sup>12</sup> Cunningham, I.A., and Fenster, A., "A method for the modulation transfer function determination from edge profiles with corrections for finite-element differentiation," *Medical Physics*, 14(4), 533-537, (1987).
- <sup>13</sup> Rossmann, K., Lubberts, G., and Cleare, H.M., "Measurement of the line spread function of radiographic systems containing fluorescent screens," *J. Opt. Soc. Am.*, 54, 187-190, (1964).

- 14 Swindell, W., Morton, E.J., Evans, P.M., and Lewis, D.G., "The design of megavoltage projection imaging systems: Some theoretical aspects," *Medical Physics*, 18(5), 855-866, (1991).
- 15 Sandrik J.M., and Wagner, R.F., "Absolute measures of physical image quality: Measurement and application to radiographic magnification," *Medical Physics*, 9(4), (1982).
- 16 Blackman, R. B., and Tukey, J. W., *The measurement of Power Spectra*, Dover, New York, (1958).
- 17 Blackman, E.S., *Photo. Sci. Eng.*, 12, 244, (1968).
- 18 Villafana, T., "Effect of microdensitometer scan slit misalignment in MTF determinations," *Medical Physics*, 2(5), 255 - 258, (1975).
- 19 Villafana, T., "Modulation transfer function of a finite scanning microdensitometer slit," *Medical Physics*, 2(5), 251-254, (1975).
- 20 Attix, F.H., *Introduction to Radiological Physics and Radiation Dosimetry*, Appendix E, John Wiley & Sons, Inc., (1986).
- 21 Evans, R.D., *The Atomic Nucleus*, Chapters 21, and 25, Krieger Publishing Company, (1955).
- 22 ICRU Report 37, Stopping Powers for Electrons and Positrons, Chapter 12, (1984).
- 23 Barnea, G., Navon, E., Ginzburg, A., Politch, J., Rochrig, H., Dick, C.E., Placious, R.C., "Use of storage phosphor imaging plates in portal imaging and high energy radiography: The intensification effect of metallic screens on the sensitivity," *Med. Phys.*, 18(3), 432-438, (1991).
- 24 Dci, K., Holje, G., Loo L-N., Snadrik J.M., and Wagner, R.F., 'MTF's and Wiener Spectrum of Radiographic Screen-Film Systems', HHS Publ. (FDA), (1982).
- 25 Nishikawa, R.M., and Yaffe, M.J., "Signal-to-noise properties of mammographic film-screen systems," *Medical Physics*, 12(1), 32-39, (1985).
- 26 De Belder, M., and De Kerf, J., "The determination of the Wiener spectrum of photographic emulsion layers with digital methods," *Photo. Sci. Eng.*, 11(37), 371 - 378, (1967).
- 27 Wagner, R. F., and Weaver, K. E., " Noise measurement on rare-earth intensifying screen systems," In : *Medical X-ray Photo-Optical Systems Evaluation, Proc. SPIE*, 56: 1948-207, Palos Verdes Estates, Ca, (1975), and HEW Publication (FDA) 76-8020, (1975).
- 28 Wagner, F.R., "Fast Fourier Digital Quantum Mottle Analysis with Application to Rare Earth Intensifying Screen Systems," *Med Phys.*, 4(2), 157-162, (1977).

- 29 Sandrik, J.M., and Wagner, F.R., "Absolute measure of physical image quality: Measurement and application to radiographic magnification," *Med. Phys.*, 9(4), 540-549, (1982).
- 30 Wagner, R.F. and Sandrik, J.M., "An introduction to digital noise analysis," in: *The physics of medical imaging: Recording System Measurements and Techniques*, A.G., Haus, Ed., American Institute of Physics, New York, New York, 524-545, (1979).
- 31 Sandrik, J.M., and Wagner, R.F., "Radiographic screen film noise power spectrum : variation with microdensitometer slit length," *Appl. Opt.*, 20, 2795-2798, (1981).
- 32 Munro, P., Rawlinson, J.A., Fenster, A., "Therapy Imaging : A Signal - to -Noise analysis of metal plate / film detectors," *Med. Phys.*, 14(6), (1987)
- 33 Roberts R.A., and Mullis, C.T., *Digital Signal Processing*, Addison-Wesley publishing company, Capters 4 and 6, (1975).
- 34 Rogers, D.W.O., "Fluence to Dose Equivalent Conversion Factors alculated with EGS3 for electrons from 100 keV to 20 GeV and photons from 11 keV to 20 GeV," *Health Physics*, 46(4), 891-914, (1983).
- 35 Ford, R.L., and Nelson, W.R., *The EGS Code System*, Stanford Linear Accelerator Center, Stanford, CA, Report No. 210, (1978).
- 36 Nelson, W.R. (Ed.), *Computer techniques in radiation transport and dosimetry*, New York, New York, Plenum Press, (1980).
- 37 Nelson, W.R., Hirayama, H., and Rogers, D.W.O., *The EGS4 code system*, SLAC report No. 265, Stanford Linear Accelerator center, Stanford, CA, (1985).
- 38 Zankowski, C.E., *Monte Carlo analysis of the 10 MV x-ray beam from a Clinac-18 linear accelerator*, M.Sc. thesis, 114 pages, (1994).
- 39 Andreo, P., "Monte Carlo techniques in medical radiation physics," *Phys. Med. Biol.*, 36(7), 861-920, (1991).
- 40 The Perkin Elmer Corporation: Applied Optics Division, *The Perkin-Elmer PDS microd reference manual*, Gary Rogertson & Assoc. Inc., (1983).
- 41 The Perkin Elmer Corporation: Applied Optics Division, *Technical manual: Installation, Operation, and Mintenance Instructions for the Micro-10 microdensitometer system*. Publication No. TM 169B250, (1983).

# **RESULTS AND DISCUSSION**

## **4.1 Modulation Transfer Function**

### **4.1.1 Clinac-18: Modulation Transfer Functions**

It is difficult to appropriately represent the large amount of data generated from the forty-nine front and back plate combinations for each of the two treatment machines. It has been decided to generate figures where each figure corresponded to the MTF data for detectors composed of the same front plate but with varying back plates. Intercomparisons between different figures will be made throughout the discussion to interpret the change in MTF due to different front plate thicknesses and densities. Each detector will be labeled in the following manner: (F, t; B, t), where F represents the type of the front plate, B denotes the type of the back plate, and t identifies the thicknesses of the respective plates.

The precision on the MTF spectral values for all the data is in the order of 2 %. Sections 3.1.3.3 and 3.1.3.4 discuss the averaging techniques used to reduce the uncertainty of the spectral values. A 5 % inaccuracy is also assigned to the spectral values mainly for background-level-estimation systematic error considerations. Taking both the random and systematic errors into consideration we have an overall error on the spectral

values of 7 %. Droege<sup>1</sup> compared theoretical MTFs and simulated MTFs derived from theoretical LSFs without and with a simulated background noise level, respectively. The background noise level had a standard deviation equal to 5 % of the peak value. Using the noise reduction techniques described in sections 3.1.3.3 and 3.1.3.4, he found a maximum overall error in the spectral values of 10 %. We use a 5 % systematic error on the spectral values since the set up techniques that we use are the same as those used by Munro *et al.*<sup>2</sup> Their techniques improve the LSF contrast over those of Droege's, thereby reducing the overall contribution of the background to the LSF and hence to the MTF. The background noise level of our LSF data has a standard deviation of 3 % of the peak value (Fig. 3.5).

Figure 4.1 compares five detectors each with a Cu(0.95 mm) front plate and with varying thicknesses of Al(0.60, 1.62, 3.22, and 4.80 mm) back plates as well as one detector without a back plate. The Al(3.22 mm) back plate offers the best resolution. The worst resolution occurs for the detector without a back plate. This is probably because without a back plate the film is not shielded from the scatter present in the therapy room. These scattered photons degrade the resolution of the image since they have no correlation with the information source. This statement suggests that thicker and denser back plates would give best results since they surely stop all of the scattered photons from reaching the film. Yet, the figure also shows that the resolution with the 4.81 mm thick back plate is not better than that of the 0.60 or 1.62 mm thick Al back plates. From Table 3.4, backscatter increases with back plate thickness<sup>3-5</sup>. This backscatter originates from the electrons that are generated by the photons incident on the front plate, and subsequently impinge on the back plate and then backscatter, or that generate Bremsstrahlung photons. These backscatter electrons and Bremsstrahlung photons degrade the resolution of the image since they originate from electrons that have traversed the thickness of a front plate (from which they are scattered at some angle) and a film<sup>5-6</sup>. Thus, the best back plate should have a thickness and density to minimize backscatter, and to maximize the shielding of the film from room scatter. Since these two criteria demand opposing characteristics from the back plate (thin and less dense on the one hand, and thick and dense on the other), an optimum back plate is to be found. For the 0.95 mm thick Cu front plate, the 3.22 mm thick Al back plate performs best.

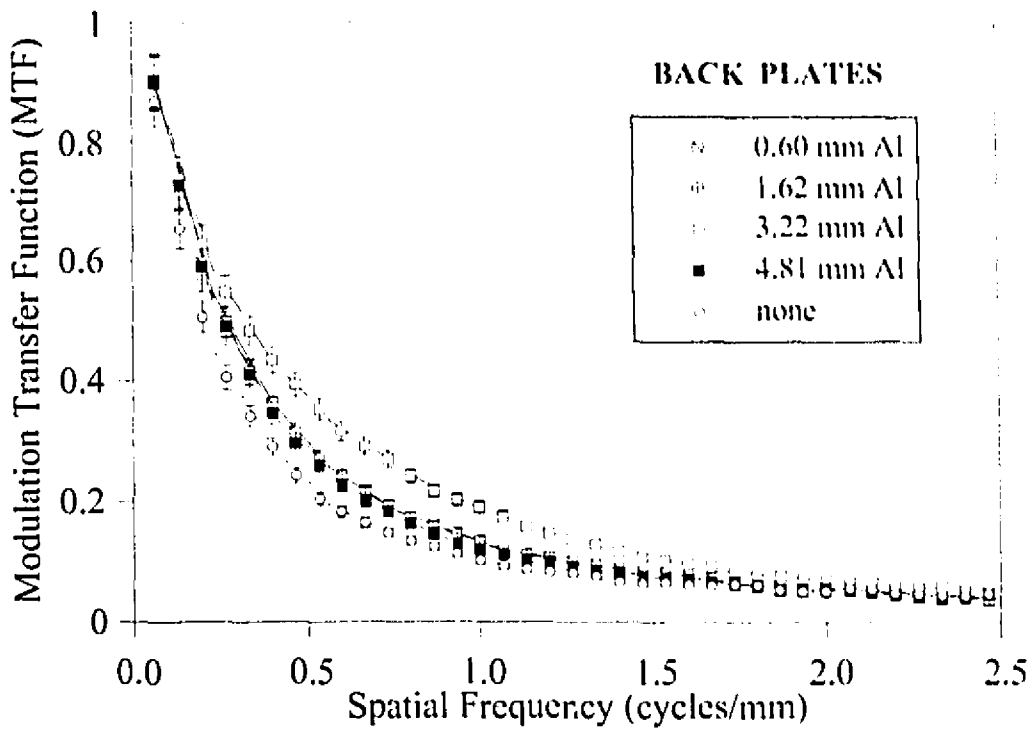


Figure 4.1 Modulation Transfer Functions for detectors with Cu(0.95 mm) front plates and with varying thicknesses of Al back plates or without a back plate.

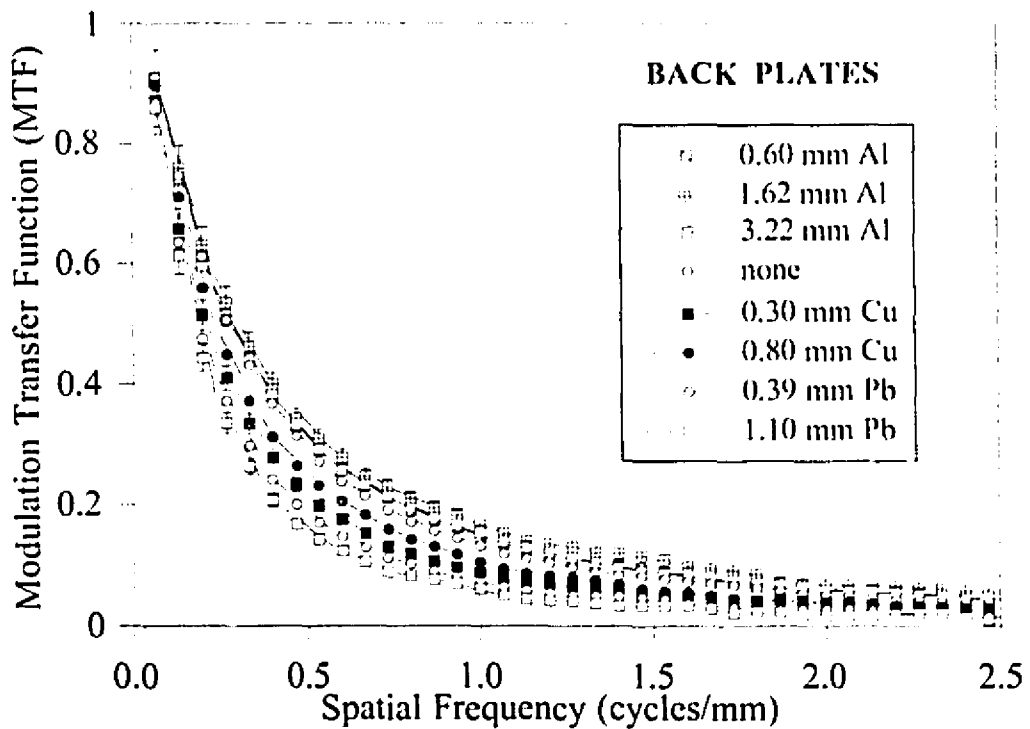


Figure 4.2 MTFs for detectors with Cu(1.75 mm) front plates and with varying thicknesses of Al, Cu, or Pb back plates or without a back plate.

In Fig. 4.2 we compare eight detectors each with a Cu(1.75 mm) front plate combined with back plates of varying thicknesses of Al(0.60, 1.62, and 3.22 mm), Cu(0.30 and 0.80 mm), and Pb(0.39 and 1.10 mm) as well as a detector without a back plate. The Al(1.62 mm) back plate is now the slightly better choice. The resolution is worst when no back plate is used as compared to the Al back plates. However, the detector without a back plate gives better MTF results than those given by the higher atomic number, denser back plates (i.e., Cu and Pb). This is so because, as seen from Table 3.4, the denser plates generate more backscatter. Pb back plates appear to give the worst MTF results. It should also be noted that the MTFs of the Al plates are more or less clustered, suggesting that any of the three Al back plates would perform equally well for the given front plate.

Figure 4.3 shows results obtained for detectors with Cu(2.40 mm) front plates and with Al(0.60, 1.62, and 3.22 mm) back plates, and without a back plate. Again, the worst MTF is obtained when the back plate is omitted. For this thickness of Cu front plate, the thinnest Al back plate (0.60 mm) appears to perform the best. The next best is Al(1.62 mm), followed by Al(3.22 mm). The latter gave best results for the Cu(0.95 mm) front plate. In reviewing Figs. 4.1 to 4.3, we note that as the Cu front plate increases in thickness, the best resolution is offered with successive decreases in thickness of Al back plates. This can be explained as follows: Back plate backscatter originating from primary photons contains spatial information since these photons have not interacted with the front plate and/or film. But this is true but to a lesser degree for backscatter generated by secondary photons which are scattered by the front plate and/or film. With increased thickness of the front plate, the ratio of backscatter generated by scattered as opposed to primary photons increases, given a fixed back plate, because the number of primary photon interactions with the front plate increases with front plate thickness. An increase in this ratio implies a decrease in resolution. This implies that when using thicker front plates, reducing backscatter becomes more important than shielding the film from room scatter. The room scatter depends on the gantry angle, the patient size, patient orientation on the couch, the field size, but insignificantly on the type and thickness of front plate. Thus, for thinner, less dense and lower atomic number (Z) back plates less backscatter and a better MTF is obtained when using progressively thicker and denser front plates. Therefore, for a given thickness of Cu front plate there seems to be a unique Al back plate that offers the best resolution. This discussion implies that a limit in the increase of the thickness of the Cu front plate can be reached whereby the best detector resolution is obtained without a back plate. We will see that this limit is reached for the Pb front plates thicknesses studied.

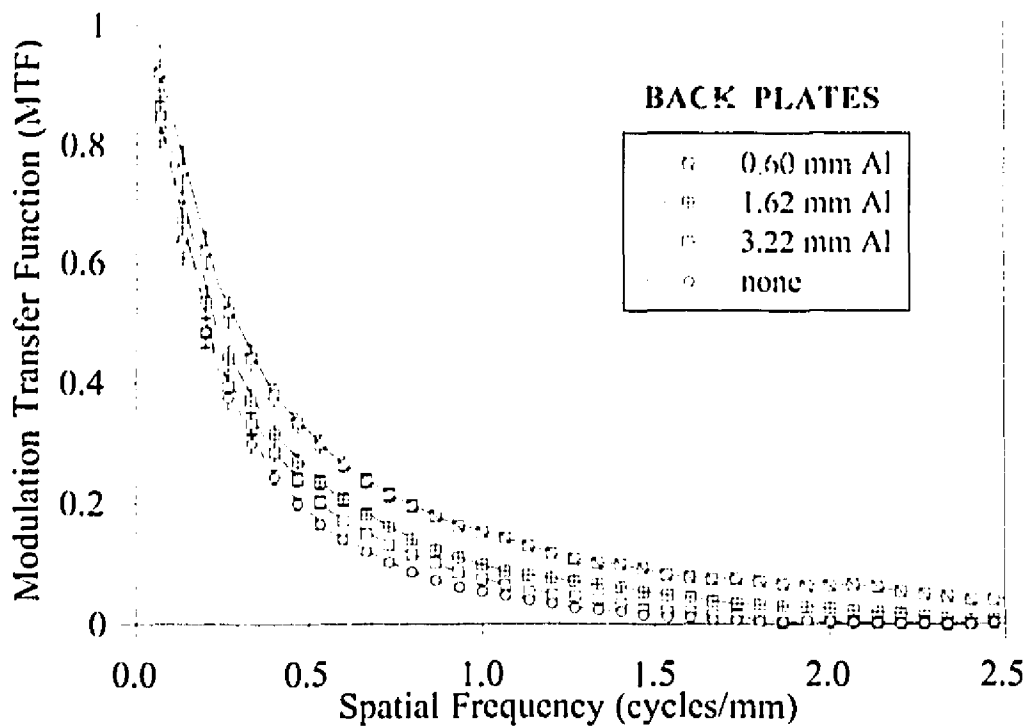


Figure 4.3 Modulation Transfer Functions for detectors with Cu(2.40 mm) front plates and with varying thicknesses of Al back plates or without a back plate.

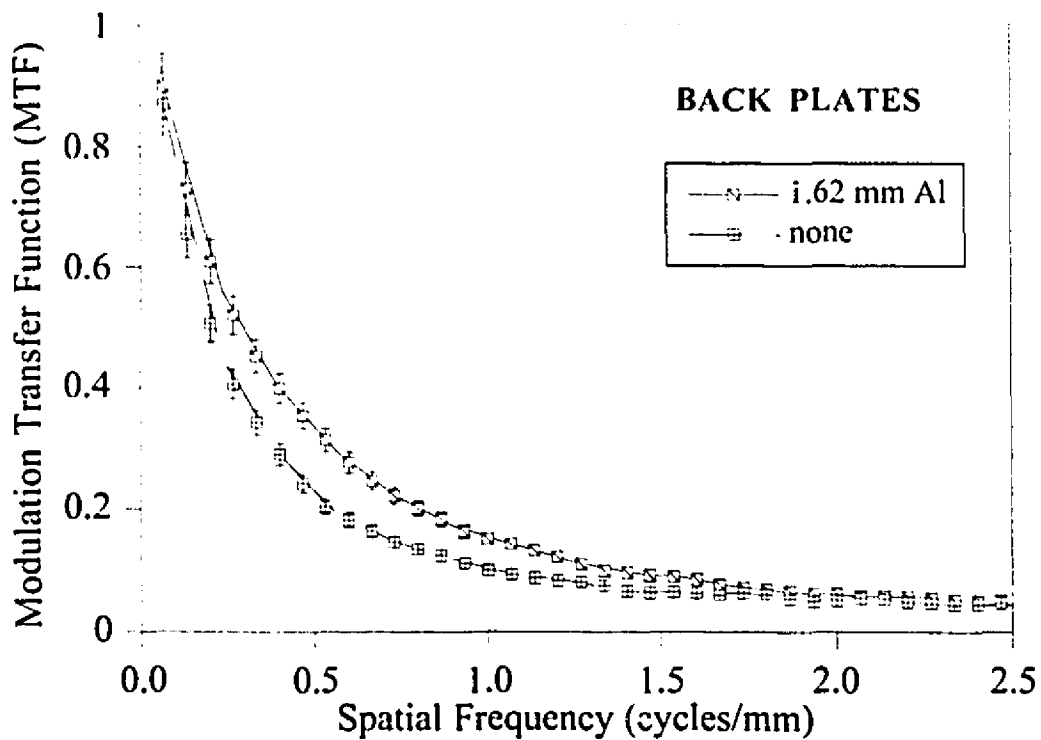
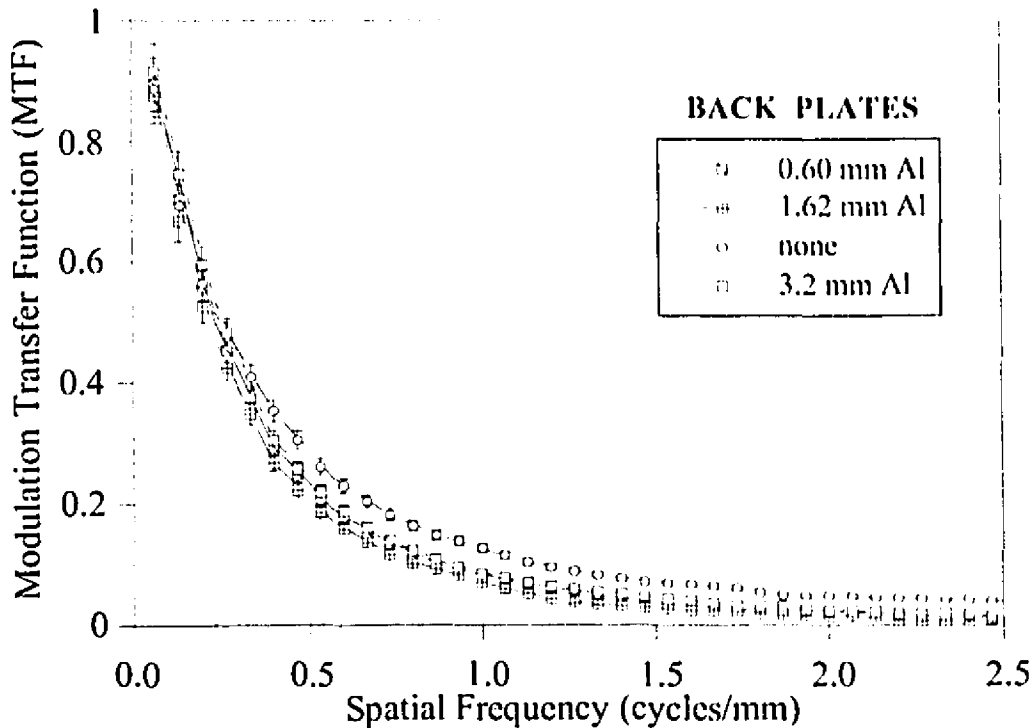


Figure 4.4 Modulation Transfer Functions for detectors with Pb(0.39 mm) front plates and with an Al(1.62 mm) back plate or without a back plate.

In Fig. 4.4, MTFs are compared for the (Pb, 0.39 mm; Al, 1.62 mm) and (Pb, 0.39 mm; none) detectors. For this particular thickness of Pb front plate, the MTF resulting from the use of a back plate is superior to that obtained without a back plate. Figure 4.5 plots the results obtained for a Pb(1.10 mm) front plate with varying thicknesses of Al back plates (0.60, 1.62, 3.22 mm) and without a back plate. The curve without a back plate gives the best results for spatial frequencies greater than 0.3 cycle/mm. We are close to reaching the limit in Pb front plate thickness where the best MTF at all spatial frequencies, is obtained without using a back plate.



**Figure 4.5** Modulation Transfer Functions for detectors with Pb(1.10 mm) front plates and with varying thicknesses of Al back plates or without a back plate.

In Fig. 4.6, detectors have a Pb(1.31 mm) front plate, and back plates consisting of Al(1.62 mm), Cu(0.30, and 0.80 mm), Pb(0.40, and 1.10 mm), and one without a back plate. The Pb back plates give the worst MTFs due to high back scatter contribution, followed by Cu. The detector without a back plate appears to give the best results, followed by the thinner Al back plate. For the limiting case of a detector without back plate, the best resolution is obtained with a 1.31 mm thick Pb front plate. Yet, we have not reached this limiting case for the thickest Cu front plate used (i.e., 2.40 mm) since Cu front plates generate less secondary scatter than Pb. This trend continues in Fig. 4.7, where detector (Pb, 2.05 mm; none) performs better than detector (Pb, 2.05 mm; Al, 1.62 mm).

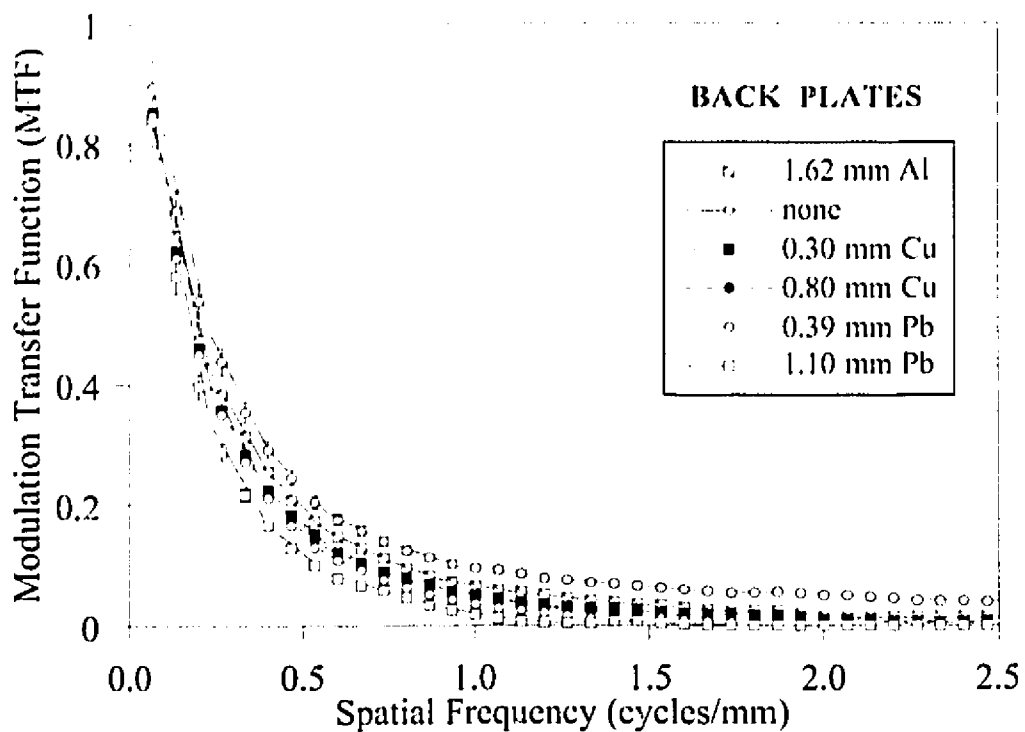


Figure 4.6 MTFs for detectors with Pb(1.31 mm) front plates and with varying thicknesses of Al, Cu, or Pb back plates or without a back plate.

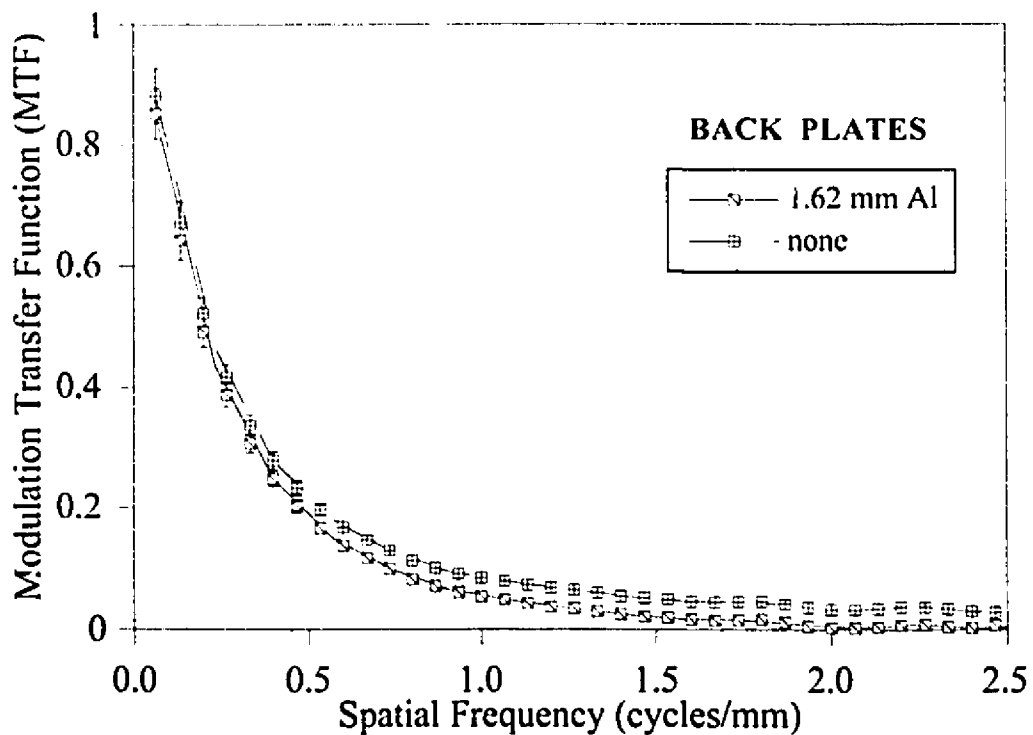
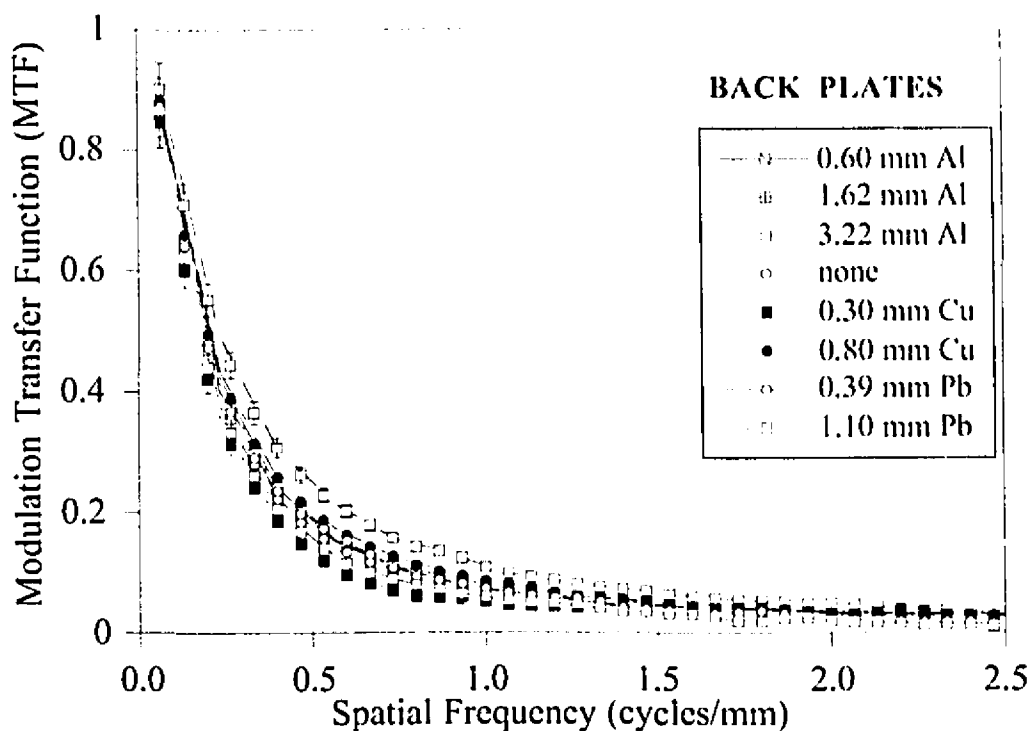


Figure 4.7 Modulation Transfer Functions for detectors with Pb(2.05 mm) front plates and with an Al(1.62 mm) back plate or without a back plate.

In Fig. 4.8, we compare detectors with brass(3.07 mm) front plates and with back plates of the following types: Al(0.60, 1.62, and 3.22 mm), Cu(0.30 and 0.80 mm), Pb(0.40 and 1.10 mm) and one without a back plate. Again, Pb and Cu back plates give the worst MTFs. The best result is obtained with the 3.22 mm thick Al back plate, which is similar to the result obtained with the Cu(0.95 mm) front plate.

In Fig. 4.9, an Al(3.22 mm) front plate is used with Cu(0.30, 0.80 mm) and Pb(0.40, 1.10 mm) back plates. The detector with the Cu(0.80 mm) back plate gives better resolution.



**Figure 4.8** MTFs for detectors with brass(3.07 mm) front plates and with varying thicknesses of Al, Cu, or Pb back plates or without a back plate.

In Fig. 4.10, detectors without a front plate are combined with the following back plates: Cu(0.30 mm); Pb(1.10 mm); Al(1.62 mm and 3.22 mm); (brass, 3.07 mm); and (without). The MTF results suggest that the best in this case would be the Al(1.62 mm) back plate. Except for the 1.10 mm thick Pb back plate which is worst by far, the remainder of the curves are close together. We would expect the best resolution to occur without the use of any front plate or back plate since theoretically there would then be minimal lateral spread and minimal backscatter, respectively. Yet, it appears that an Al back plate gives far better results than detectors without one. This reinforces the premise

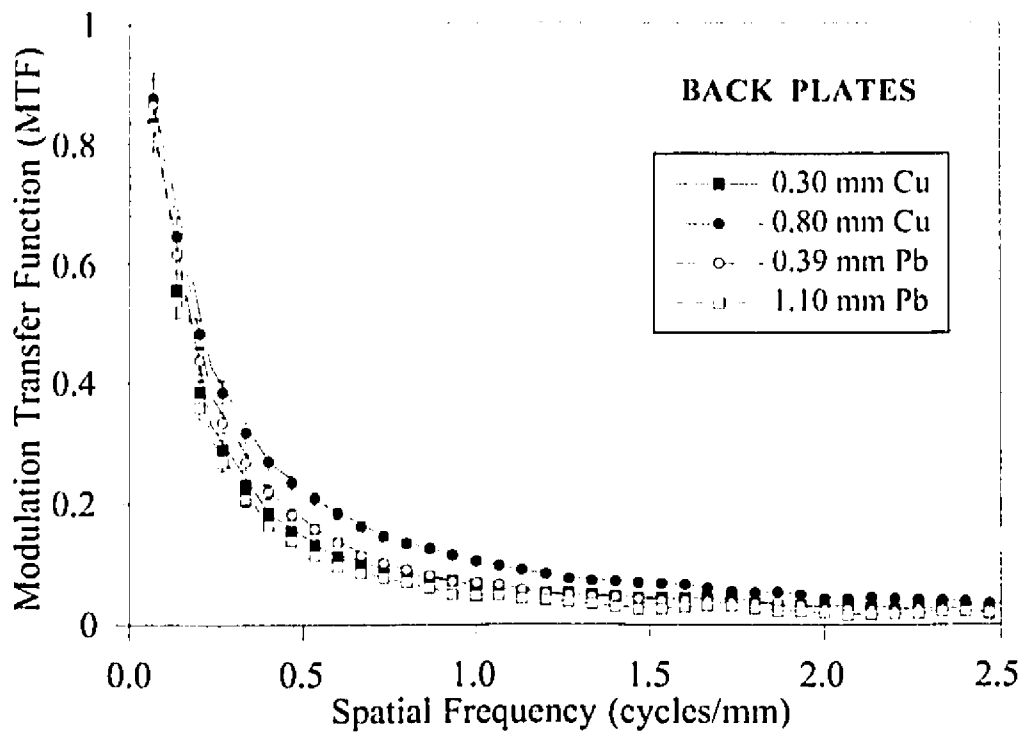


Figure 4.9 Modulation Transfer Functions for detectors with Al(3.22 mm) front plates and with varying thicknesses of Cu, or Pb back plates.

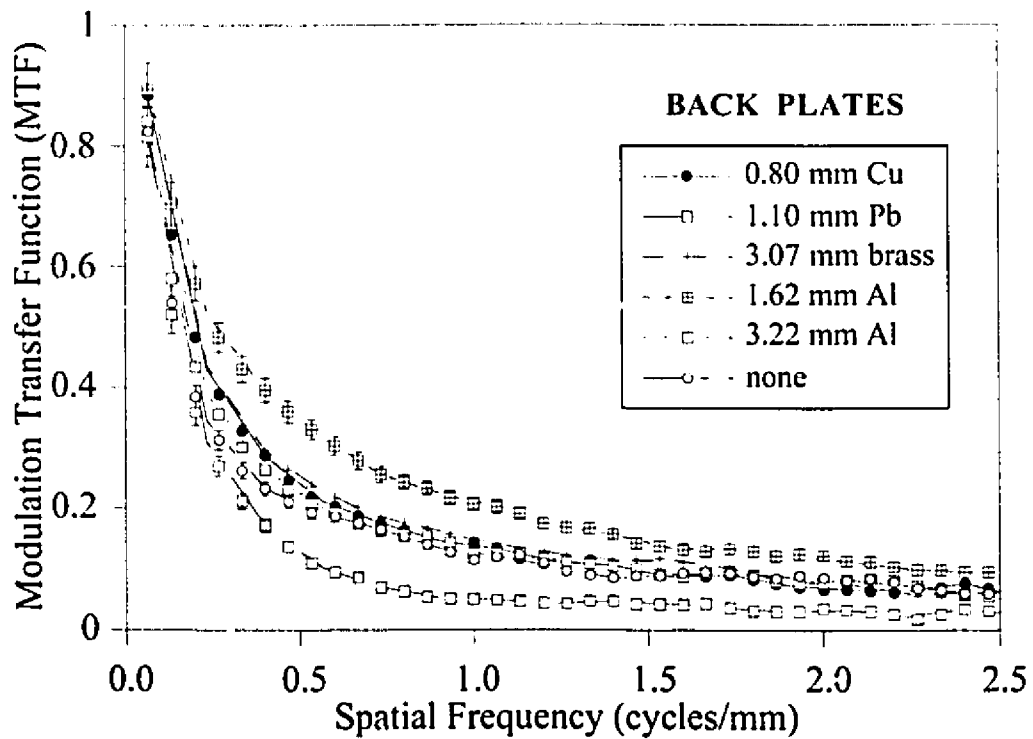


Figure 4.10 MTFs for detectors without front plates and with varying thicknesses of Al, Cu, Pb, or brass back plates or without a back plate.

that removal of room scatter is important and can be achieved through the use of thin, low density, and low atomic number back plates without causing substantial backscatter. Previous studies<sup>7-8</sup> suggest not to use back plates because they worsen the MTF. However, these studies were performed only with high density, high Z back plates (i.e., Cu, and Pb). Scatter contamination from the exit side of the patient must also be considered and when we compare different front plates (see discussion for Fig. 4.11) we will see that the use of a front plate is also required as a means of shielding the film from the scatter generated by the blocks, which simulates patient scatter.

#### 4.1.1.1 Comparing front plates using the Clinac-18 beam

The best MTFs for each front plate used in Figs. 1 to 10, are shown in Fig. 11. The ten best detectors shown are: (Cu, 0.95; Al, 3.22), (Cu, 1.75; Al, 1.62), (Cu, 2.40; Al, 0.60), (Pb, 0.39; Al, 1.62), (Pb, 1.10; without), (Pb, 1.31; without), (Pb, 2.05; without), (brass, 3.07; Al, 3.22), (Al, 3.22; Cu, 0.80), and (without; Al, 1.62). Two conclusions can be made solely from this list before considering Fig. 4.11: (1) The detectors with the best MTFs have Al back plates or no back plates at all. Cu and Pb back plates give the worst MTF results. These low density and low atomic number back plates (e.g., Al) offer the best compromise between ensuring a low back scatter component, and offering a shield from the room scatter. (2) With an increase in the front plate thickness and/or density the best MTF occurs with a decrease in the Al back plate thickness until a limit is reached for the increased front plate thickness whereby the best MTF is obtained without a back plate. This limiting situation is reached with the 1.10 mm thick Pb front plate for frequencies greater than 0.3 cycle/mm, and with the 1.31 mm Pb front plate for the whole spatial frequency domain. For Pb front plates thicker than 1.10 mm, the best spatial resolution is obtained without the use of a back plate.

From Fig. 4.11 we can consider several quantitative effects of front plates on the resulting spatial resolution:

(I) As the thickness of the Cu front plate increases beyond 0.95 mm, the MTF of the system degrades. This effect is due to the added secondary photon scatter and Bremsstrahlung photons generated by the increasing thickness of the Cu plate, rather than the increased lateral spread of electrons since we are beyond the average maximum electron range  $R_{max}$ . We see from Table 3.4 that the Cu front plate generates maximum intensification for a thickness between 0.95 and 1.75 mm. This means that electronic equilibrium is reached within this range implying that  $R_{max}$  is also within this range.

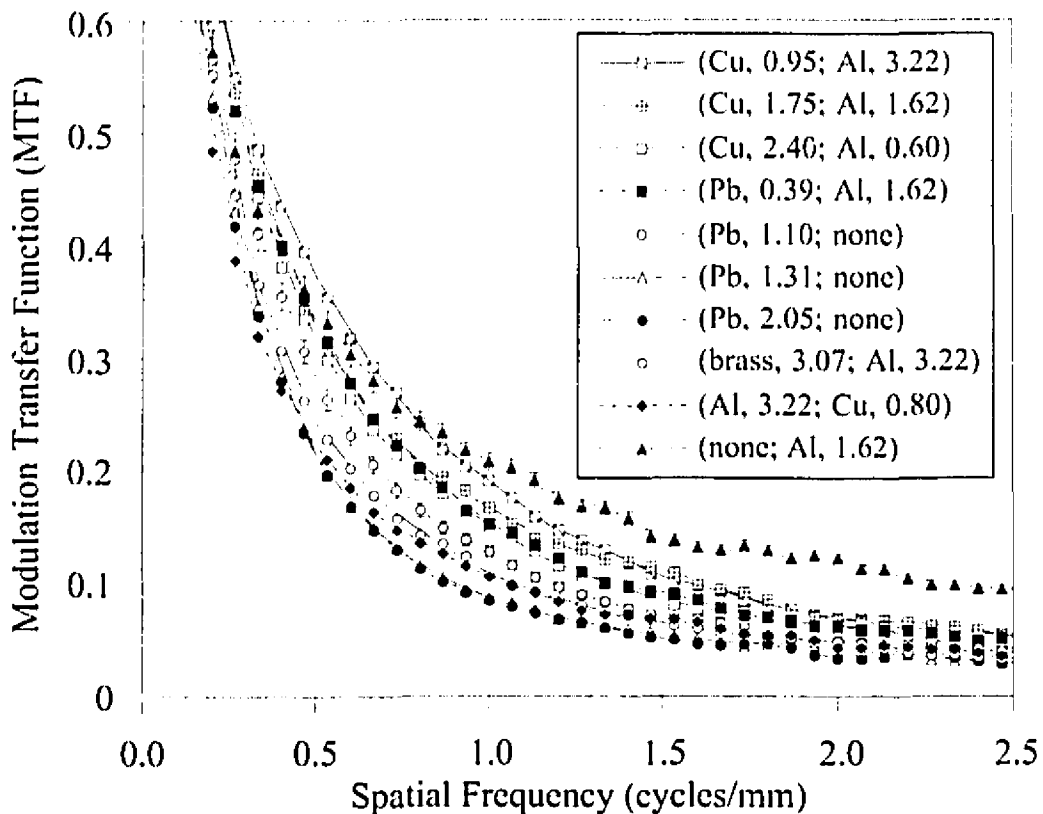


Figure 4.11 MTFs for the best detectors from each of Figs. 4.1 to 4.10

By decreasing the Cu front plate thickness to a value less than  $R_{\max}$ , then (1) the lateral spread would decrease thereby increasing the MTF, but (2) the plate would not be thick enough to completely shield the film from electron contamination generated in the patient, or to preferentially absorb secondary (larger wavelength) photons over primary photons. An optimal plate is sought to balance these two criterion. For the case where the Cu front plate is thicker than  $R_{\max}$  (1) the electron scatter from the patient is removed, and (2) only the electrons generated from the thickness of the Cu front plate equal to  $R_{\max}$  and that are closest to the film will contribute to the resultant spatial resolution. Furthermore, if the electrons generated in the front plate are the only contributors to the spatial resolution, then the MTF would not change with increased thicknesses of the Cu front plate for values greater than  $R_{\max}$ . However, the MTF does decrease when increasing the Cu front plate thicknesses beyond  $R_{\max}$ . This suggests, that in addition to electrons in the front plate, there is another contribution to the MTF: The effect of photon scatter from the front plates can not be ignored even though photons are less likely to be absorbed by the film than electrons generated in the last ' $R_{\max}$ ' layer of the plate. Since photon scatter increases with

increased thickness of the front plate it would be a likely candidate for the decrease in MTF with front plate thickness, given that the best back plate is used.

A similar conclusion is obtained if we compare the different thicknesses of Pb front plates in Fig 4.11. From Table 3.4, the maximum flux of electrons occurs at a depth that is less than 1.10 mm which implies the  $R_{\max}$  in Pb is less than 1.10 mm. We would expect that the range of electrons in Pb is less than in Cu since Pb has a greater physical density or more electrons per unit volume, resulting in a greater number of ionizations per unit volume for the incoming Compton electron which would hence release its energy in a shorter path length. The best MTF is obtained with the Pb(0.39 mm) front plate, and the MTF decreases for front plate thicknesses greater than this value, implying that  $R_{\max}$  for Pb is closer to 0.39 mm. This decrease in MTF for front plates whose thickness is greater than  $R_{\max}$  has not been described by Droege and Bjärngard<sup>7</sup>.

(II) The fact that in Fig. 4.11 the best resolution is obtained with rather than without a front plate, demonstrates that a front plate is needed to shield the film from scatter<sup>7,9-11</sup>.

(III) In Fig. 4.11 we see a crossover effect for detectors with low density front plates (Al, 3.22 mm) or without front plates. This fact is also observed by other authors<sup>7</sup>. For spatial frequencies greater than  $\sim 0.80$  cycle/mm, the MTF of the detector without a front plate outperforms the best detector with a front plate. For spatial frequencies below  $\sim 0.80$  cycle/mm, the MTF of the detector without a front plate is worse than detectors with a Cu(0.95 mm) front plate. Thus, detectors without front plates exhibit better response at high spatial frequencies but poorer response at low spatial frequencies than detectors with front plates thicknesses close to  $R_{\max}$ . This characteristic crossover was detected by Droege and Bjärngard since they used Cu and Pb front plates of thicknesses (0.10 and 0.13 mm, respectively) less than the electrons' range  $R_{\max}$  for the photon energy beam used (8 MV). Thus, the crossover phenomenon appears when comparing MTFs for detectors with thin ( $< R_{\max}$ ) front plates to detectors with thick ( $> R_{\max}$ ) front plates. Moreover, because the crossover phenomenon is not seen with the Cu or Pb front plates of thicknesses 0.95 mm and the 0.39 mm, respectively, these thicknesses are probably close to, but not much smaller than,  $R_{\max}$ .

The MTF response below  $\sim 1$  cycle/mm is very important for perception of low contrast objects and their edges. For these spatial frequencies it appears that the front metal screen is required. At megavoltage energies, structures of clinical interest are usually large

(about 1 cm) whose appearance is better visualized with a front plate. However, thin screens may be more useful in reproducing the edges of these low contrast objects.

(IV) Resolution can be improved by using a high density screen to shorten the electron ranges<sup>7-8,12</sup>, and by using a low atomic number material to reduce electron scattering angle<sup>13</sup>. But, physical density increases as atomic number increases. For the Clinac-18 therapy beam, the Cu front plate gives consistently better MTFs than Pb. This suggests that the decrease in electron scatter due to smaller atomic number of Cu, is more important to resolution than the increase in electron path length that accompanies the lower physical density of Cu. This trend does not seem to extend to much lower atomic number materials such as Al. The 3.22 mm Al front plate gives MTF results which are considerably worse than Cu or Pb. Thus, physical density of material is important. Copper may work best since it has a fairly low atomic number of 27 and a fairly high physical density  $\sim 8.9 \text{ g/cm}^3$ , whereas Pb has both a very high atomic number of 82 and a high physical density of  $11.48 \text{ g/cm}^3$ . Aluminum, on the other hand, has both a very low atomic number of 13 and a low density of  $2.7 \text{ g/cm}^3$ . Copper seems to have the best of both worlds when compared to the other two metals which are at the two extremes. Generally, given best back plates, the Cu front plates perform better than the Pb plates, and the Pb front plates perform better than Al front plates.

(V) With the Clinac-18, in its 10 MV X-ray mode, the best resolution is obtained with the (Cu, 0.95; Al, 3.22), and (Pb, 0.39; Al, 1.62) detectors for frequencies less than 0.7 cycles/mm and with the (without; Al, 1.62) detector for spatial frequencies greater than 0.7 cycles/mm. The worst MTFs are obtained with detectors composed of thick Pb front plates: (Pb, 1.31; without), and (Pb, 2.05; without), and with Cu or Pb back plates.

#### **4.1.2 Cobalt-60: Modulation Transfer Functions**

We will now analyze the data from the Cobalt-60 unit. Once again, for each figure we will compare the detectors by varying the back plate while keeping the front plate fixed. In each figure, we have also included the best Clinac-18 MTF data for the same front plate.

In Fig. 4.12, we compare results for the detectors consisting of a Cu(0.95 mm) front plate in combination with Al(0.60, 1.62, 3.22, and 4.81) mm back plates, and one without a back plate. The best detector appears to be the one with the 1.62 mm thick back plate followed, in order of decreasing performance, by the 3.22 mm, 0.60 mm, 4.81 mm back plates and the detector without a back plate. We also note that the MTF decreases with photon energy and this will be the case for all of the figures in this section.

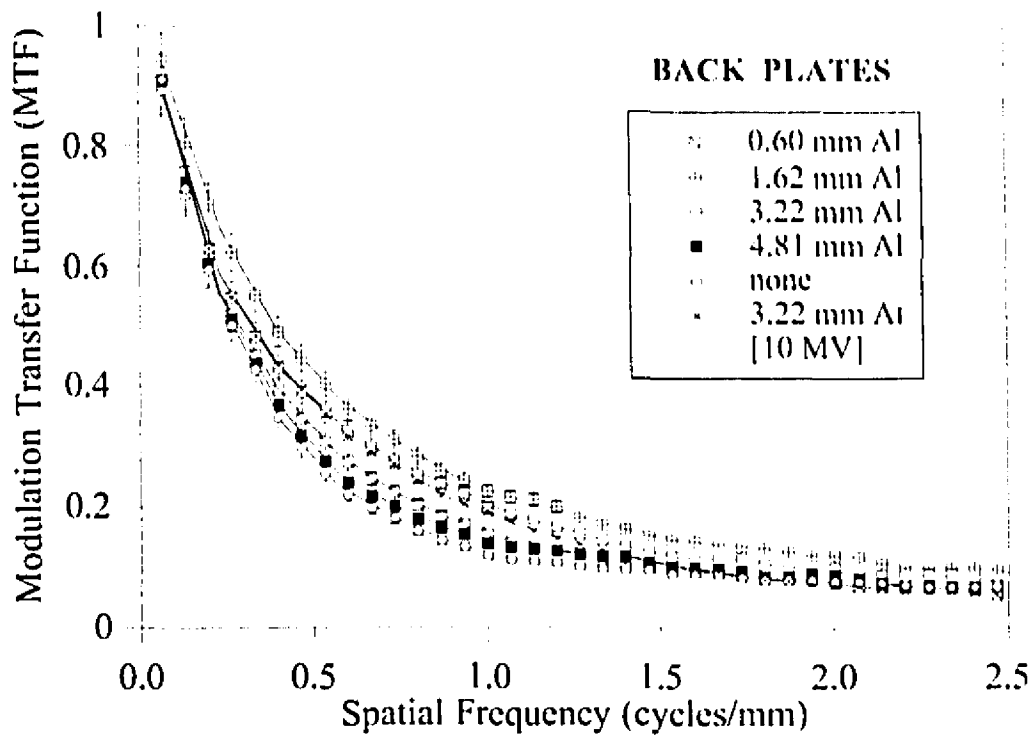


Figure 4.12 MTFs for detectors with Cu(0.95 mm) front plates and with varying thicknesses of Al back plates or without a back plate.

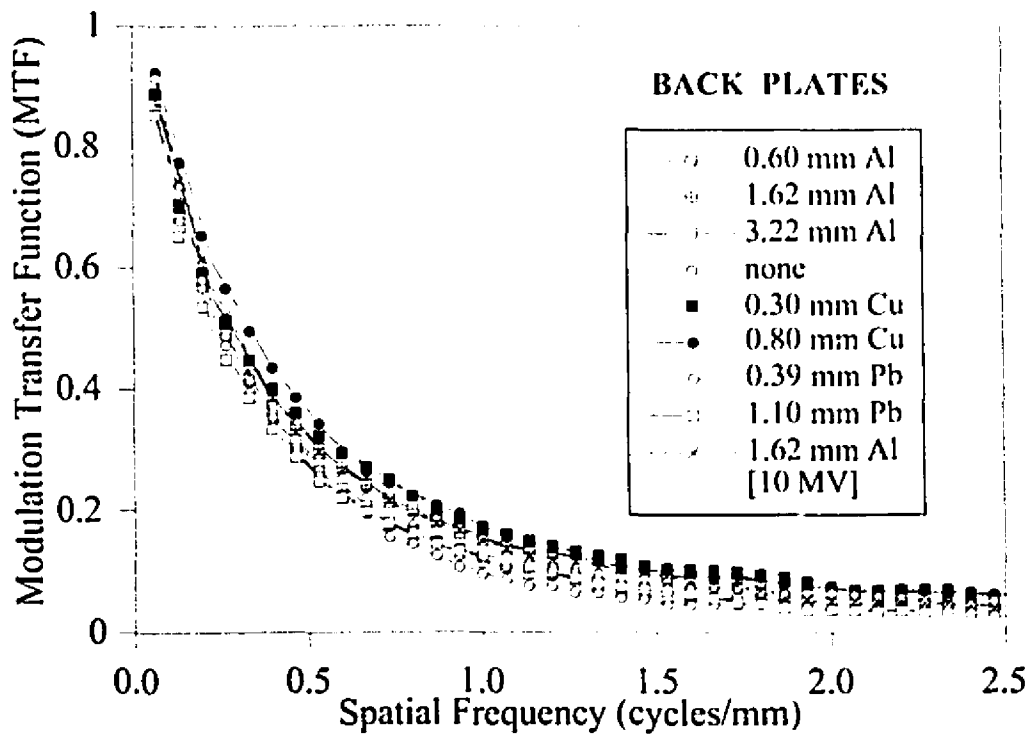
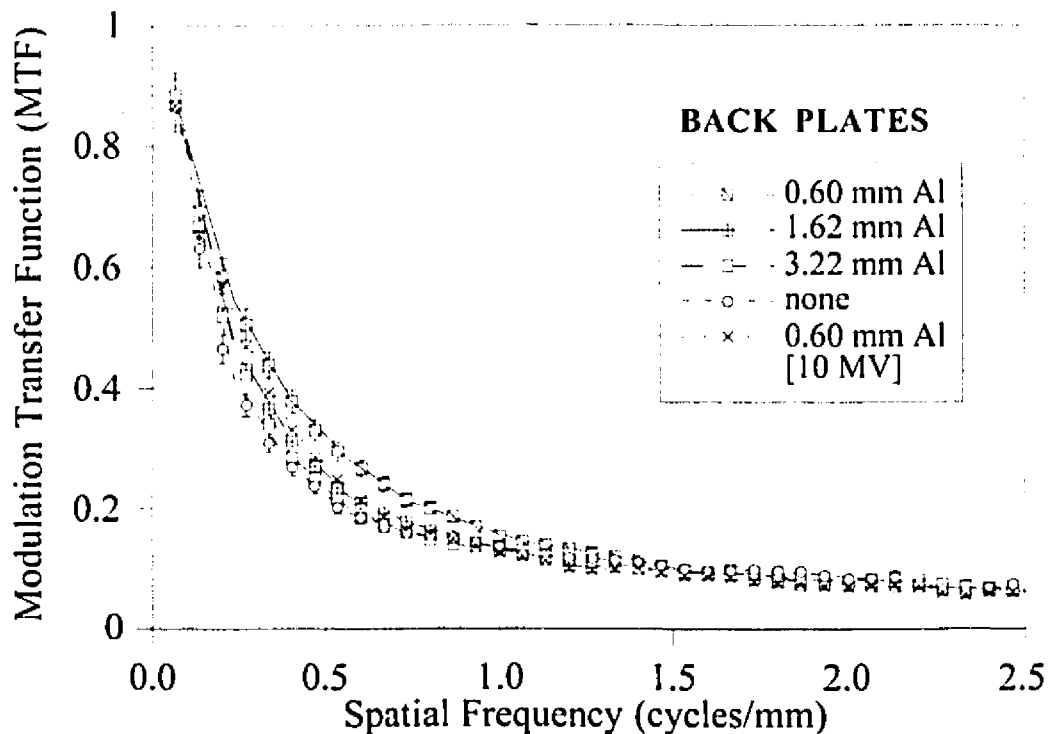


Figure 4.13 MTFs for detectors with Cu(1.75 mm) front plates and with varying thicknesses of Al, Cu, or Pb back plates or without a back plate.

Figure 4.13 shows detectors with Cu(1.75 mm) front plates and with the following back plates: Al(0.60, 1.62, and 3.22 mm), Cu(0.30, and 0.80 mm), Pb(0.39, and 1.10 mm) and without a back plate. For the Al back plates, 1.62 and 0.60 mm thicknesses offer the best MTFs. Detectors with 3.22 mm and without back plates are the worst. But, the best MTF in this figure is obtained with the Cu(0.80 mm) back plate for frequencies greater than 0.7 cycles/mm. Beyond this spatial frequency, the Cu(0.30 mm) plate is as good. The fact that copper is the best back plate would suggest that the room scatter component is more pronounced in the Cobalt-60 room.

In Fig. 4.14, Cu(2.40 mm) front plates are used with the following back plates: Al(0.60, 1.62, and 3.22 mm) and without a back plate. The thinnest (0.60 mm) back plate gives the best MTF, confirming the trend obtained with the Clinac-18 MTF results: as the front plate increases in thickness the thinner Al back plate gives the better resolution.



**Figure 4.14** Modulation Transfer Functions for detectors with Cu(2.40 mm) front plates and with varying thicknesses of Al back plates or without a back plate.

The Pb(0.39 mm) front plate in Fig. 4.15 is in combination with Al(1.62 mm) and without a back plate. The Al back plate gives better results up to approximately 1.20 cycle/mm but beyond this frequency, the detector without back plate is best. With the Pb(1.10 mm) front plate in Fig. 4.16, we find that MTF curves are clustered together for the Al back plates. The best MTF curve corresponds to the detector without a back plate.

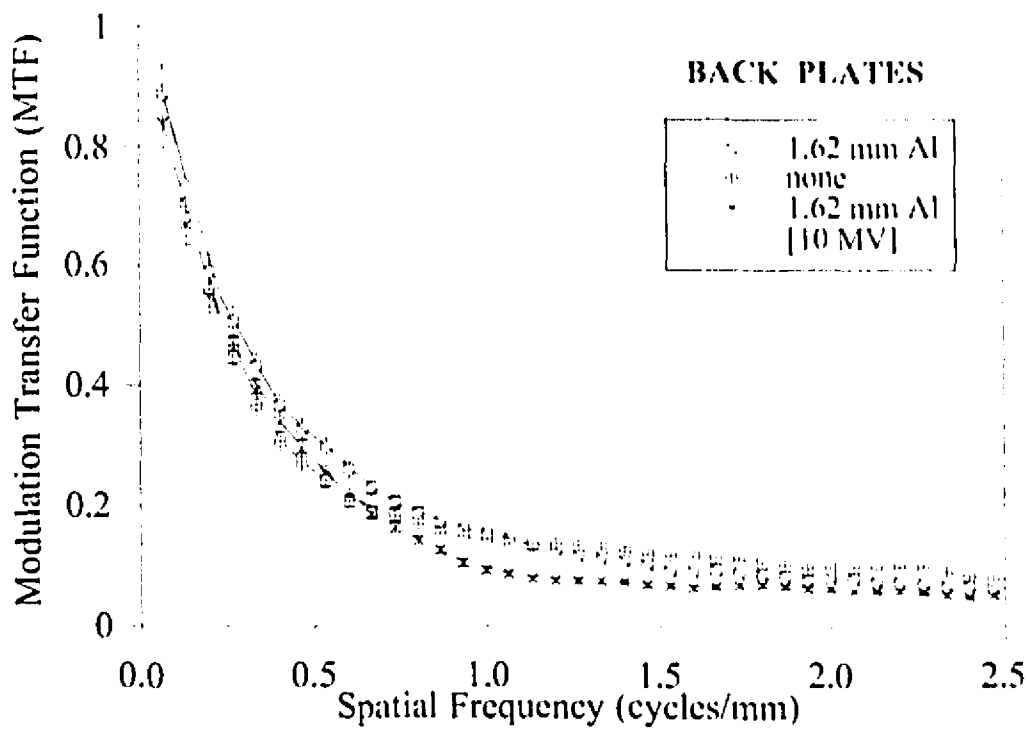


Figure 4.15 Modulation Transfer Functions for detectors with Pb(0.39 mm) front plates and with varying thicknesses of Al back plates without back plate.

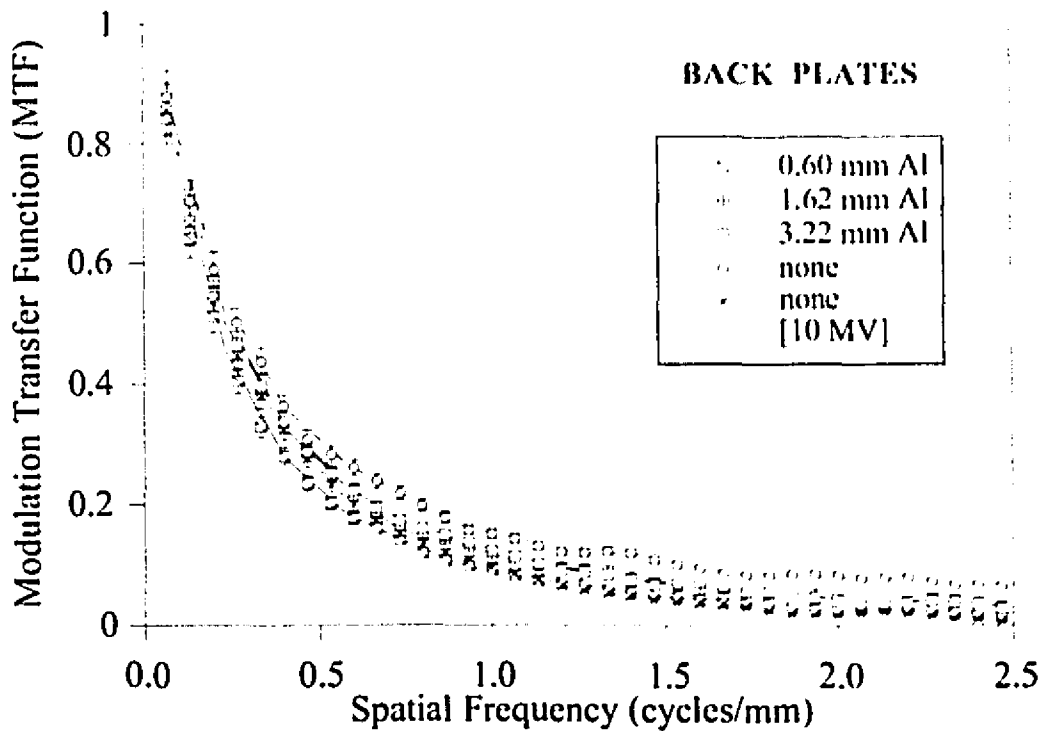
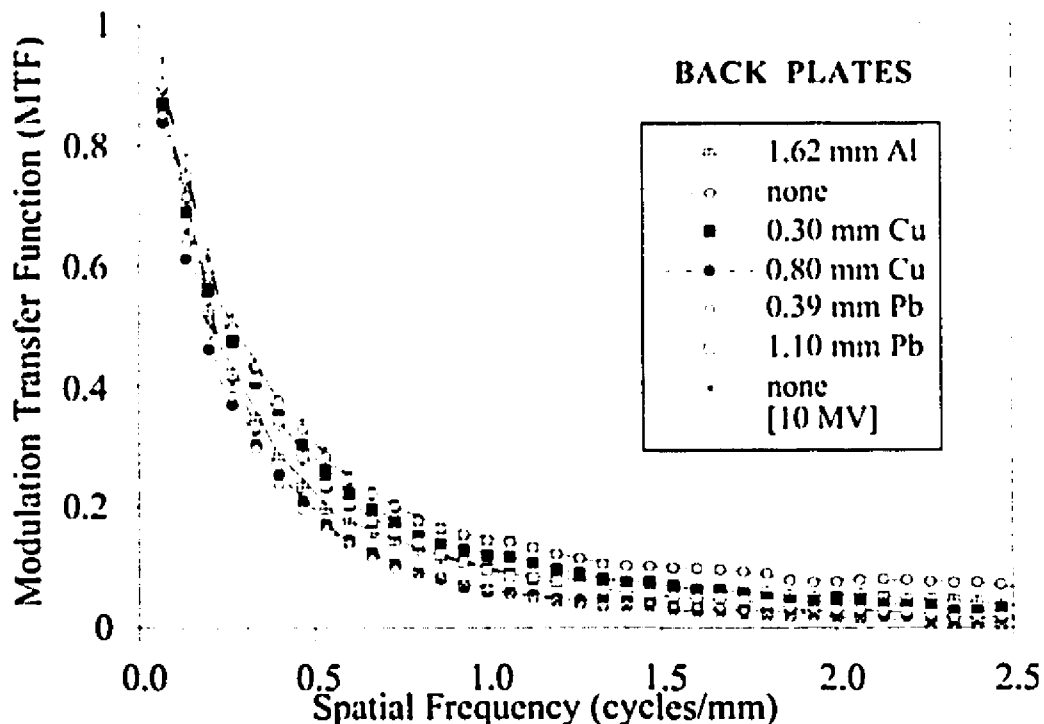


Figure 4.16 Modulation Transfer Functions for detectors with Pb(1.10 mm) front plates and with varying thicknesses of Al back plates or without a back plate.

In Fig. 4.17 we show MTFs for detectors with Pb(1.31 mm) front plates and with the following back plates: Al(1.62 mm), Cu(0.30 and 0.80 mm), Pb(0.40 and 1.10 mm) and without a back plate. The detector without the back plate performs best. In Fig. 4.18 we compare detectors with Pb(2.05 mm) front plates and an Al(1.62 mm) back plate and without a back plate. The best MTF is obtained for the detector without a back plate.

The brass front plate is analyzed in Fig. 4.19 with the following back plates: Al(0.60, 1.62, and 3.22 mm), Cu(0.30 and 0.80 mm), Pb(0.39 and 1.10 mm), and also without a back plate. The best results are obtained with the Al(0.60 mm) or the Al(3.22 mm) back plates. When the detector without a back plate is used very poor results are obtained.



**Figure 4.17** Modulation Transfer Functions for detectors with Pb(1.31 mm) front plates and with varying Al, Cu, or Pb back plates or without a back plate.

In Fig. 4.20, we have MTFs of detectors with Al(3.22 mm) front plates combined with varied back plates: Cu(0.30 and 0.80 mm) and Pb(0.40 and 1.10 mm). The best resolution is obtained with the Pb(1.10 mm) back plate which performs slightly better than the rest. For this same front plate with the Clinac-18, the back plate which gave the best MTF was the Cu(0.8 mm) front plate. This suggests that the Cobalt-60 unit is characterized by a greater ratio of room to back scatter photons than is the Clinac-18.

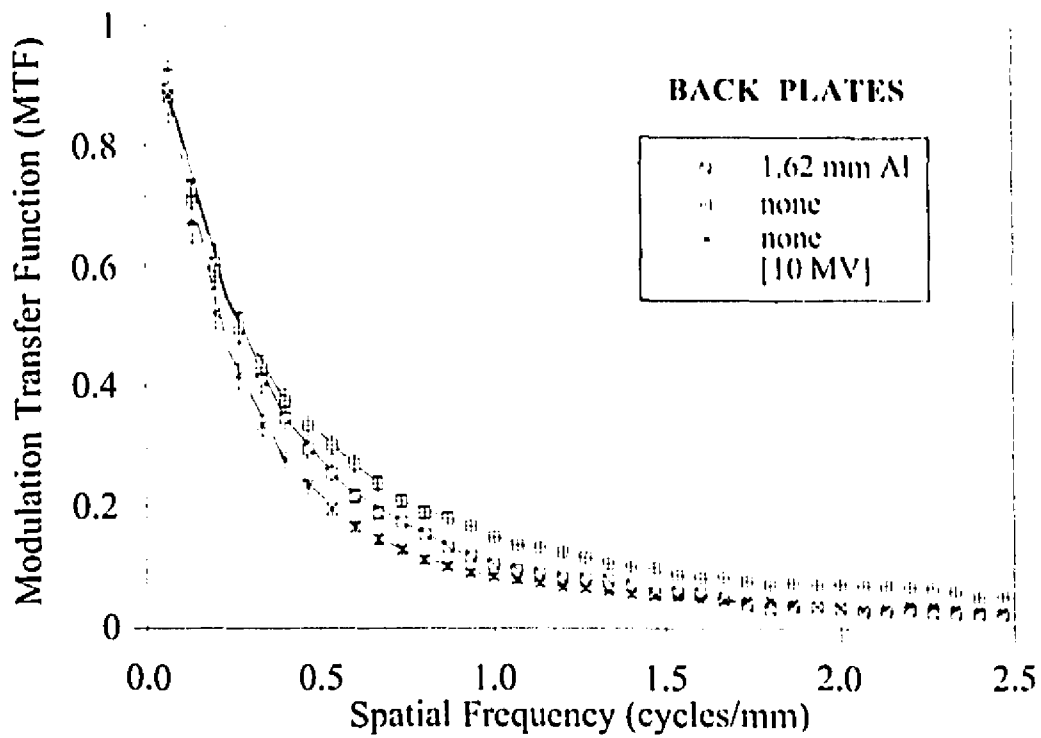


**Figure 4.18** Modulation Transfer Functions for detectors with Pb(2.05 mm) front plates and with Al back plates or without a back plate.

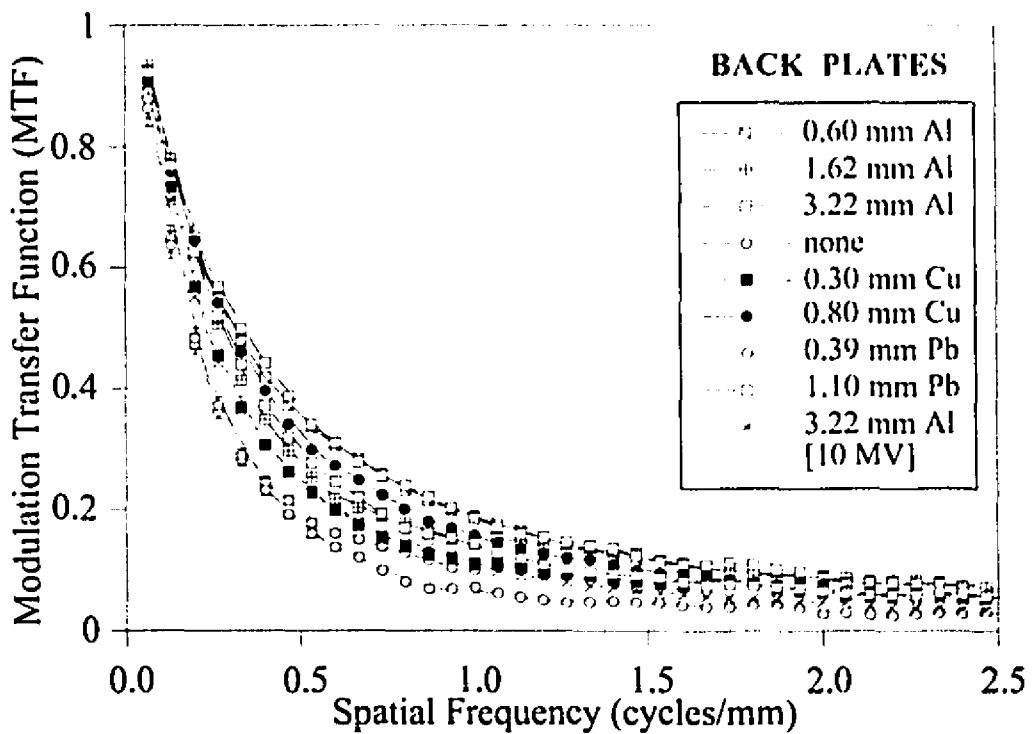


**Figure 4.19** MTFs for detectors with brass(3.07 mm) front plates and with varying thicknesses of Al, Cu, or Pb back plates or without back plates.

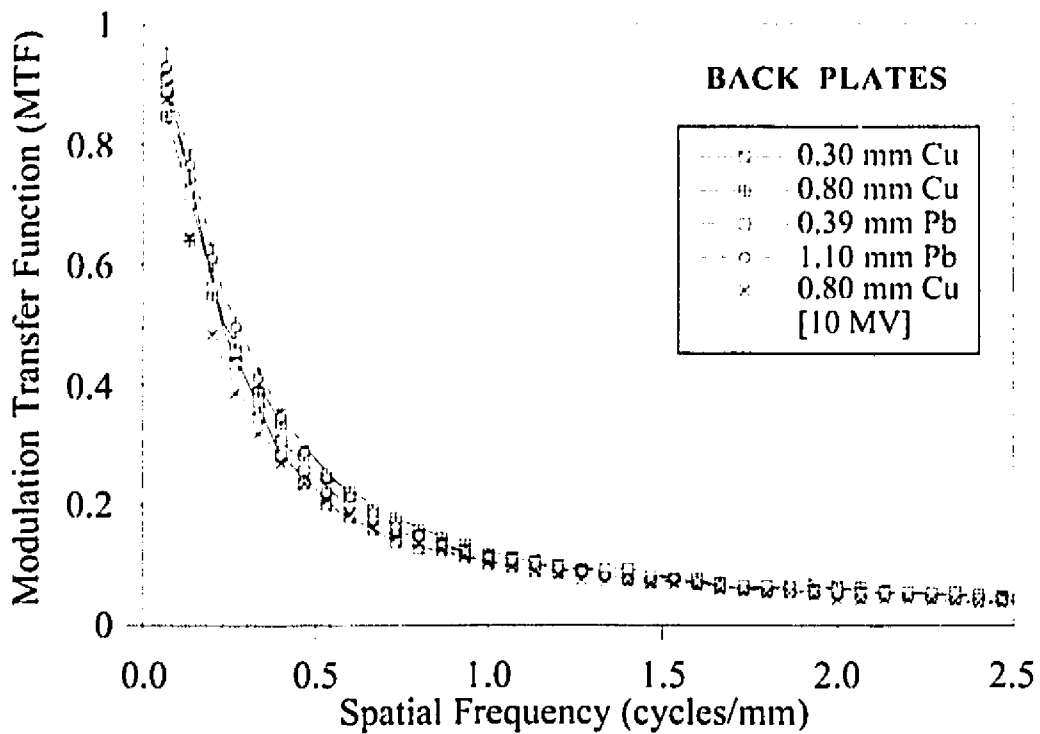


Figure 4.20 Modulation Transfer Functions for detectors with Al(3.22 mm) front plates and with varying thicknesses of Cu, or Pb back plates.

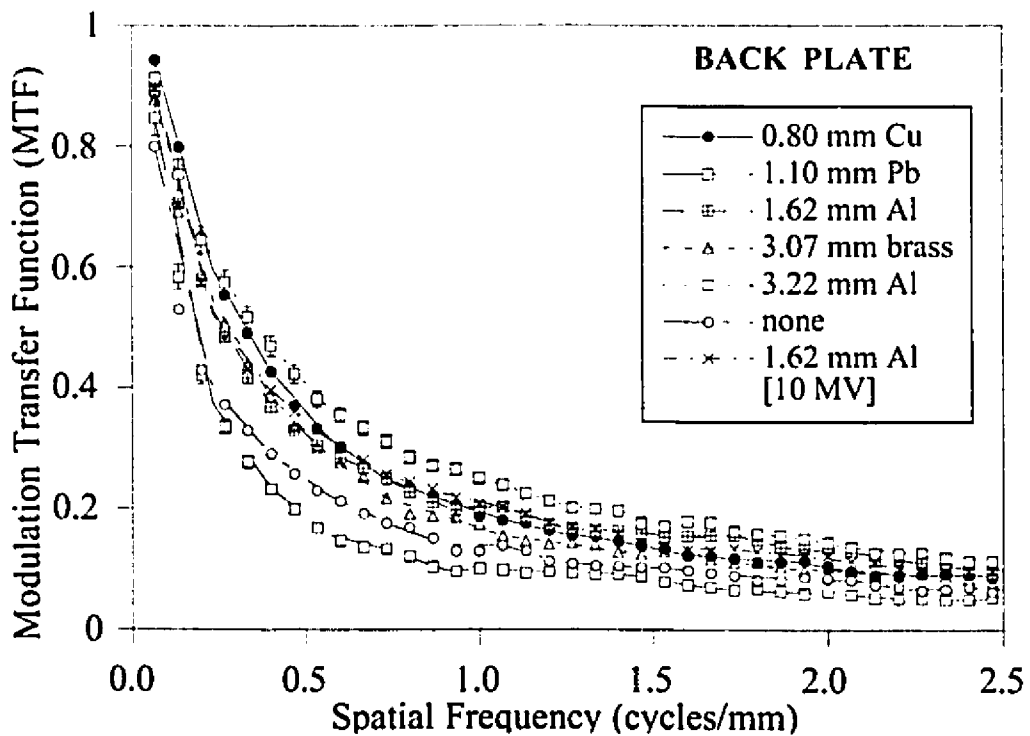


Figure 4.21 MTFs for detectors without front plates and with varying thicknesses of Al, Cu, Pb, or brass back plates or without a back plate.

In Fig. 4.21 we show MTFs for detectors without front plates and different back plates: Cu(0.80 mm), Pb(1.10 mm), Al(1.62 and 3.22 mm), brass(3.07 mm), and (without). The best MTF results in this case are obtained with the Al(3.22 mm) back plate. The best results for Clinac-18 are obtained with the Al(1.62 mm) back plate. Below 0.30 cycles/mm the best results are obtained with the (Cu, 0.8 mm) back plate. As was discussed with the Clinac-18 data, a thin, low atomic number, low density back plate is recommended even though it contributes a low backscatter component.

#### 4.1.2.1 Comparing front plates using the Cobalt-60 beam

In Fig. 4.22, we summarize the best MTFs obtained from each of Figs. 4.12 to 4.21. The ten best detectors are: (Cu, 0.95; Al, 1.62), (Cu, 1.75; Cu, 0.80), (Cu, 2.40; Al, 0.60), (Pb, 0.39; Al, 1.62), (Pb, 1.10; without), (Pb, 1.31; without), (Pb, 2.05; without), (brass, 3.07; Al, 3.22), (Al, 3.22; Pb, 1.10), and (without; Al, 3.22). The most striking difference between the detectors in Figs. 4.11 and Fig. 4.22 is that the back plates are thicker and denser on average in Fig. 4.22. The fact that the Cobalt-60 machine requires thicker, and denser back plates suggests that room scatter in the Cobalt-60 room is greater than within the Clinac-18 room. This may come from the fact that the Cobalt-60 room is smaller. Again we notice that as the front plate thickness increases the best MTF is obtained with a thinner back plate.

The MTFs obtained with the Clinac-18 seem to be consistently worse than that obtained with the Cobalt-60 machine. This fact was noted by others<sup>2,7-8</sup>. The average difference between the MTFs of the therapy machines for given detectors at 1 cycle/mm, is about 22 %. This is because  $R_{\max}$  for Cobalt-60 machine is smaller than for Clinac-18 (0.5 cm and 2.5 cm, respectively, in water). Smaller  $R_{\max}$  means that we have less lateral scatter and hence better resolution. The maximum range of the electrons  $R_{\max}$  at therapy energies is thus a vital parameter. Because  $R_{\max}$  is energy dependent, the MTF is also energy dependent. The MTFs worsen for detectors whose thicknesses of Cu and Pb plates are greater than 0.95 mm and 0.39 mm, respectively, due to the larger photon scatter and Bremsstrahlung components generated in the front plates with increased thickness. We would expect this since the range of electrons from the Cobalt unit is less than that of the Clinac-18. The crossover effect is also seen for the Cobalt-60 irradiations. The crossover occurs at approximately 0.6 cycle/mm where, the detector without a front plate gives the best MTF beyond this spatial frequency. Detector (Cu, 0.95; Al, 1.62) gives the best resolution for spatial frequencies less than 0.6 cycles/mm and the (without; Al, 3.22)

detector is best for spatial frequency greater than this value. The Cu and brass front plates slightly outperform the Pb front plates while the Al front plate is by far the worst.

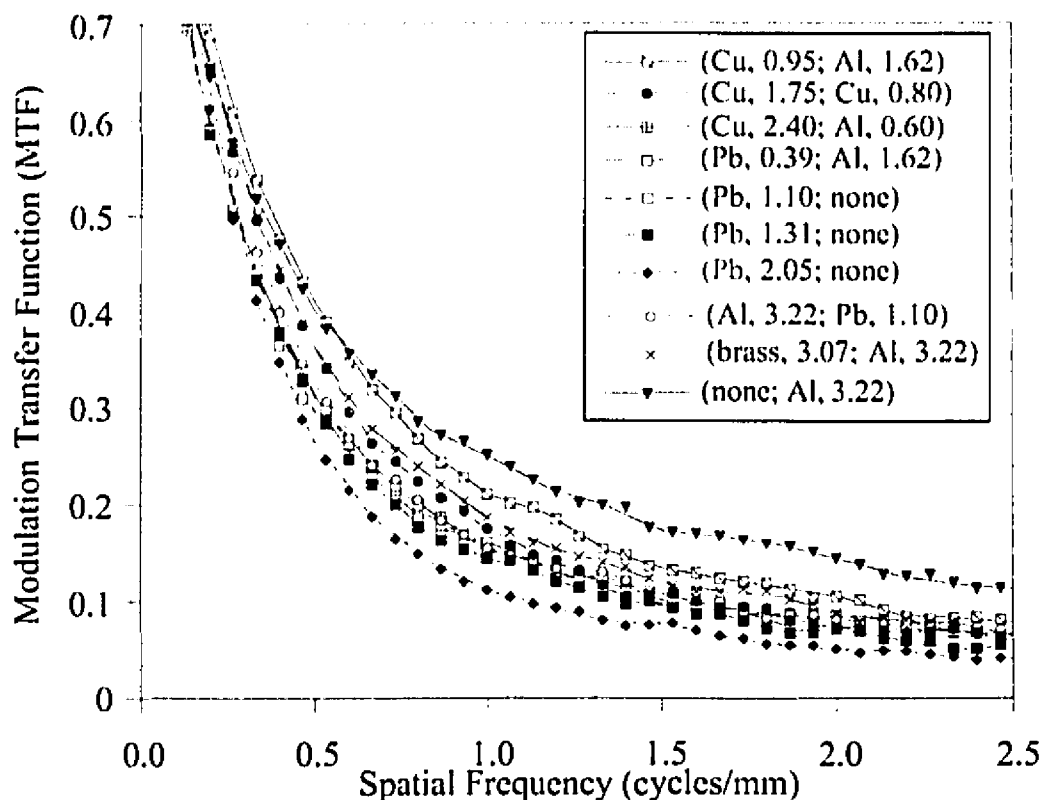


Figure 4.22 Modulation Transfer Functions for the best detectors from each of the last ten figures (i.e., 4.12 to 4.21).

## 4.2 Noise Power Spectrum

In addition to the MTF, the NPS must also be considered.

For the purpose of intercomparison, all of the noise power spectra results in this section were obtained from films that were irradiated to an optical density of  $1.00 \pm 0.02$  for each detector. Due to the time constraints placed on the use of the microdensitometer only seventeen of the forty-nine detectors used in section 4.1 are analyzed in this section. Thus the DQE will also only be calculated for these seventeen detectors since both the NPS and MTF results are required to calculate the DQE. The list of the seventeen detectors that are analyzed for both therapy machines is shown in Table 3.2.

Figures 4.23 to 4.32 show the results for the estimates of the NPS of the detectors. The first five figures show the results for the data obtained using Clinac-18, and the subsequent five figures describe the results obtained when the detectors are irradiated with the Cobalt-60 source. The results are shown on log-log plots so that the differences between the curves can be shown readily. The uncertainties on the spectral values are calculated in accordance to sections 3.2.2.2 and 3.2.2.3 and are approximately 4 % throughout the spatial frequency range of interest. The systematic errors in the spectral values arise from two sources: low-frequency smoothing of the data, and the use of a finite frequency bandwidth (or bias error)<sup>14</sup> resulting from the averaging of 33 adjacent frequency bins. Nishikawa and Yaffe<sup>14</sup> used white noise data from a random number generator to estimate the systematic errors introduced by low-frequency smoothing and found a maximum inaccuracy of 0.5% at all spatial frequencies except at the lowest spatial frequency bin where it was about 10 % lower. They estimated an overall bias error of about 3 % and 1 % for spatial frequencies below and above 1 cycle/mm, respectively. Thus, considering both random and systematic errors, a 14 % error is expected for the lowest frequency, 7-8 % error for all other frequencies below 1 cycle/mm, and 5-6 % error for frequencies greater than 1 cycle/mm.

#### **4.2.1 Clinac-18: Noise Power Spectra**

In Fig. 4.23 we compare the NPS for the detectors with the same back plate Al(1.62 mm) and with varying front plates: Cu(0.95, 1.75, and 2.40 mm), Pb(1.10, 1.31, and 2.05 mm), brass(3.07 mm), and without a front plate. No perceivable trend can be seen for the rise or fall of the NPS with thickness or density of the front plates. For spatial frequencies greater than about 3 cycles/mm, the curves superimpose and no real difference can be given to their NPS.

In Fig. 4.24, the front plate is fixed as Cu(1.75 mm) and the back plates vary as follows: Pb(1.10 mm), Cu(0.80 mm), Al(3.22 and 1.62 mm), and (without). Once again no real trend is evident from the data. The data for the (Cu, 1.75; Al, 1.62) detector are plotted in both Figs. 4.23 and 4.24. Using this curve as our point of reference we can clearly see that the NPS values in both Figs. 4.23 and 4.24 are in the same order of magnitude.

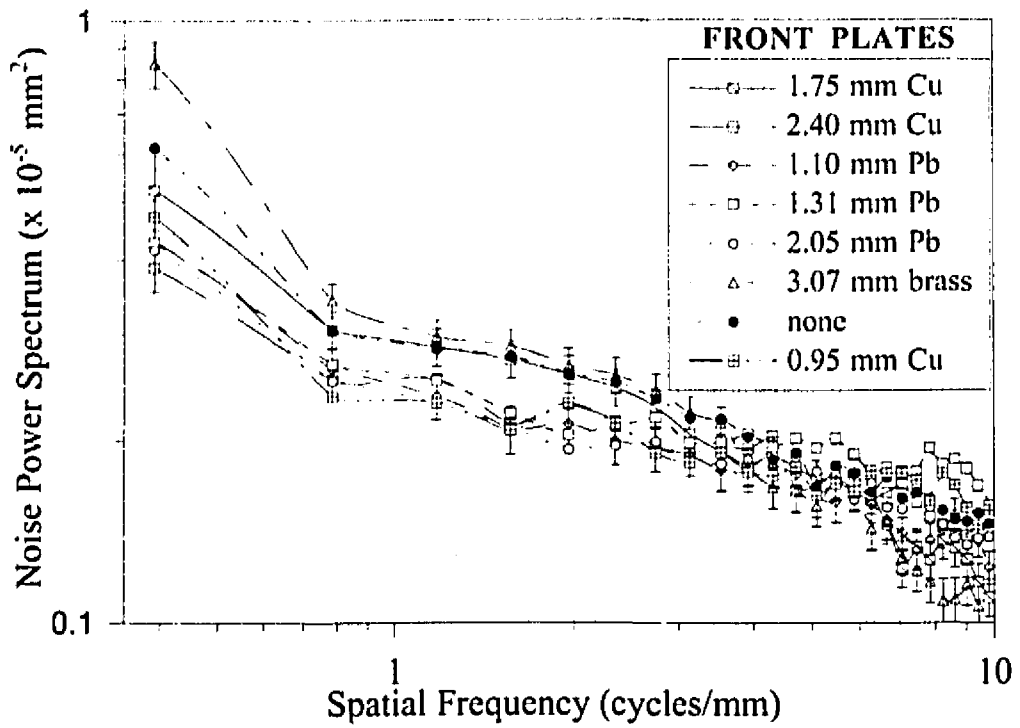


Figure 4.23 Noise Power Spectra for detectors with Al(1.62 mm) back plates and varying thicknesses of Cu, Pb, or brass front plates or without a front plate.

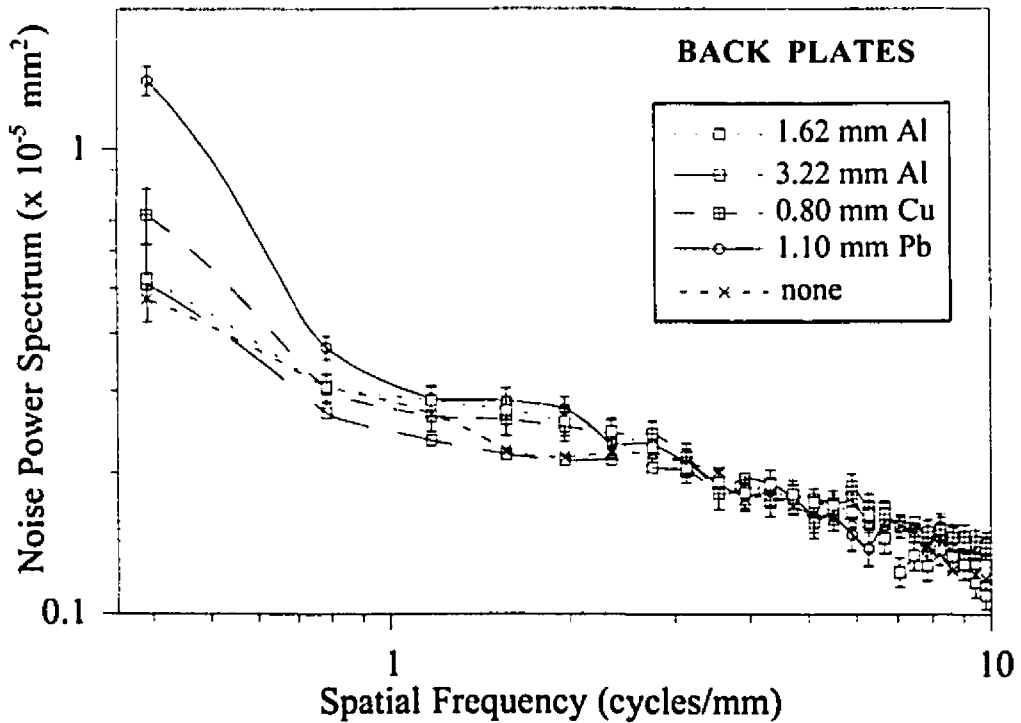
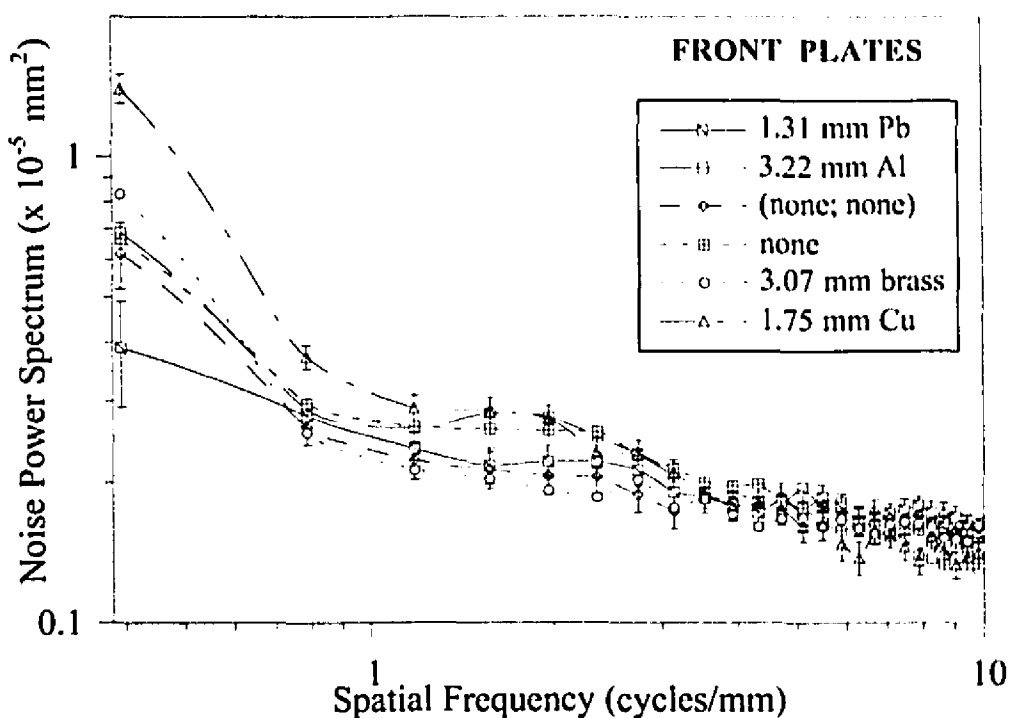


Figure 4.24 Noise Power Spectra for detectors with Cu(1.75 mm) front plates and varying thicknesses of Al, Cu, or Pb back plates or without a back plate.

In Fig. 4.25, we show the results of the NPS for detectors with the same Pb(1.10 mm) back plate and with varying front plates: Pb(1.35 mm), Al(3.22 mm), brass(3.05 mm), Cu(1.75 mm), and without a front plate. Also data for a detector with only film (i.e., without front or back plates) is shown. There seems to be no visible trend in the NPS values with physical density or atomic number. Beyond 3 cycles/mm the curves coincide within error. The (Cu, 1.75; Pb, 1.10) detector is plotted in both Figs. 4.24 and 4.25 which shows that once again the data for all of the NPS are of the same order of magnitude. Two trends are evident from Figs. 4.23 to 4.25: The NPS are fairly independent of the front and back plate combinations used, and that the NPS decreases with spatial frequency. These trends are addressed in the next two paragraphs.



**Figure 4.25** *Noise Power Spectra for detectors with Pb(1.10 mm) back plates and varying thicknesses of Al, Cu, Pb, or brass front plates or without a front plate. Also shown is the NPS for the film without metal-plates.*

Figures 4.23 to 4.25 imply that the NPS is independent of the type of front and back plates used. As is discussed in section 2.1.4.3, the contribution to the total NPS originates mainly from two components: quantum and film noise. From Table 3.4 we know that in Fig. 4.23, 6-7 times more photons/mm<sup>2</sup> are required to expose the (without; Al, 1.62) detector as compared to the (Pb, 2.05; Al, 1.62) detector. Thus, we would expect that the quantum noise power, which is inversely proportional to the quanta

used in the exposure, should differ by a factor of  $\sim 7$ . Yet, throughout Figs. 4.23 to 4.25 we see that increasing the quantum noise power has no effect whatsoever on the total noise power spectra, thus implying that the film noise power dominates<sup>2,14</sup>. Thus for an exposure of 1.00 D the quantum flux is high enough for quantum fluctuation to be minimal<sup>15</sup>. Therefore, the film grain noise is the dominant factor in our NPS.

The trend for all of the data is similar: the NPS decreases with increased spatial frequency, and levels off at frequencies exceeding approximately 7 cycles/mm. This trend is well documented in literature concerned with high energy (X-ray) photon NPS<sup>2,16-19</sup>. This trend is not seen for films exposed to light where the spectrum is white<sup>2,17-18</sup>. The basic imaging elements for film are the individual silver grains in the emulsion layer when the film is exposed to light. Yet, when the film is exposed to X-rays the basic imaging elements are larger than one grain in this instance since several grain crystals are developed by one quanta<sup>17,20</sup>. Hence, for Figs. 4.23-4.25, as Frieser states<sup>17</sup> "the individual silver grain is no longer the basic imaging element in this instance, but rather aggregates of silver grains which are formed by the incident X-ray quanta. At high frequencies ... the fluctuations are caused by the individual silver grains [whereas] the aggregates affect the measurements only at the low frequencies" where we are concerned with good correlation of large structures in the image.

In Fig. 4.26, we compare the NPS for one detector (without; Pb, 1.10 mm) but with different uniform optical densities on the film: 1.00, 0.69, and 0.52 D. Clearly, the NPS increases with optical density and is proportional to the optical density. This result has been confirmed experimental and theoretically by others<sup>17,21-24</sup> demonstrating the importance of using the same film optical density among investigators in evaluating NPS. Moreover, Fig. 4.27 shows the plot of optical density versus NPS at four spatial frequencies values: 0.39, 1.57, 3.92, and 8.23 cycles/mm. At larger spatial frequencies the relationship appears linear, while at small spatial frequencies the relationship appears to saturate with increased optical density. At small spatial frequencies, the contribution to the noise power spectrum comes mainly from larger structures or aggregates of many developed film grains generated by the high energy photon exposures. This is evident from the fact that the NPS values are 3 to 5 times greater at small than at large spatial frequencies. At small spatial frequencies (large scales) the NPS tends towards saturation with increased exposure, suggesting that the number of aggregates of film grains is increasing and they are more effectively covering the film area.

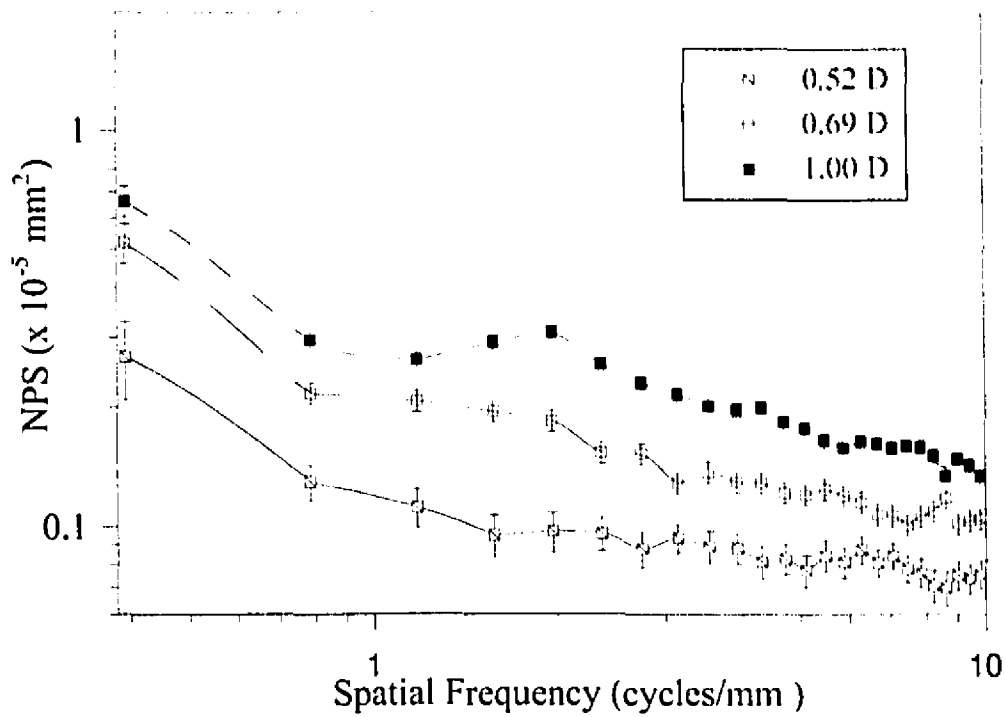


Figure 4.26 Noise Power Spectra for the (none; Ph, 1.10) detector where the nominally uniform film densities used were 1.00, 0.69, and 0.52 optical density.

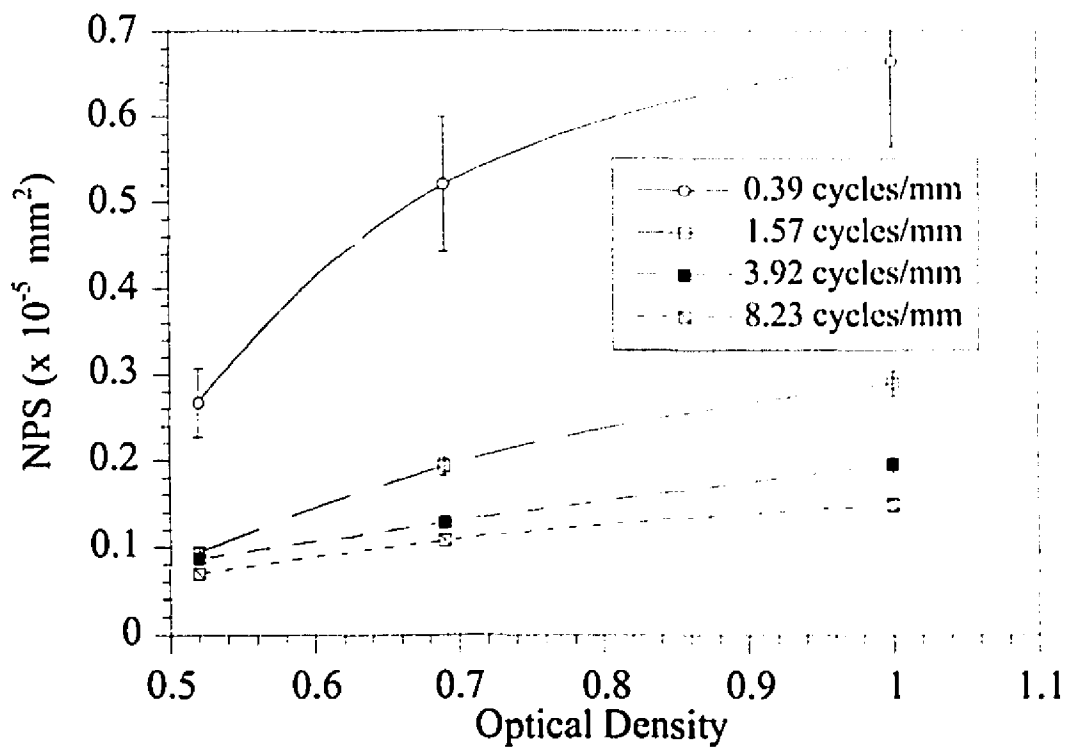
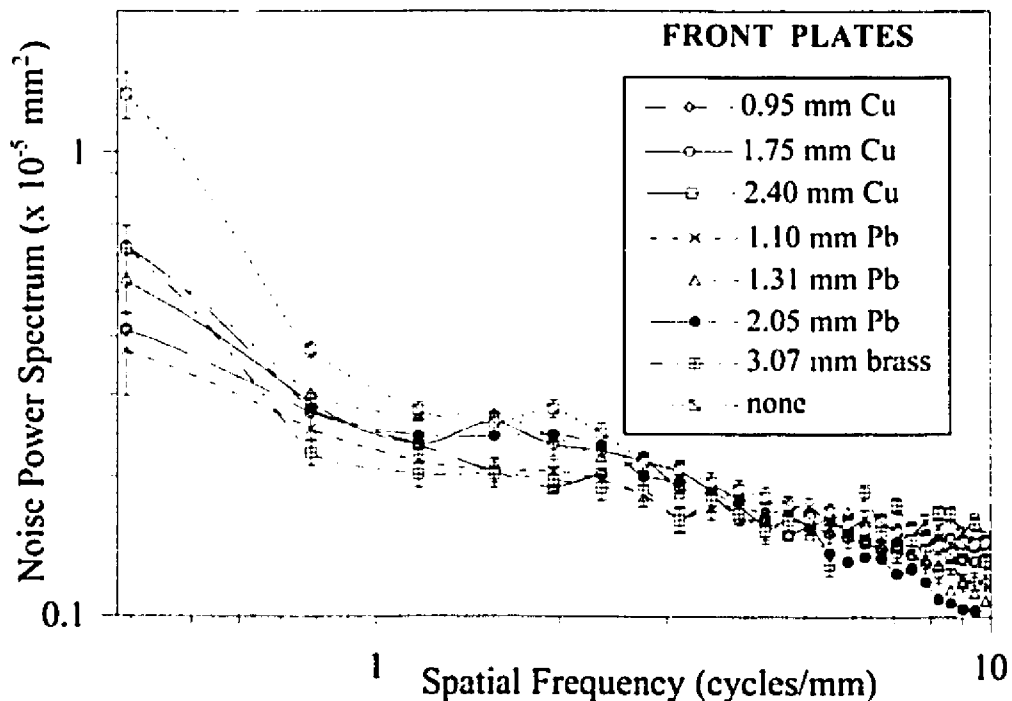


Figure 4.27 Optical density versus NPS at four spatial frequencies values: 0.39, 1.57, 3.92, and 8.23 cycles/mm.

#### 4.2.2 Cobalt-60: Noise Power Spectra

In Fig. 4.28 we compare the NPS for the detectors with the same back plate (Al, 1.62 mm) and varying front plates: Cu(0.95, 1.75, and 2.40 mm), Pb(1.10, 1.31, and 2.05 mm), brass(3.07 mm), and without a front plate. No discernible trend seems to exist between the NPS values and the physical characteristics of the plates. Also, no real difference exists between the NPS values for the Clinac-18 and Cobalt-60 machines. In Fig. 4.29, the front plate is fixed at Cu(1.75 mm) and the back plates vary as follows: Pb(1.10 mm), Cu(0.80 mm), Al(3.22 and 1.62 mm), and (without). From Figs. 4.28 and 4.29 the NPS values are comparable. Figure 4.30 shows the NPS for detectors with the same Pb(1.10 mm) back plates and with varying front plates: Pb(1.35 mm), Al(3.22 mm), brass(3.05 mm), Cu(1.75 mm), and without a front plate. Also data for a detector with only film (i.e., without front or back plate) is shown. Figures 4.28 to 4.30 show the same trends as for the Clinac-18 generated NPS: The NPS decrease with spatial frequency, and the NPS originates mainly from film noise (granularity) contributions.



**Figure 4.28** Noise Power Spectra for detectors with Al(1.62 mm) back plates and varying thicknesses of Cu, Pb, or brass front plates or without a front plate.

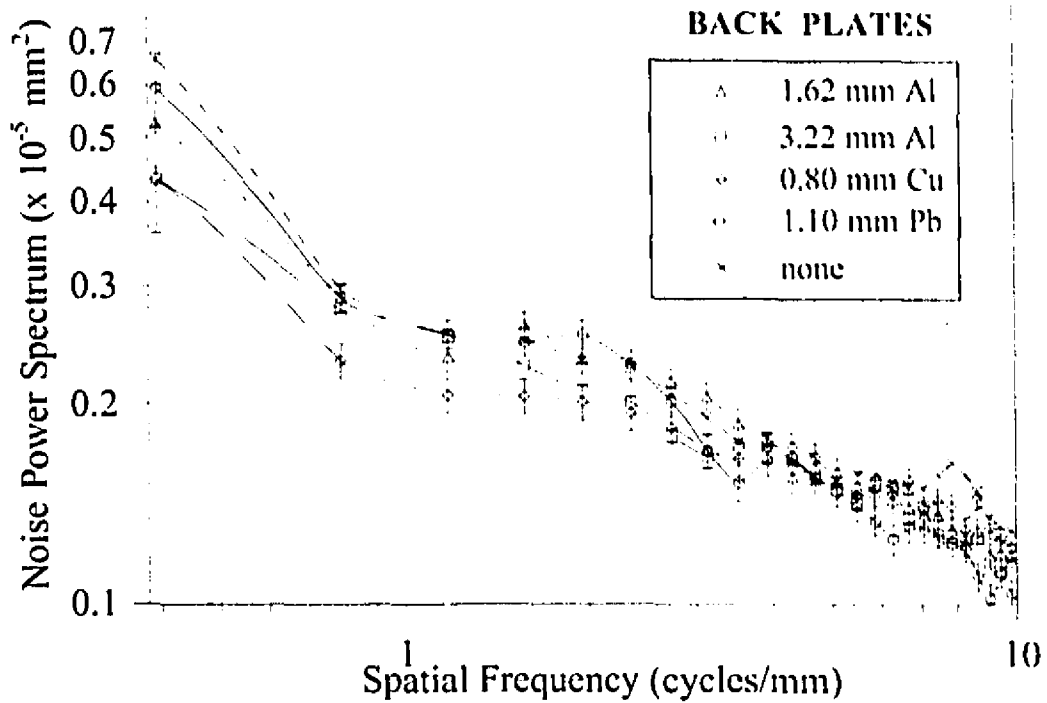


**Figure 4.29** Noise Power Spectra for detectors with Cu(1.75 mm) front plates and varying thicknesses of Al, Cu, or Pb back plates or without a back plate.

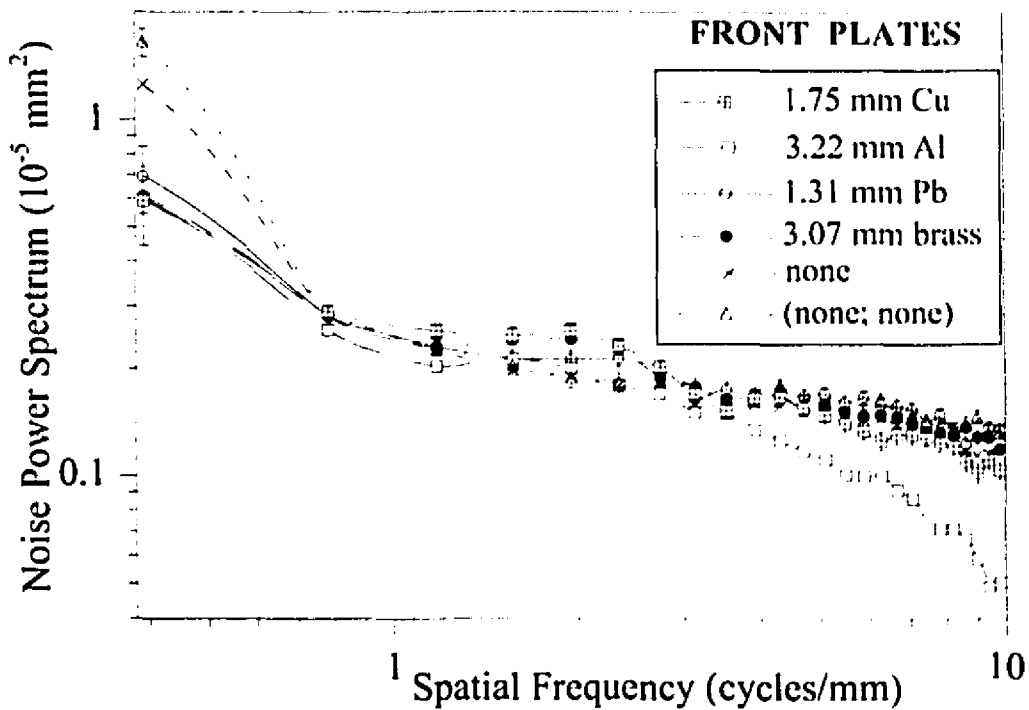


**Figure 4.30** Noise Power Spectra for detectors with Pb(1.10 mm) back plates and varying thicknesses of Al, Cu, Pb, or brass front plates or without a front plate. Also shown is the NPS for film without metal-plates.

In Fig. 4.31, we have the NPS for the same detector (none; Pb, 1.10 mm) but for different film optical densities: 1.00, 1.27, and 1.81. For spatial frequencies greater than 1 cycle/mm the NPS increases with optical density as it did in Fig. 4.26. At approximately 1 cycle/mm, a crossover occurs for the NPS values corresponding to 1.27 and 1.81 D. In Fig. 4.32 we show the change in NPS with film optical density for four spatial frequencies: 0.39, 1.57, 3.92, and 8.23 cycle/mm. From Fig. 4.32, we see that at the lowest spatial frequency of 0.39 cycle/mm we have a maximum NPS value of  $\sim 3.8 \times 10^{-5} \text{ mm}^2$  occurring at  $\sim 1.3 \text{ D}$ . Thus, an increase in the film exposure beyond  $\sim 1.3 \text{ D}$  will result in a decrease in the NPS which suggests that the variance over large scales decreases with increased exposure and implies a formation of a large number of film grain aggregates covering the image area more uniformly (i.e., less fluctuations). This dependence between NPS and optical density at low spatial frequencies has not been shown in the literature.

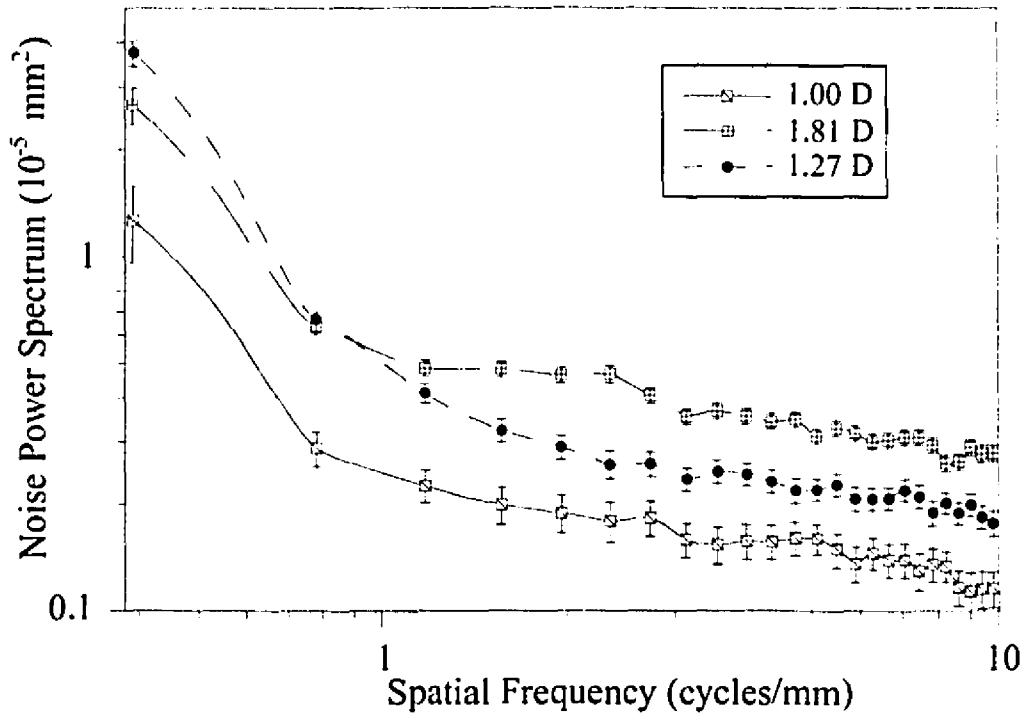


**Figure 4.31** *Noise Power Spectra for the (none; Pb, 1.10) detector where the nominally, uniform film densities used were 1.00, 1.27, and 1.81 optical density.*

Figures 4.23 to 4.25, and 4.28 to 4.30 show that the NPS estimates (at 1.00 D) tend towards a constant lowest value of  $0.15 \times 10^{-5} \text{ mm}^2$  at spatial frequencies greater than  $\sim 7 \text{ cycle/mm}$  which corresponds to the variance due to the single silver grains. This suggests that the size of the film grain aggregates is approximately  $140 \mu\text{m}$ .

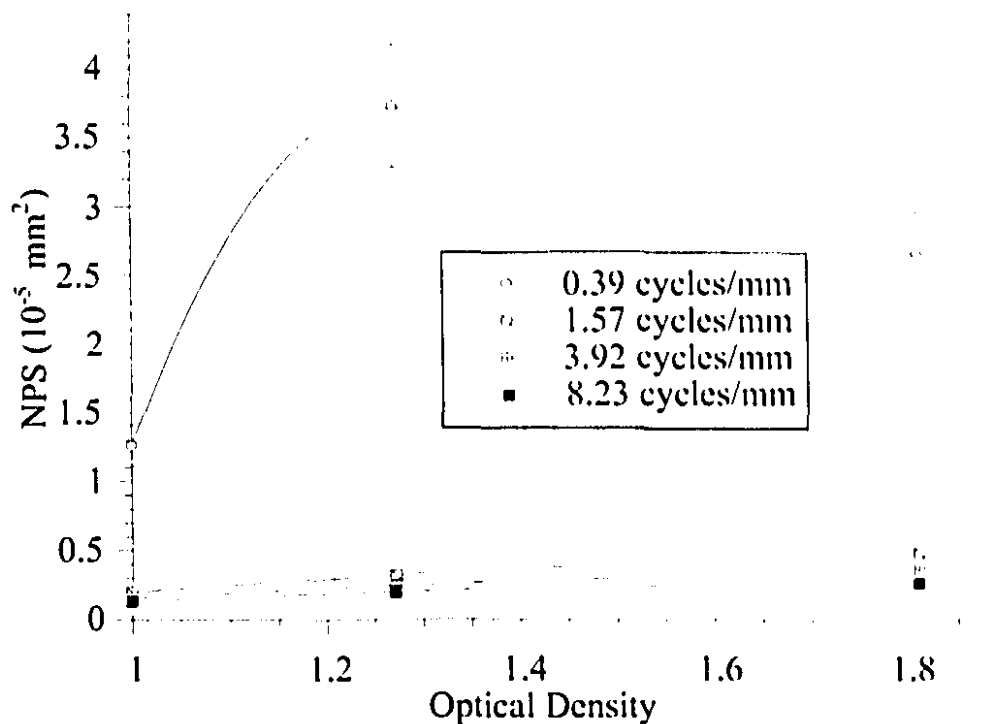


**Figure 4.32** *Noise Power Spectrum versus film optical density for four spatial frequencies: 0.39, 1.57, 3.92, and 8.23 cycle/mm*

### 4.3 Detective Quantum Efficiency

#### 4.3.1 Clinac-18: Detective Quantum Efficiency

The DQE measurements from the Clinac-18 are shown in Figs. 4.33 to 4.35. Most of the DQEs have the same shape: smoothly decreasing with increased spatial frequency. For spatial frequencies greater than 3 cycles/mm, the DQEs for all of the detectors are essentially zero. The only detector that deviates slightly from this general shape is the detector without front and back plate. The curve for this detector is constant between 0.4 and 0.8 cycle/mm (Fig. 4.35).

In Fig. 4.33 the detectors consist of Al(0.62 mm) back plates and front plates of varying thicknesses: Cu(0.95, 1.75, and 2.40 mm), Pb(1.10, 1.31, and 2.05 mm), brass(3.07 mm), and without a front plate. The (Cu, 1.75; Al, 1.62) detector has the best DQE. The next best DQE is obtained by the detector with the Cu(2.40 mm) front plate, followed by the detector with the Cu(0.95 mm) front plate. The best detectors appear to have Cu front plates. The next best series of curves belong to the Pb front plates of

thicknesses 1.10 mm, and 1.31 mm. The 2.05 mm-thick lead front plate gives the worst results. This is because the thickness is much greater than the average range of the electrons in Pb. The large thickness not only contributes (1) a larger photon scatter component to the film, but it also (2) attenuates the beam reducing the electron flux impinging on the film thus degrading the image by reducing the signal. Furthermore, detectors without front plates also result in very poor DQEs because, (1) a small number of quanta from the information source are gathered, and (2) the film is not being shielded from scatter contamination from the patient.

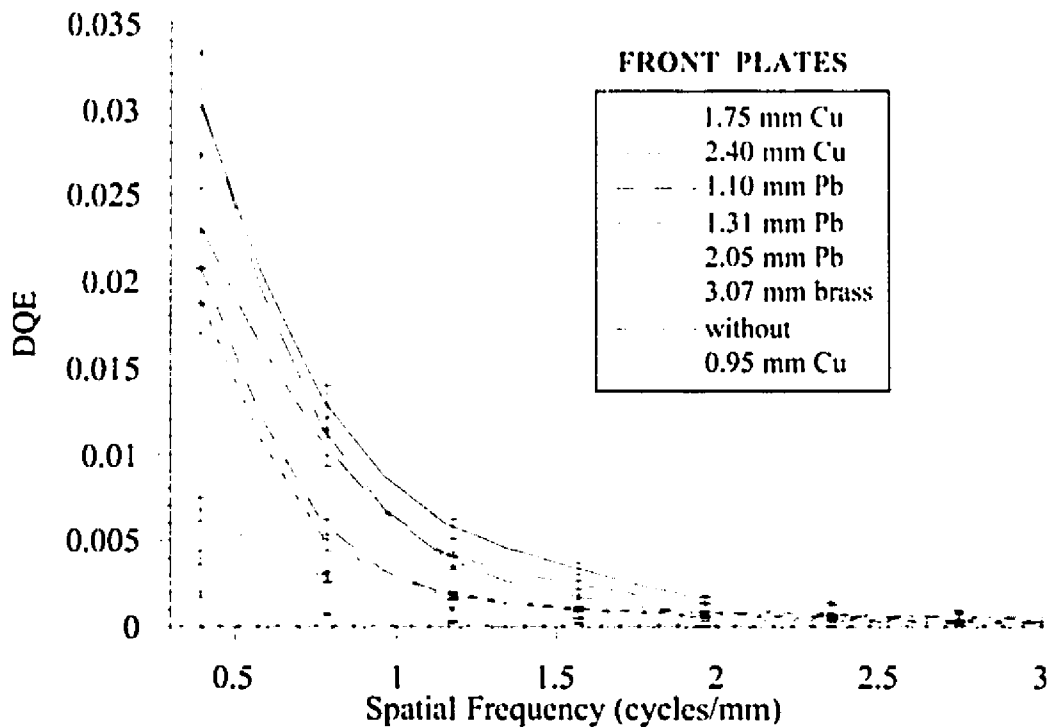


**Figure 4.33** DQE for detectors with Al(1.62 mm) back plates and varying thicknesses of Cu, Pb, or brass front plates or without a front plate.

In Fig. 4.34, we show the DQE curves for detectors with Cu(1.75 mm) front plates and varying back plates: Al(1.62, and 3.22 mm), Cu(0.80 mm), Pb(1.10 mm), and without back plate. The best detectors are the ones with Cu(1.75 mm) front plates and with Al(1.62 mm) or Al(3.22 mm) back plates. The detector without back plate gives the next best DQE followed by the use of Cu and then Pb back plates, which suggests that the diminishment of backscatter from these high physical density back plates is more crucial than shielding the film from room scatter. The Pb back plate detector is by far the worst due to its large backscatter component.

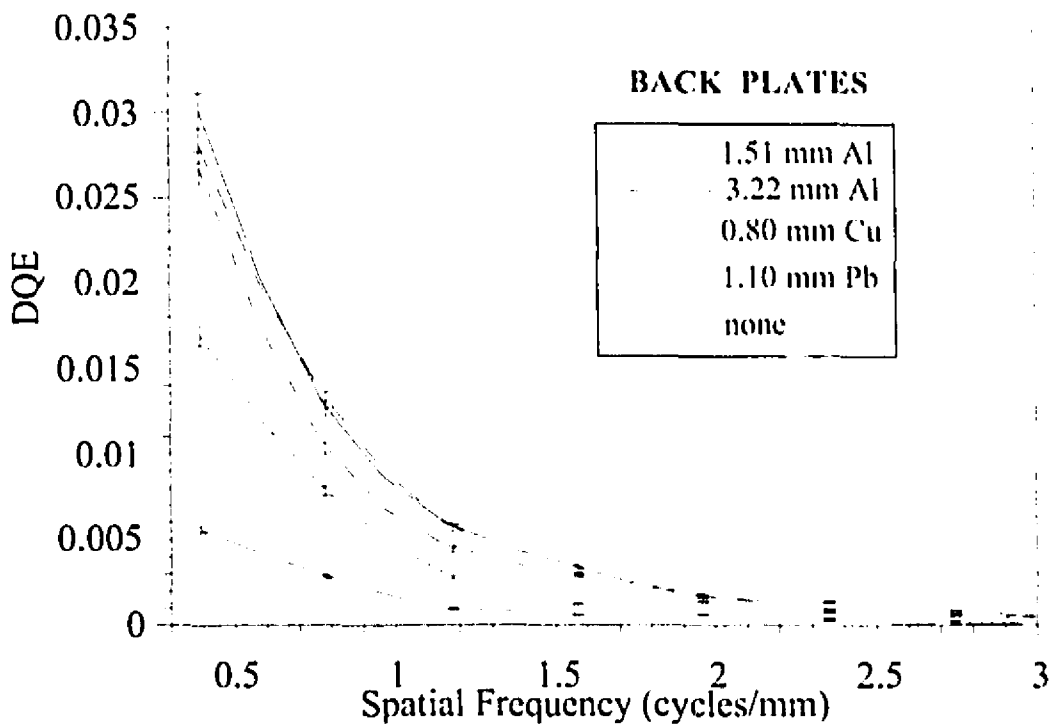


Figure 4.34 DQE for detectors with Cu(1.75 mm) front plates and varying thicknesses of Al, Cu, or Pb back plates or without a back plate.

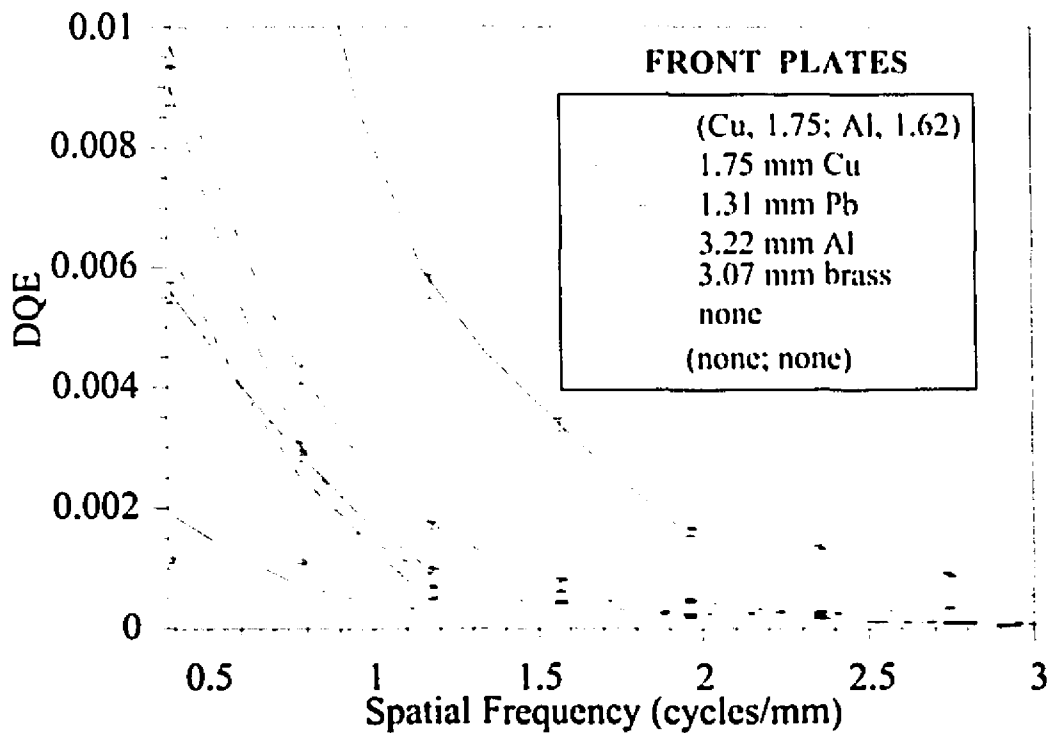


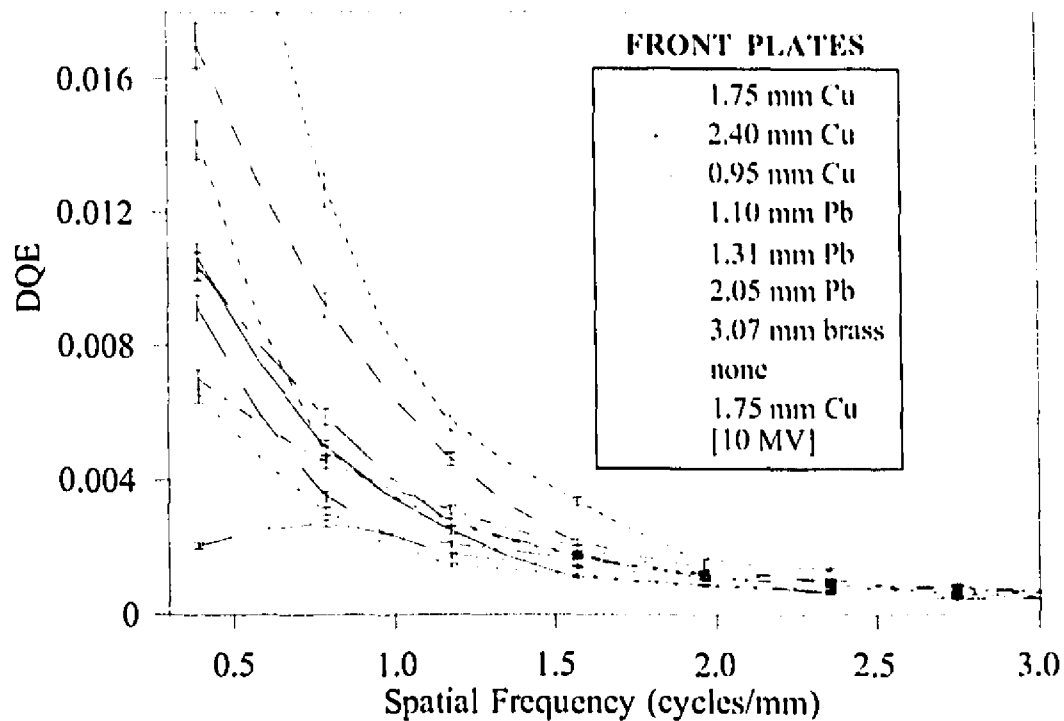
Figure 4.35 DQE for detectors with Pb(1.10 mm) back plates and varying thicknesses of Al, Cu, Pb, or brass front plates or without a front plate. Also shown is the film without metal-plates.

Figure 4.35 shows the DQEs for detectors with Pb(1.10 mm) back plates and varying front plates: Al(3.22 mm), Cu(1.75 mm), Pb(1.31 mm) and brass(3.07 mm) and one without front plate. Also plotted are the curves for the detector without front and back plates, and the best detector from the last two figures (i.e., (Cu, 1.75; Al, 1.62)). Using this latter detector as a point of reference, we can note that a thick Pb back plate will degrade the image quality consistently, independent of the front plate due to its large backscatter component. Detectors without front and/or back plates give, once again, the worst results since their intensification factor is the poorest and the film is not shielded from scatter.

#### 4.3.2 Cobalt-60: Detective Quantum Efficiency

In the next three figures, curves for the DQE of detectors irradiated with Cobalt-60 are shown. In each of the figures, the best DQEs from each of Figs. 4.33 to 4.35 (i.e., for the Clinac-18) are also plotted as a means of comparing the Cobalt-60 and the Clinac-18 beam qualities.

In Fig. 4.36, the detectors consist of Al(0.62 mm) back plates and the following front plates: Cu(0.95, 1.75, and 2.40 mm), Pb(1.10, 1.31, and 2.05 mm), brass(3.07 mm), and without front plate along with the DQE curve for the (Cu, 1.75; Al, 1.62) detector that was irradiated with the Clinac-18 machine. The DQE for the Clinac-18 is better than that of the Cobalt-60 because the thickness of all of the front plates are greater than the maximum range of the electrons from the Cobalt-60 source. Thus, there is substantial total absorption within the plates which implies that a significant number of quanta from the information source do not reach the film, thus reducing the signal-to-noise ratio or NEQ. The best detector for Cobalt-60 is the one with the 0.95 mm thick Cu front plate. The fact that the thickness of Cu that gives the best DQE for the Cobalt-60 beam is thinner than the one that is best for the Clinac-18, implies that the average maximum range of electrons  $R_{\max}$  within a given type of metal does have a significant role in the image quality. For the remaining plates the DQE curves for spatial frequencies greater than 0.7 cycles/mm are more or less grouped together. The worst DQEs correspond to the Pb(1.31 mm) front plate and the detector without a front plate.



**Figure 4.36** *DQE for detectors with Al(1.62 mm) back plates and varying thicknesses of Cu, Pb, or brass front plates or without a front plate.*

In Fig. 4.37, the DQE curves for detectors with Cu(1.75 mm) front plates and varying back plates: Al(1.62, and 3.22 mm), Cu(0.80 mm), Pb(1.10 mm), and without a back plate, are shown. We also show the DQE for the best detector from Fig. 4.34 (i.e., (Cu, 1.75; Al, 1.62)). The DQE is once again best for the Clinac-18 as opposed to the Cobalt-60 unit. The best detector when comparing only the Cobalt-60 results is (Cu, 1.75; Cu, 0.80). The next best detector has a Pb(1.10 mm) back plate, followed by the Al back plates and finally the worst detector is the one without a back plate. This suggests that room scatter is not a negligible parameter. For these same detectors but with the Clinac-18 (Fig. 4.34), the worse DQEs are obtained for the Cu(0.80 mm) and Pb(1.10 mm) back plates, which suggests that room scatter is more pronounced in the Cobalt-60 than the Clinac-18 room (perhaps because the Cobalt-60 room is smaller).

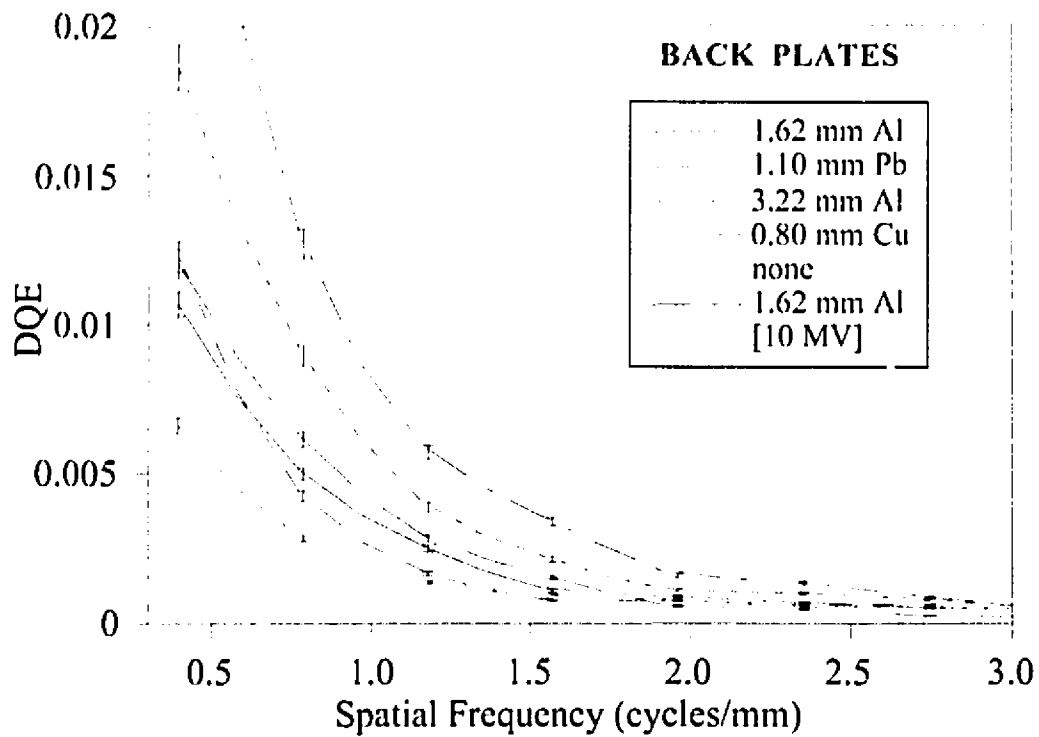


Figure 4.37 DQE for detectors with Cu(1.75 mm) front plates and varying thicknesses of Al, Cu, or Pb back plates or without back plates.

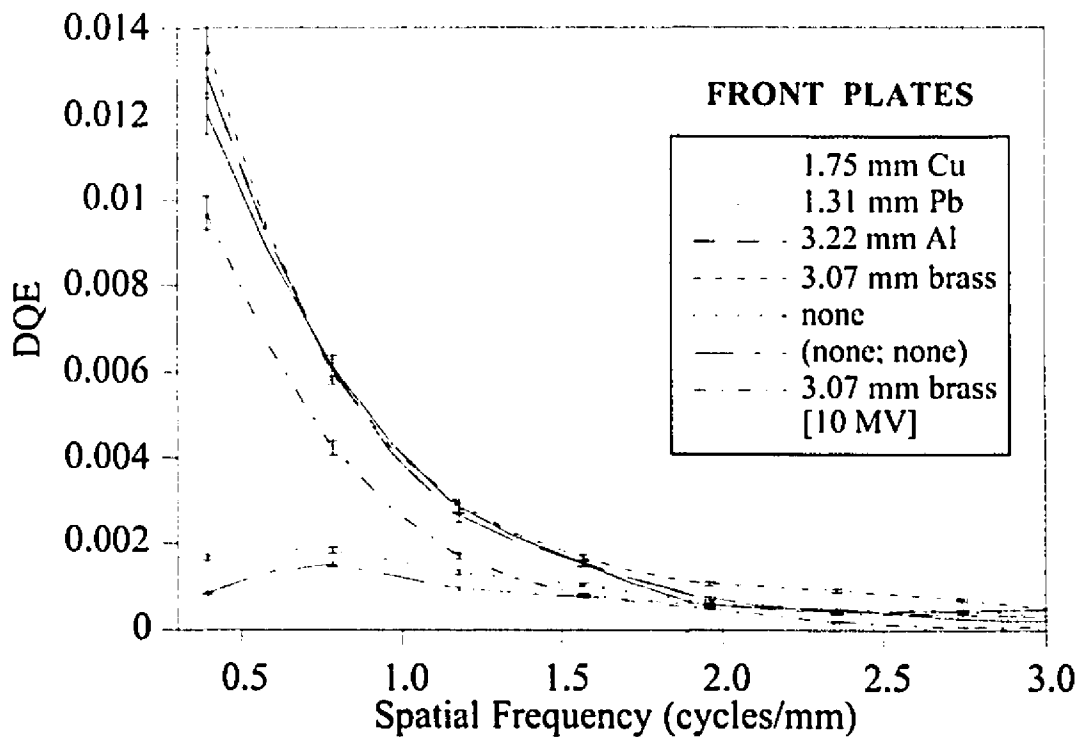


Figure 4.38 DQE for detectors with Pb(1.10 mm) back plates and varying thicknesses of Al, Cu, Pb, or brass front plates or without a front plate. Also shown is the DQE for film alone.

In Fig. 4.38, we show the DQEs for detectors with Pb(1.10 mm) back plates and varying front plates: Al(3.22 mm), Cu(1.75 mm), Pb(1.31 mm) and brass(3.07 mm) and one without front plate. Also plotted is the data for the detector without metal-plates, along with the best detector from Fig. 4.35 (brass, 3.07; Pb, 1.10). In this case, for thick Pb back plates, the DQE from Clinac-18 and from Cobalt-60 do not differ significantly. The use of Pb back plates deteriorates the image to such a degree that the difference in DQE between the two energies is not significant. The DQE for the (brass, 3.07; Pb, 1.10) detector for the Cobalt-60 beam is slightly better than that of the same detector on the Clinac-18. In this figure we also see a sharp difference between the detectors which have front and back plates as compared to those that do not have either one or both. The DQEs of detectors without front and/or back plates are worse than those with front and back plates.

## References

- <sup>1</sup> Droege, R.T., "A megavoltage MTF measurement technique for metal screen-film detectors," *Medical Physics*, 6(4), 272-279, (1979).
- <sup>2</sup> Munro, P., Rawlinson, J. A., and Fenster, A., "A signal-to-noise analysis of metal/plate film detectors," *Medical Physics*, 14(6), 975-984, (1987).
- <sup>3</sup> Das, I.J., Bushe, H.S., "Backscatter and transmission through a high Z interface as a measure of electron beam energy," *Medical Physics*, 21(2), 315-319, (1994).
- <sup>4</sup> Klevenhagen, S.C., Lambert, G.D., and Arbabi, A., "Backscatter in electron beam therapy for energies between 3 and 35 MeV," *Phys. Med. Biol.*, 27, 363-373, (1982).
- <sup>5</sup> Klevenhagen, S.C., *Medical Physics Handbooks 13, Physics of Electron Beam Therapy*, Adam Hilger Ltd. Bristol and Boston (publisher), London, England, 59-61, (1985).
- <sup>6</sup> Webb, S., *The Physics of Three-Dimensional Radiation Therapy: Conformal Radiotherapy, Radiosurgery, and Treatment Planning*, Medical Science Series, IOP Publishing, London, 265, (1993).
- <sup>7</sup> Droege, R. T., and Bjärngard, B. E., "Metal screen-film detector MTF at megavoltage energies," *Medical Physics*, 6(6), (1979).
- <sup>8</sup> Munro, P., Rawlinson, J. A., "Therapy imaging: A signal-to-noise analysis of a fluoroscopy imaging system for radiotherapy localization," *Medical Physics*, 17(5), (1990).
- <sup>9</sup> Barnea, G., Navon, E., Ginzburg, A., Politch, J., Roehrig, H., Dick, C.E., Placious, R.C., "Use of storage phosphor imaging plates in portal imaging and high energy radiography: The intensification effect of metallic screens on the sensitivity," *Med. Phys.*, 18(3), 432-438, (1991).
- <sup>10</sup> Wowk, B., Radcliffe, T., Leszczynski, K.W., Shalev, S., and Rajapakshe, R., "Optimization of metal/phosphor screens for on-line portal imaging," *Medical Physics*, 21(2), 227-235, (1994).
- <sup>11</sup> Hammoudah, M.M., Henschke, U.K., "Supervoltage beam films," *Int. J. Radiation Oncology Biol. Phys.*, 2(5 and 6), 571-577, (1977).
- <sup>12</sup> Johns, H.E., and Cunningham, J.R., *The Physics of Radiology: fourth edition*, Charles C. Thomas (publisher), Illinois, USA, 197-200, (1983).
- <sup>13</sup> I bid reference 5, pp. 53-59.
- <sup>14</sup> Nishikawa, R.M., and Yaffe, M.J., "Signal-to-noise properties of mammographic film-screen systems," *Medical Physics*, 12(1), 32-39, (1985).

- 15 Webb, S. (editor), *The Physics of Medical Imaging: Medical Science Series*, IOP Publishing Ltd., PA, USA, 51-54, (1988).
- 16 Dainty, J. C., and Shaw, R., *Image Science*, Academic Press, London, New York, 298-302, (1974).
- 17 Frieser, H., "Noise Spectrum of developed photographic layers exposed to light, X-rays, and electrons," *Photographic Science and Engineering*, 3(4), 164-169, (1959).
- 18 Wagner, R. F., and Weaver, K. E., "Noise measurement on rare-earth intensifying screen systems," *SPIE : Medical X-Ray Photo-Optical Systems Evaluation*, 56, 198-207, (1975).
- 19 Wagner, R.F. and Sandrik, J.M., "An introduction to digital noise analysis," in: *The physics of medical imaging: Recording System Measurements and Techniques*, A.G., Haus, Ed., American Institute of Physics, New York, New York, 524-545, (1979).
- 20 I bid reference 16, chapter 8.
- 21 Siedentopf, H., "Concerning granularity, density fluctuations and the enlargement of photographic negatives," *Physik Zeit.*, 38, 454, (1937).
- 22 Klein, E., "Theoretical considerations concerning the relationship between characteristic curves of elementary and thick layers," *Photogr. Sci. Eng.*, 4, 341, (1960).
- 23 Wall, F. J. B., and Steel, B. G., "Implications of the method chosen for the measurement of the statistical properties of photographic images," *J. Photogr. Sci.*, 12, 34, (1964).
- 24 Selwyn, E.W.H., "A theory of graininess," *Photogr. J.*, 75, 571, (1935).

## Conclusion

There are several trends in MTF measurements reported in the literature: (1) The MTF decreases with increased energy of the photon beam because the electron range and hence lateral spread increases with beam energy, (2) a high density back plate (i.e., Cu or Pb) degrades the resolution of the system caused by backscatter, and consequently it is suggested that a back plate should never be used, (3) electron scatter dominates the MTF but scattered photons also influence the magnitude of the MTF, (4) a crossover effect is evident when comparing detectors with front plate thicknesses that are ( $< R_{\max}$ ) and ( $> R_{\max}$ ), and (5) the use of the highest density front plate increases the resolution of the system, implying that the density of the plate is more important than atomic number Z considerations.

Our broader analysis of metal-plate/film detectors has allowed us to expand upon the above statements:

- (1) We also find that the MTF increases with a decrease in the photon energy of the beam;
- (2) We also show that high density back plates (i.e., Cu and Pb) degrade the system resolution substantially, but, we further show that the system resolution increases when

low density, low atomic number back plates (i.e. Al) are used. This is because although some minimal backscatter is generated by the Al back plates the reduction of room scatter contamination is significant;

(3) We also found that not only electron but also photon scatter from the front plate affects the resolution of the system. But, we also show through quantitative results that the MTF decreases substantially as the front plate thickness increases beyond  $R_{\max}$ , which can only be attributed to photon scatter and Bremsstrahlung production in the front plate. Seeing that the MTF results can only degrade if we use front plate thicknesses greater than  $R_{\max}$ , the MTF can be used to give us an estimate of  $R_{\max}$  for Cu and Pb. We found that  $R_{\max}$  is less than  $\sim 1.75$  mm in Cu and less than  $\sim 0.39$  mm in Pb for the Clinac-18 and, less than  $\sim 0.95$  mm in Cu and less than  $\sim 0.39$  mm in Pb for the Cobalt-60 unit. The range in Pb for the Cobalt-60 unit is probably much less than 0.39 mm but this is the thinnest Pb plate that we had available;

(4) We have also seen the crossover effect in our results;

(5) Our results suggest that the resolution is not only dependent on the density of the front plate but also on the atomic number  $Z$ , which affects the electron scatter angle. We found that the Cu front plates give a good balance between high density and low atomic number; and

(6) We have also shown that there is a definite dependence of the detector resolution on the combination of the front and back plates used. We have shown that as the front plate (Cu or Pb, say) increases in thickness then the best resolution is obtained with a decrease in the (Al) back plate thickness. A limit in the thickness of the front plate is reached where the best resolution is obtained without using a back plate. This limit is reached when the front plate thickness is approximately 2.5 to 3.5 times  $R_{\max}$ . This last statement comes from the fact that the limiting situation is almost reached for the Cu front plate of thickness 2.40 mm for the Clinac -18, and that the electronic equilibrium in Cu (Table 3.2), using the 10 MV spectrum, occurs at a depth of approximately 1 mm. From the MTF results we obtained, the limiting situation occurs for the Pb front plates of thicknesses 0.39 mm and 1.10 mm, on the Cobalt-60 and Clinac-18, respectively. Thus, a good estimate of  $R_{\max}$  for Pb at Cobalt-60 or Clinac-18 energies would be,  $0.13 \pm 0.03$  mm and  $0.37 \pm 0.06$  mm, respectively.

The detectors that gave the best MTFs are summarized as follows: At Clinac-18 energies, for frequencies less than approximately 0.7 cycle/mm, the best detectors have Cu(0.95 mm) or Pb(0.39 mm) front plates with Al(1.62 mm) or Al(3.22 mm) back plate, respectively. At Cobalt-60 energies, the best detector is (Cu, 0.95; Al, 3.22). For spatial frequencies greater than 0.7 cycles/mm, the crossover effect dominates and detectors without front plates and with Al(1.62 mm) and Cu(0.80 mm) back plates are best for Clinac-18 and Cobalt-60 energies, respectively.

From the NPS measurements two trends are immediately evident:

(1) Film grain noise dominates the total NPS. The NPS are more or less independent of the front and back plate combinations used, the NPS decreases with spatial frequency, and the NPS values do not appear to depend on the photon energy that is used. These trends have been shown by others. The fact that the NPS results change little with the use of different detectors suggests that the film grain noise is the dominant factor in our NPS while the quantum noise power does not play a role. Since for megavoltage photons the NPS decreases with increased spatial frequency, this implies that it is large aggregates of silver grains developed by one quanta, rather than the individual silver grains, that are the basic imaging elements. From the NPS curves the size of these aggregates is  $\sim 140 \mu\text{m}$ . The NPS curves tend towards the same NPS value of  $0.15 \times 10^{-5} \text{ mm}^2$  at high spatial frequencies which implies that this is the base, film grain noise power (i.e., film grain pedestal) stemming from the individual silver grain contributions.

(2) We have the NPS for the same detector (none; Pb, 1.10 mm) but for different film optical densities ranging from 0.52 to 1.81 D. We have shown that generally the NPS increases with optical density, which has been discussed in the literature. Yet, we found that at approximately 1 cycle/mm a crossover occurs for the NPS spectra corresponding to 1.27 and 1.81 D. When the NPS is plotted as a function of optical densities for four spatial frequencies (0.39, 1.57, 3.92, and 8.23 cycle/mm), we see that at the lowest spatial frequency of 0.39 cycle/mm we have a maximum NPS value of  $\sim 3.8 \times 10^{-5} \text{ mm}^2$  occurring at  $\sim 1.3$  D. Thus, an increase in the film exposure beyond  $\sim 1.3$  D will result in a decrease in the NPS which suggests that the variance over large scales decreases with increased exposure, and this implies a formation of a greater number of film grain aggregates covering the image area more uniform (i.e., less fluctuations). This dependence between NPS and optical density, at low spatial frequencies, has not been reported in the literature.

The cause that the DQE for the Clinac-18 can be as much as 1.5 % greater than that of the cobalt-60 machine has to be accounted for. This discrepancy comes mostly from the consideration of the number of input quanta required to irradiate the film to 1.00 D for both machines. The data in Table 3.4 suggests that the intensification factor (sensitivity) of the detectors is lower for the Cobalt-60 beam than for the Clinac-18 10 MV beam. However, there may be a different explanation. The fluence required to obtain an optical density of 1.00 on the film alone (without metal-plates) for Cobalt and Clinac-18 is very similar (i.e., Cobalt-60 : Clinac-18 = 1 : 1.4). Yet, the incident photon fluence required to obtain an optical density of 1.00 from Cobalt is ~ 2.3 times that required for the Clinac-18, when using thick, dense front plates (e.g. (Pb, 2.05; Al, 1.62)) detectors. This means that dense, thick front plates absorb more Cobalt-60 photons than Clinac-18 photons. This suggests that a metal-plate thicker than the range of the electrons should not be used for two reasons: (1) the extra thickness will increase the number of scattered photons while not increasing the number of electrons that exit the plate to the film; and (2) the added thickness, beyond  $R_{max}$ , will attenuate the photon beam, reducing the information gathered from the primary beam. Furthermore, if we compare the fluences from detectors (none; Pb, 1.10) and (Pb, 1.31; Pb, 1.10) for the Clinac-18, we find that the ratio of the incident photon fluence to give 1.00 D on the film, is 4.5 : 1. This suggests that although Pb attenuates the beam, the intensification factor still generates more electrons than the photons that are attenuated. The same situation exists for the Cobalt-60 source but to a lesser extent: The ratio of the fluences of (none; Pb, 1.10) to (Pb, 1.31; Pb, 1.10) is 1.7:1, and in this case, Cobalt is reaching the limit where the front plate removes more photons from the primary beam than the electrons that are generated.

Thick and dense back plates such as Cu or Pb give very poor results due to their large backscatter component and can not be used. Low atomic number and low density back plates such as Al are best. Cu front plates seem to give the overall best results although Pb front plates gave encouraging results. If thinner Pb plates were studied (i.e., 0.1 - 0.3 mm) the results for Pb might have been substantially better. Unfortunately, thicknesses of Pb studied are greater than the range of electrons for the energies used. Detectors without front plates always give the worse DQEs. This is reasonable since a front plate is needed to remove any scattered electrons that are generated from the patient, and for intensification purposes. The best detector for the 10 MV spectrum seems to have a 1.75 mm Cu front plate and a relatively thin Al back plate: 1.62 mm. For the Cobalt-60 source the best detector has a 0.95 mm Cu front plate and a 0.80 mm Cu back plate. This detector gives slightly better results than the (Cu, 0.95; Al, 1.62) detector.

## **Appendix A**

### **A.1 Microdensitometer: Function and operation**

#### **A.1.1 Functionality**

The Micro-10 microdensitometer system used for acquiring the MTF and NPS data can be divided into three subsystems: (1) one measuring the transmission or density information; (2) another for moving the stage in the X and/or Y directions or both; and, (3) another for yielding the precise stage position information.

(1) An area of the film is illuminated with an incandescent light source and optically projected onto a sample-size-defining aperture found on the underside of the film being scanned. Only the light that passes through the aperture is collected; measured with a photomultiplier (PM) tube and digitized by an analog to digital converter (ADC). (2) The scanning is accomplished by the lateral translation of the stage, onto which the film is fixed, relative to the optical axis formed by the source aperture and the scanning aperture. Optical aberrations are reduced by keeping the source and sampling apertures fixed with respect to one another as the stage moves. Low inertia direct current (DC) servo motors control the movement of the stage in the X and Y directions. (3) Digital signals are sent out to the Digital Coordinate Readout System (DCRS) which allow the Micro-10 system to determine the location of the area being measured. Linear Optical directional Encoders (LOEs) are used to determine the precise location of the stage. Perkin-Elmer guarantees that the difference between the measured and known locations will not exceed +/- 5 microns. We calibrated our PDS micro-10 photodigitizer to within less than 1 micron using a calibration test grid.

During scanning in automatic mode, a micro-processor controls all of the functions of the Micro-10 by sending a series of signals to the DCRS, continually monitoring the X and Y stage positions, initiating the ADC conversions, formatting the signals, and storing the data. The operator can define any origin in the plane of the film and the X/Y positions are tallied according to this zero position.

## **A.1.2 Components and operational specifications**

### **A.1.2.1 Optics**

The density measurements are acquired by passing a beam of light from the lower optical system, through the film, and then on to the upper optical system, which is aligned symmetrically by the user to the lower optical system.

Compound type microscopes (160 mm tube lengths) are used for both the influx and efflux optical systems. Each of the microscopes is provided with one objective and four turret-mounted eyepieces, of 5X, 10X, 15X, and 20X (nominal) magnifications. The standard objective used is a 10X 0.30 Numerical Aperture ( $NA$ ) achromate. This set of optics will provide overall nominal magnifications ratios of 50X, 100 X, 150X, and 200X.

The resolution of the compound microscope is diffraction-limited and is related to the  $NA$  by the formula  $2 \cdot NA/\lambda$ . With the wavelength of our source of 555 nm the objectives have a resolution of 1080 lp/mm. The manufacturer recommends that the smallest aperture used should be given by  $3\lambda/2 \cdot NA$  or 2.8  $\mu\text{m}$  (at the film plane).

### **A.1.2.2 Source section**

The source aperture which is imaged onto the underside of the film being digitized, is illuminated by an incandescent lamp. It is a 150 W tungsten-halogen quartz lamp offering incoherent source illumination required for linear photometric performance. The lamp filament is imaged at the entrance pupil of the influx eyepiece, providing uniform Kohler illumination of the film. A stabilized power supply (and the lamp's thermal inertia) insures that measurable fluctuations are not present in the illumination of the film due to the lamp source. The function of the source aperture is to restrict the illuminated area of the film to a size that is only slightly larger than the size of the film that is being sampled. This minimizes the flare in the photodigitizer optical system and allows operation of the instrument over a wider photometric range. Thermal equilibrium of the instrument is reached within one hour of warm-up.

Flare (non-image-forming light), which comes from the region outside of the sampled area but which is nevertheless detected by the photosensor, is the ultimate performance limiting factor for the photometer. Non-linearly biased results are obtained

from the addition of photons to the flux incident onto the photosensor. The flare of the PDS microdensitometer is quoted as being less than one percent of the photometric signal.

### A.1.2.3 Sensor section

A photomultiplier tube (PMT) converts the light intensity, that is modulate by the film, into a voltage signal which is proportional to the intensity of the light. This signal is then amplified by a logarithmic converter and the resulting voltage represents the film density. The transmission value  $T$  is the original linear value, taken directly from the PM tube. The relation between the transmission voltage signal and the film density value  $D$  is shown below

$$D = \text{Log}_{10}(1/T). \quad (\text{A.1})$$

The photosensor used in the PDS microdensitometer is a multi-stage, end-on PMT. Its photocathode is a bialkali photocathode which is sensitive to wavelengths in the range 400 nm - 700 nm. The dark current of the PMT is no more than 0.2 nA at full gain (and with no cooling).

Thirty-two different size sampling apertures are available (Appendix B), along with seven Neutral Density filters, and three color-separating filters. The latter two auxiliary components were not used for our film scanning.

Two eight position handknobs one for each microscope, lettered A through H, are used to select the source apertures desired on each microscope. The settings of the source and sensor (sampling) apertures must coincide. Two four-position eyepiece turrets (one for each microscope), labeled 1 to 4, are used to change the overall magnification ratios. It is recommended that the turrets be rotated for the upper and the lower microscopes so that they have the same magnification ratios. This will ensure that the source aperture will over illuminate the sampling aperture by the proper amount to discourage flaring. Appendix B contains the 32 possible sampling aperture dimensions that are offered by the Micro-10 PDS microdensitometer (i.e. 8 possible aperture handknob positions times 4 possible eyepiece turret positions for magnifications of 50X, 100X, 150X, and 200X).

A Source Aperture/Full Field Control knob is used to toggle between the source and sampling apertures to be able to focus both on the same emulsion. The knob is rotated and

positioned for either viewing of the image of the source aperture (source aperture position) or for viewing the entire screen (full field position). The following procedure must be used when focusing the microscopes: The operator must look at the full field of view and use the focus knob of the upper microscope (located on the head of the machine) to focus the sampling aperture onto the film. The upper microscope is correctly focused when the grains of the emulsion are focused in the full field of view. If there are two emulsions to the film, the task becomes more difficult since both microscopes must be focused on the same emulsion. Next, to ensure that both microscopes are focusing on the same emulsion the full field illuminator handknob is turned so that now the view screen shows the source aperture field of view. In this position, the operator must now focus the image of the source aperture of the lower microscope onto the sampling aperture.

The alignment of the source and the sampling aperture is facilitated with the use of a telescope which is found on the head of the microdensitometer. After the microscopes are focused onto the same point of the film they are aligned with one another. Thumb-screws are found on the base of the sampling microscope to allow manual alignment of the optical axis. The screws are turned to move the cross-hairs, that mark the center of the sampling microscope, into position over the center of the source aperture. After alignment is completed the microscopes are refocused since slight unfocusing occurs during optical axis alignment. It must be noted that both the telescope and the viewing screen must be covered during scanning to avoid incorrect density (transmission) readings due to ambient light contamination.

#### **A.1.2.4 Film stage**

The film is positioned and supported by a glass platen. The light from the source is propagated upwards through the platen, giving an emulsion-up scanning set up of photographic images. The film that we used was of double emulsion type. Since the stage can be programmed to move quite quickly the film has to be fastened down on the platen or between two platens. Usually this can be done adequately with masking tape.

### A.1.2.5 Scanning

An X-Y stage is used to translate the film relative to the instrument optical axis. This action of scanning the film by moving it past the optical axis results in the generation of an analog signal profile for each scan line by the PMT. Digitizing is achieved by sampling the output signal from the PMT at user-defined increments of the stage travel. Each sample is taken on the fly and is triggered by the stage position (due to the LOEs) and not by a clock. This means that variations in stage velocity will not affect the sampling accuracy. Since the PMT is a non-integrating type of photosensor, no pixel smearing is seen, even though the stage is moving while the sample is being taken. A sample-and-hold amplifier samples the photometer output signal and holds it at a level until an ADC has had time to complete its function. The ADC digitizes to 12-bit resolution (i.e. 4096 levels of amplitude). The least significant bit (LSB) of the ADC is 1.25 mV so that all of the bits are set for an input of 5.12 V (i.e.,  $2^{12} \cdot 1.25$  mV). It takes no more than 9 ms for the entire conversion cycle.

There are three types of scanning motions that can be used when scanning with the Perkin-Elmer microdensitometer. The three modes of scanning are depicted below in Fig. A.1.

		<b>Storage Format</b>		
<b>Raster Mode</b>	1 _____ 2 _____ 3	123	654	789
	4 _____ 5 _____ 6			
	7 _____ 8 _____ 9			
<b>Edge Mode</b>	1 _____ 2 _____ 3	123	456	789
	4 - - - - 5 - - - - 6			
	7 - - - - 8 - - - - 9			
<b>Flip Mode</b>	1 _____ 2 _____ 3	123	456	789
	4 _____ 5 _____ 6			
	7 _____ 8 _____ 9			

**Figure A.1** *Microdensitometer scan modes*

First, the raster-type scanning consists of back-and-forth scans in one axis, separated with stepwise motion in the other. It provides the fastest scan time of a given area of film (fastest photodigitizing), since the sampling occurs in both directions (positive and negative). Although, since the data is acquired serially every other line is reversed when stored. The second type of scanning method is edge-mode scanning. In this method, all of the lines are scanning in the same direction so that the stored data is properly ordered, but the scan time is doubled. The third method of scanning combines the fast scanning of the raster-mode and the correct ordering of the data associated with the edge-mode scanning. This mode of scanning is known as flip-mode scanning. Flip-mode scanning can not be used when long scan lines, exceeding the buffer size are involved. With the previous two scan modes, when the number of samples per line exceeds the buffer capacity, a segmented scan automatically occurs. In this case the scan will stop, and the buffer will be dumped onto the storage medium. After which, the stage will back up and recommence scanning along the same scan line. The stage backs up to allow time for the stage to accelerate to the constant scan speed before reading again.

The flip-mode scanning can not be used with segmented scans, unless, the scan area whose length is larger than the buffer is sectioned off in such a manner whereby the length of each area section is shorter than 3200 pixels (buffer size). The scanning of the films used in the thesis was done using the flip-mode scan method and the microdensitometer was programmed to scan the area into sections, since each line would exceeded 3200 points (6000 points). The data from the sections were then concatenated using commercial software.

#### **A.1.2.6 Microprocessor**

The operation of the PDS microdensitometer is controlled by the onboard microprocessor. The external control of the Micro-10 is possible through the optional X-10 interface. The storage buffer that is used during the digitization process is controlled by the microprocessor and can store a maximum of 3200 pixels (6.4 kbytes). The stage velocities are controlled with 8-bit precision. The microprocessor can handle a maximum of 50,000 samples per second.

### **A.1.2.7 Scanning setup procedure**

Scanning parameters such as pixel intervals (pixel size is defined by the optics settings, see Appendix B), scan lengths and scan speeds in each direction, and the scan-mode are defined through the SCANSALOT program supplied with the microdensitometer.

The steps used to prepare the microdensitometer and the film for the scanning are listed below:

1 - The platen is cleaned with a glass cleaner and dried with lens cleaning tissues. The film is firmly fastened to the platen. In our case, the film is placed between two platens, the top platen was held immobile by fastening it to the stage with masking tape. After scanning the film it is removed from between the platens, and the platens are wiped free of dust and smeared finger prints and the next series of films are placed between the platens.

2 - The POWER, LAMP ON, and PMT VOLTAGE control buttons are depressed in that sequence to start the Micro-10.

3 - The desired eyepiece magnification ratios are selected, as well as the sampling and source aperture sizes, using the information in Appendix B.

4 - The upper and lower microscopes are focused on the film. The telescope is used to align the optical axis. The microscopes are re-focused for each new LSF and NPS samples placed between the platens. The 25 cm range of the stage in either direction allows six LSF and four NPS films to be placed between the platens at any one time.

5 - The method used to calibrated the photometer depends on the type of scan that is desired: transmission or density. This calibration must be carried out every time that the next series of films is placed between the platens. The PMT must be calibrated with the following routine if DENSITY readings are used. Note that for this case, the TRANS.-DENS. switch must be switched to the DENS. position.

(a) The Micro-10 must be properly warmed-up, fully operational, and optically aligned (1-4 above). The PMT voltage should be turned down to zero, and the N.D. and color filter should be set on clear.

(b) The stage is now moved so that the optical axis falls onto a film strip that represents the base + fog exposure for the same type of X-ray film (same batch) as that of the film specimens between the platens. Thus, we are scanning net transmittance. When scanning net transmittance care must be taken not to scan off of the films since damage may occur to the PMT since its signal is zeroed to the base + fog exposure value.

(c) The Calib. switch is now set to position 1 and the PMT voltage is increased till the digital panel meter on the control panel reads 1.00. There is a fixed gain of 1.00 in the LOG. mode. The LOG. mode always gives 4096 gray level digitization.

(d) Set the CALIB. switch to position N and adjust the LOG. knob until the meter reads 0.00.

(e) repeat steps c, and d till no further adjustments are needed.

6- Input the desired parameters from the SCANSALOT program after the microdensitometer is put into automatic mode using the manual/automatic button.

7 - Initiate scanning from the SCANSALOT program.

## **Appendix B**

### **B.1 Microdensitometer scanning aperture sizes**

**Table B.1** *Actual scanning aperture sizes for the Micro-10 PDS microdensitometer. 'Dia.' denotes that the column lists the diameters of circular apertures and 'Sq.' denotes that the column lists lengths of square apertures.*

<b>ACTUAL SCANNING APERTURE SIZE (<math>\mu\text{m}</math>)</b>									
<b>Magnification</b>		<b>Apertures</b>							
		<b>A (Dia.)</b>	<b>B (Sq.)</b>	<b>C (Sq.)</b>	<b>D</b>	<b>E</b>	<b>F</b>	<b>G</b>	<b>H</b>
<b>1</b>	50 X	20	20	50	10 x 200	10 x 400	30 x 400	50 x 200	50 x 400
<b>2</b>	100 X	10	10	25	5.0 x 100	5.0 x 200	15 x 200	25 x 100	25 x 200
<b>3</b>	150 X	6.67	6.67	16.7	3.3 x 66.7	3.3 x 133.3	10 x 133.3	16.7 x 66.7	16.7 x 133.3
<b>4</b>	200 X	5.0	5.0	12.5	2.5 x 50	2.5 x 100	7.5 x 100	12.5 x 50	12.5 x 100

## **BIBLIOGRAPHY**

(in parentheses after each entry are the pages on which the reference is referred to)

- American Association of Physicists in Medicine (AAPM), Task Group 28, "Radiotherapy Portal Imaging Quality: AAPM Report #24," *American Institute of Physics*, New York, (1987). (2)
- Andreo, P., "Monte Carlo techniques in medical radiation physics," *Phys. Med. Biol.*, 36(7), 861-920, (1991). (69)
- Antonuk, L.E., Yorkston, J., Boudry, J., Longo, M.L., Jimenez, J., and Street, A., "Development of hydrogenated amorphous silicon sensors for high-energy photon radiotherapy imaging," *IEEE Trans. Nucl. Sci.*, NS-37(2), 165-170, (1990). (4)
- Attix, F.H., *Introduction to Radiological Physics and Radiation Dosimetry*, Appendix E, John Wiley & Sons, Inc., (1986). (60)
- Bailey, N.A., Horn, R.A., and Kamp, T.D., "Fluoroscopic visualization of megavoltage therapeutic x ray beams," *Int. J. Radiat. Oncol. Biol. Phys.*, 6, 935, (1980). (4)
- Barnea, G., Navon, E., Ginzburg, A., Politch, J., Roehrig, H., Dick, C.E., Placious, R.C., "Use of storage phosphor imaging plates in portal imaging and high energy radiography: The intensification effect of metallic screens on the sensitivity," *Med. Phys.*, 18(3), 432-438, (1991). (60, 86)
- Blackman, E.S., *Photo. Sci. Eng.*, 12, 244, (1968). (55)
- Blackman, R. B., and Tukey, J. W., *The measurement of Power Spectra*, Dover, New York, (1958). (26, 55, 59)
- Boyer, A.L., Antonuk, L., Fenster, A., Van Herk, M., Meertens, H., Munro, P., Reinstein, L.E., Wong, J., "A review of electronic portal imaging devices (EPIDs)," *Medical Physics*, 19(1), 1-16, (1992). (3)
- Bracewell, R.N., *The Fourier Transform and Its Applications, second edition*, McGraw-Hill Book Company, chapters 1 to 6, (1978). (11,38,40)
- Brahme, A., "Dosimetric precision requirement in radiation therapy," *Acta. Radiol. Oncol.*, 23, 379-391, (1984). (2,3)
- Brigham, E. O., *The Fast Fourier Transform*, Englewood Cliffs, N.J., Prentice-Hall, Chapter 13, (1974). (26)
- Byhardt, R.W., Cox, J.D., Hornburg, A., and Liermann, G., "Weekly localization films and detection of field placement errors," *Int. J. Radiat. Oncol. Biol. Phys.*, 4, 881-887, (1978). (2)
- Champeney, D.C., *Fourier Transforms and their Physical Applications*, Academic Press, chapters 1-5, (1973). (11)

- Cleare, H. M., Spletstosser, H. R., Seeman, H. F., "An experimental study of the mottle produced by x-ray intensifying screens," *Am. J. Roentgenol.*, 88, 168-174, (1962). (31)
- Cooley, J. W., Lewis, P. A. W., and Welch, P. D., *The Fast Fourier transform algorithm and its applications*, IBM, Yorktown Heights, New York, Res. Paper RC-1743, (1967). (11)
- Cunningham, I. A., and Fenster, A., "A method for the modulation transfer function determination from edge profiles with corrections for finite-element differentiation," *Medical Physics*, 14(4), 533-537, (1987). (47)
- Cunningham, I. A., and Reid, B.K., "Signal and noise in modulation transfer determinations using the slit, wire, and edge techniques," *Medical Physics*, 19(4), 1037-1044, (1992). (46, 47, 48, 58)
- Curry, T.S., Dowdey, J.E., and Murrey, R.C., Jr., *Christensen's Physics of Diagnostic Radiology, forth edition*, Lea & Febiger, 196-218, (1990). (9, 10, 23)
- Dainty, J. C., and Shaw, R., *Image Science*, Academic Press, London, New York, chapters 6 and 7, (1974). (11, 20, 22, 23, 26, 27, 31, 35, 100)
- Das, I.J., Bushe, H.S., "Backscatter and transmission through a high Z interface as a measure of electron beam energy," *Medical Physics*, 21(2), 315-319, (1994). (77)
- De Belder, M., and De Kerf, J., "The determination of the Wiener spectrum of photographic emulsion layers with digital methods," *Photo. Sci. Eng.*, 11(37), 371 - 378, (1967). (29, 61, 65)
- Doi, K., "Wiener spectrum analysis of quantum statistical fluctuations and other noise sources in radiography," In: *Television in Diagnostic Radiology*, Moseley, R. D., and Rust, J. H., Eds., Aesculapius Publishing Co., 313-333, (1969). (27)
- Doi, K., Holje, G., Loo, N., Chan, H., Sandrik, J.M., Jennings, R.J., and Wagner, R.F., "MTF's and Wiener Spectra of radiographic screen-film systems," *HHS Publication*, No. 82-8187 (FDA), (1982). (23, 29, 46, 48, 59, 61, 63)
- Doi, K., Strubler, K., and Rossmann, K., "Truncation errors in calculating the MTF of radiographic screen-film systems from the line spread function," *Phys. Med. Biol.*, 17, 241-250, (1972). (46)
- Droege, R.T., "A megavoltage MTF measurement technique for metal screen-film detectors," *Medical Physics*, 6(4), 272-279, (1979). (4, 46, 48, 49, 55, 56, 58, 59, 60, 77)
- Droege, R. T., Bjärngard, B. E., "Metal screen-film detector MTF at megavoltage X-ray energies," *Medical Physics*, 6(6), 515-518, (1979). (4, 46, 48, 49, 59, 60, 85, 86, 88, 95)
- Duncombe, P.B., and Fox, K., "Precision of determining compliance with prescribed fields from conventional portal films," *British J. Radiol.*, 62, 935-939, (1980). (2)
- Ehrhardt, J.C., "Reduction of aliasing in MTF measurements," *Medical Physics* 13(5), (1986). (46)

- Evans, R.D., *The Atomic Nucleus*, Chapters 21, and 25, Krieger Publishing Company, (1955). (60)
- Fellget, P.B., "Concerning photographic grain, signal-to-noise ratio, and information," *J. Opt. Soc. Amer.*, 43, 271, (1953). (19)
- Ford, R.L., and Nelson, W.R., *The EGS Code System*, Stanford Linear Accelerator Center, Stanford, CA, Report No. 210, (1978). (68)
- Frieser, H., "Noise Spectrum of developed photographic layers exposed to light, X-rays, and electrons," *Photographic Science and Engineering*, 3(4), 164-169, (1959). (100)
- Gelinas, M., and Fletcher, G.H., "Incidence and causes of local failure of irradiation in squamous cell carcinoma of the faucial arch, tonsillar fossa and base of the tongue," *Radiology*, 108(2), 383-7, (1973). (2)
- Gointein, M., and Busse, J., "Immobilization error: some theoretical considerations," *Radiology*, 117, 407-412, (1975). (2, 3)
- Hammoudah, M.M., Henschke, U.K., "Supervoltage beam films," *Int. J. Radiation Oncology Biol. Phys.*, 2(5 and 6), 571-577, (1977). (86)
- Haus, A.G., and Marks, J.E., "Detection and evaluation of localization errors in patient radiation therapy," *Invest. Radiol.*, 8(6), 384-391, (1973). (2, 3)
- Huizenga, H., Levendag, P.C., De Porre, P.M., and Visser, A.G., "Accuracy in radiation field alignment in head and neck cancer: A prospective study," *Radiotherapy and Oncology*, 11, 181-187, (1988). (2)
- ICRU Report 37, Stopping Powers for Electrons and Positrons, Chapter 12, (1984). (60)
- Jenkins, G. M., and Watts, D. G., *Spectral Analysis and its applications*, Holden-Day, San Francisco, (1968). (25, 26)
- Johns, H.E., and Cunningham, J.R., *The Physics of Radiology: fourth edition*, Charles C. Thomas (publisher), Illinois, USA, 197-200, (1983). (88)
- Jones, R.C., "New methods of describing and measuring the granularity of photographic materials," *J. Opt. Soc. Amer.*, 43, 271, (1955). (28, 34, 35)
- Jones, R.C., "New method of describing and measuring the granularity of photographic materials," *J. Opt. Soc. Amer.*, 45, 799, (1955). (19)
- Kinzie, J.J., Hanks, G.E., Maclean, C.J., and Kramer, S., "Patterns of care study: Hodgkin's disease relapse rates and adequacy of portals," *Cancer*, 52, 2223-2226, (1983). (2)
- Klein, E., "Theoretical considerations concerning the relationship between characteristic curves of elementary and thick layers," *Photogr. Sci. Eng.*, 4, 341, (1960). (100)

- Klevenhagen, S.C., Lambert, G.D., and Arbabi, A., "Backscatter in electron beam therapy for energies between 3 and 35 MeV," *Phys. Med. Biol.*, 27, 363-373, (1982). (77)
- Klevenhagen, S.C., Medical Physics Handbooks 13, *Physics of Electron Beam Therapy*, Adam Hilger Ltd. Bristol and Boston (publisher), London, England, 59-61, (1985). (77, 78)
- Leong, J., "Use of digital fluoroscopy as an on-line verification device in radiation therapy," *Phys. Med. Biol.*, 31, 985-992, (1986). (4)
- Marks, J.E., Davis, M.K., and Haus, A.G., "Anatomic and geometric precision in radiotherapy," *Radiologia Clinica et Biologica*, 43(1), 1-20, (1974). (2)
- Marks, J.E., Haus, A.G., Sutton, G.H., and Griem, M.L., "Localization error in the radiotherapy of Hodgkin's disease and malignant lymphoma with extended mantle fields," *Cancer*, 34, 83-90, (1974). (2)
- Marks, J.E., Haus, A.G., Sutton, G.H., and Griem, M.L., "The value of frequent treatment verification films in reducing localization error in the irradiation of complex fields," *Cancer*, 37, 2755-2761, (1976). (2, 3)
- Maruyama, Y., and Khan, F., "Blocking considerations in mantle therapy," *Radiology*, 101, 167-173, (1971). (2)
- Meertens, H., van Herk, M., Bijhold, J., and Bartelink, H., "First clinical experience with a newly developed electronic portal imaging device," *Int. J. Rad. Oncol. Biol. Phys.*, 18, 1173-1181, (1990). (4)
- Morgan, R.H., Bates, L.M., Gopala Rao, U.V., and Marinaro, A., "The frequency response characteristics of X-ray films and screens," *Am. J. Roentgenol.*, 92, 426, (1964). (46)
- Morton, E.J., Swindell, W., Lewis, D.G., and Evans, P.M., "A linear scintillation-crystal photodiode detector for radiotherapy imaging," *Medical Physics*, 18, 681-691, (1991). (4)
- Munro, P., Rawlinson, J. A., and Fenster, A., "Therapy Imaging: A signal-to-noise analysis of metal plate/film detectors," *Medical Physics*, 14(6), 975-984, (1987). (4, 46, 47, 48, 49, 59, 60, 63, 77, 95, 100)
- Munro, P., Rawlinson, J.A., and Fenster, A., "A digital fluoroscopic imaging device for radiotherapy localization," *Proc. SPIE* 1090, 321-329, (1989). (4)
- Munro, P., Rawlinson, J. A., and Fenster, A., "Therapy Imaging: A signal-to-noise analysis of a fluoroscopy imaging system for radiation therapy localization," *Medical Physics*, 17(5), 763-772, (1990). (4, 46, 48, 49, 59, 85, 88, 95)
- Nelson, W.R. (Ed.), *Computer techniques in radiation transport and dosimetry*, New York, New York, Plenum Press, (1980). (68)
- Nelson, W.R., Hirayama, H., and Rogers, D.W.O., *The EGS4 code system*, SLAC report No. 265, Stanford Linear Accelerator center, Stanford, CA, (1985). (69)

- Nishikawa, R.M., and Yaffe, M.J., "Signal-to-noise properties of mammographic film-screen systems," *Medical Physics*, 12(1), 32-39, (1985). (61, 97, 100)
- Nutting, P.G., "On the absorption of light in heterogeneous media," *Phil. Mag.*, 26, 423, (1913). (20, 33)
- O'Neill, E.L., *Introduction to Statistical Optics*, Addison-Wesley, Reading, MA, page 18, (1963). (24)
- Papoulis, A., *Probability, Random Variables and Stochastic Processes*, McGraw-Hill, New York, (1965). (32)
- Papoulis, A., *Systems and Transforms with Applications in Optics*, McGraw-Hill Series in Systems Science, chapters 2 and 3, (1968). (11)
- Perkin Elmer Corporation: Applied Optics Division, The Perkin-Elmer PDS microd reference manual, Gary Rogertson & Assoc. Inc., (1983). (71)
- Perkin Elmer Corporation: Applied Optics Division, Technical manual: Installation, Operation, and Mintenance Instructions for the Micro-10 microdensitometer system, Publication No. TM 169B250, (1983). (71)
- Rabinowitz, I., Broomberg, J., Gointein, M., McCarthy, K., and Leong, J., "Accuracy in radiation field alignment in clinical practice," *Int. J. Radiat. Oncol. Biol. Phys.*, 11, 1957-1967, (1985). (2)
- Roberts R.A., and Mullis, C.T., *Digital Signal Processing*, Addison-Wesley publishing company, Capters 4 and 6, (1975).
- Rogers, D.W.O., "Fluence to Dose Equivalent Conversion Factors aleulated with EGIS3 for electrons from 100 keV to 20 GeV and photons from 11 keV to 20 GeV," *Health Physics*, 46(4), 891-914, (1983).
- Rose, A., "A unified approach to the performance of photographic film, television pick-up tubes, and the human eye," *J. Soc. Motion Picture Engrs.*, 47, 273, (1946). (31, 33)
- Rose, A., *Vision-Human and electronic*, Plenum, New York, (1974). (9)
- Rossmann, K., "Spatial fluctuations of x-ray quanta and the recording of radiographic mottle," *Am. J. Roentgenol*, 90, 863 - 869, (1963). (31)
- Rossmann, K., Lubberts, G., and Cleare, H.M., "Measurement of the line spread function of radiographic systems containing fluorescent screens," *J. Opt. Soc. Am.*, 54, 187-190, (1964). (47)
- Rossmann, K., and Sanderson, G., "Vality of the modulation transfer function of radiographic screen-film systems measured by the slit method," *Phys. Med. Biol.*, 13, 259, (1968). (46)
- Sanderson, G.K., "Erroneous pertubations of the modulation transfer function derived from the line spread function," *Phys. Med. Biol.* 13, 661-663, (1968). (46)

- Sandrik, J. M., and Wagner, R. F., "Radiographic screen-film noise power spectrum: Variation with microdensitometer slit length," *Applied Optics*, 20(16), 2795-2798, (1981). (29, 63)
- Sandrik, J.M., and Wagner, F.R., "Absolute measure of physical image quality: Measurement and application to radiographic magnification," *Med. Phys.*, 9(4), 540-549, (1982). (55, 61)
- Schwarz, R. J., and Friedland, B., *Linear Systems*, McGraw-Hill Book Company, New York, New York, chapter 9, (1965). (21)
- Selwyn, E.W.H., "A theory of graininess," *Photographic J.*, 75, 571, (1935). (20, 34, 100)
- Shalev, S., Lee, T., Leszczynski, K., Cosby, S., and Chu, T., "Video techniques for on-line portal imaging," *Comp. Med. Img. Graph.*, 13, 217-226, (1989). (4)
- Shaw, R., "Image evaluation as an aid to photographic emulsion design," *Photogr. Sci. Eng.*, 16, 395, (1972). (34)
- Shaw, R., "The equivalent quantum efficiency of the photographic process," *The Journal of Photographic Science*, 11, 199-204, (1963). (34, 38)
- Shaw, R., "Evaluating the efficiency of imaging processes," *Report on the Progress of Physics*, 41, 1103-1155, (1978). (35)
- Siedentopf, H., "Concerning granularity, density fluctuations and the enlargement of photographic negatives," *Physik Zeit.*, 38, 454, (1937). (100)
- Suit, H.D., in *Proceedings of the conference on time and dose relationships in radiation biology as applied to radiotherapy*, Brookhaven National Laboratories Publication #50203, (1970). (8)
- Svensson, G.K., "Quality Assurance in radiation therapy: Physics efforts," *Int. J. Radiation Oncol. Biol. Phys. sup. 1*, 10, 23-29, (1984). (2)
- Swindell, W., Morton, E.J., Evans, P.M., and Lewis, D.G., "The design of megavoltage projection imaging systems: Some theoretical aspects," *Medical Physics*, 18(5), 855-866, (1991). (55)
- Taborsky, S.c., Lam, W.C., Sterner, R.E., and Skarda, G.M., "Digital imaging for radiation therapy verification," *Opt. Eng.*, 21, 888-893, (1982). (4)
- Trabka, E. A., "Wiener spectrum scans obtained from an isotropic two - dimensional random field," *J. Opt. Soc. Amer.*, 55, 203, (1965). (29)
- Van Herk, M., and Meertens, H., "A matrix ionization chamber imaging device for on-line patient setup verification during radiotherapy," *Radiother. Oncol.*, 11, 369-378, (1988). (4)
- Van Herk, M., "Physical aspects of a liquid filled ionization chamber with pulsed polarizing voltage," *Medical Physics*, 18, 692-702, (1991). (4)

- Verhey, L.V., Gointein, M., McNulty, P., Munzenrider, J.E., and Suit, H.D., "Precise positioning of patients for radiation therapy," *Int. J. Radiat. Oncol. Biol. Physics*, 8, 289-294, (1982). (2,3)
- Villafana, T., "Modulation transfer function of a finite scanning microdensitometer slit," *Medical Physics*, 2(5), 251-254, (1975). (41, 56)
- Villafana, T., "Effect of microdensitometer scan slit misalignment in MTF determinations," *Medical Physics*, 2(5), 255 - 258, (1975). (56, 60)
- Visser, A.G. , Huizenga, H., Althof, V.G.M., and Swanenburg, B.N., "Performance of a prototype fluoroscopic radiotherapy imaging system," *Int. J. Radiat. Oncol. Biol. Phys.*, 18, 43-50, (1990). (4)
- Wagner, R. F., and Weaver, K. E., " Noise measurement on rare-earth intensifying screen systems," In : *Medical X-ray Photo-Optical Systems Evaluation, Proc. SPIE*, 56, 198-207, Palos Verdes Estates, Ca, (1975), and HEW Publication (FDA) 76-8020, (1975). (29, 61, 66, 100)
- Wagner, R. F., "Fast Fourier Digital Quantum Mottle Analysis with Application to Rare Earth Intensifying Screen Systems," *Med Phys.*, 4(2), 157-162, (1977). (61, 64)
- Wagner, R. F. and Sandrik, J.M., "An introduction to digital noise analysis," in: *The physics of medical imaging: Recording System Measurements and Techniques*, A.G., Haus, Ed., American Institute of Physics, New York, New York, 524-545, (1979). (27, 61, 100)
- Wall, F. J. B., and Steel, B. G., "Implications of the method chosen for the measurement of the statistical properties of photographic images," *J. Photogr. Sci.*, 12, 34, (1964). (100)
- Webb, S. (editor), *The Physics of Medical Imaging: Medical Science Series*, IOP Publishing Ltd., PA, USA, (1988). (10, 23, 100)
- Webb, S., *The Physics of Three-Dimensional Radiation Therapy: Conformal Radiotherapy, Radiosurgery, and Treatment Planning*, Medical Science Series, IOP Publishing, London, 265, (1993). (77)
- Wiener, N., "Generalized harmonic analysis," *Acta Math*, 55, 117, (1930). (19)
- Wong, J.W., Binns, W.R., Cheng, A.Y., Gear, L.Y., Epstein, J.W., Klarmann, J., and Prudy, J.A., "On-line radiotherapy imaging with an array of fiber-optic image reducers," *Int. J. Rad. Oncol. Bio. Phys.*, 18, 1477-1484, (1990). (4)
- Wowk, B., Radcliffe, T., Leszczynski, K.W., Shalev, S., and Rajapakshe, R., "Optimization of metal/phosphor screens for on-line portal imaging," *Medical Physics*, 21(2), 227-235, (1994). (4, 86)
- Zankowski, C.E., *Monte Carlo analysis of the 10 MV x-ray beam from a Clinac-18 linear accelerator*, M.Sc. thesis, 114 pages, (1994). (69)
- Zwieg, H. J., "Autocorrelation and granularity. Part I. Theory," *J. Opt. Soc. Am.*, 46, 805 - 811, (1956). (19)